



**HAL**  
open science

# Oxidation of toluene traces in gas phase in presence of manganese-oxide based catalysts : relationship structure-activity

Zakaria Sihaib

► **To cite this version:**

Zakaria Sihaib. Oxidation of toluene traces in gas phase in presence of manganese-oxide based catalysts : relationship structure-activity. Catalysis. Université de Lyon; Università degli studi (Palerme, Italie), 2018. English. NNT : 2018LYSE1029 . tel-04005669

**HAL Id: tel-04005669**

**<https://theses.hal.science/tel-04005669>**

Submitted on 27 Feb 2023

**HAL** is a multi-disciplinary open access archive for the deposit and dissemination of scientific research documents, whether they are published or not. The documents may come from teaching and research institutions in France or abroad, or from public or private research centers.

L'archive ouverte pluridisciplinaire **HAL**, est destinée au dépôt et à la diffusion de documents scientifiques de niveau recherche, publiés ou non, émanant des établissements d'enseignement et de recherche français ou étrangers, des laboratoires publics ou privés.



N°d'ordre NNT : 2018LYSE1029

## THESE de DOCTORAT DE L'UNIVERSITE DE LYON

opérée au sein de  
l'Université Claude Bernard Lyon 1

**ED 206**  
(Ecole Doctorale de Chimie de l'Université de Lyon)

**Spécialité de doctorat :**  
**Chimie**

Soutenue publiquement le 26/02/2018, par :

**Zakaria SIHAIB**

---

# Oxidation of toluene traces in gas phase in presence of manganese-oxide based catalysts: relationship structure-activity

---

Devant le jury composé de :

**VALVERDE Jose Luis**

Professeur/HDR , Universidad de Castilla-La Mancha (Espagne)

**DUJARDIN Christophe**

Professeur des Universités, HDR, Ecole Supérieure de Chimie de Lille

**GERVASINI Antonella**

Professeure, HDR, Università degli Studi di Milano (Italie)

**GIL Sonia**

Maître de Conférences, Université Lyon 1

**GIROIR-FENDLER Anne**

Professeure des universités, HDR, Université Lyon 1

**GRUTTADAURIA Michelangelo**

Professeur, HDR, Università degli Studi di Palermo (Italie)

**LIOTTA Leonarda Francesca**

Chercheuse , HDR, Università degli Studi di Palermo (Italie)

Président

Rapporteur

Rapporteuse

Co-directrice de thèse

Directrice de thèse

Directeur de thèse

Co-directrice de thèse

**Zakaria Sihaib**

---

**Oxydation de traces de toluène en phase gazeuse en présence de catalyseurs à base de manganèse: relation structure réactivité.**

**Ossidazione di tracce di toluene in fase gassosa in presenza di catalizzatori a base di ossido di manganese: relazione struttura-attività**

---

# UNIVERSITE CLAUDE BERNARD - LYON 1

## **Président de l'Université**

Président du Conseil Académique

Vice-président du Conseil d'Administration

Vice-président du Conseil Formation et Vie Universitaire

Vice-président de la Commission Recherche

Directrice Générale des Services

**M. le Professeur Frédéric FLEURY**

M. le Professeur Hamda BEN HADID

M. le Professeur Didier REVEL

M. le Professeur Philippe CHEVALIER

M. Fabrice VALLÉE

Mme Dominique MARCHAND

## ***COMPOSANTES SANTE***

Faculté de Médecine Lyon Est – Claude Bernard

Faculté de Médecine et de Maïeutique Lyon Sud – Charles  
Mérieux

Faculté d'Odontologie

Institut des Sciences Pharmaceutiques et Biologiques

Institut des Sciences et Techniques de la Réadaptation

Département de formation et Centre de Recherche en Biologie  
Humaine

Directeur : M. le Professeur G.RODE

Directeur : Mme la Professeure C. BURILLON

Directeur : M. le Professeur D. BOURGEOIS

Directeur : Mme la Professeure C. VINCIGUERRA

Directeur : M. X. PERROT

Directeur : Mme la Professeure A-M. SCHOTT

## ***COMPOSANTES ET DEPARTEMENTS DE SCIENCES ET TECHNOLOGIE***

Faculté des Sciences et Technologies

Département Biologie

Département Chimie Biochimie

Département GEP

Département Informatique

Département Mathématiques

Département Mécanique

Département Physique

UFR Sciences et Techniques des Activités Physiques et Sportives

Observatoire des Sciences de l'Univers de Lyon

Polytech Lyon

Ecole Supérieure de Chimie Physique Electronique

Institut Universitaire de Technologie de Lyon 1

Ecole Supérieure du Professorat et de l'Education

Institut de Science Financière et d'Assurances

Directeur : M. F. DE MARCHI

Directeur : M. le Professeur F. THEVENARD

Directeur : Mme C. FELIX

Directeur : M. Hassan HAMMOURI

Directeur : M. le Professeur S. AKKOUCHE

Directeur : M. le Professeur G. TOMANOV

Directeur : M. le Professeur H. BEN HADID

Directeur : M. le Professeur J-C PLENET

Directeur : M. Y.VANPOULLE

Directeur : M. B. GUIDERDONI

Directeur : M. le Professeur E.PERRIN

Directeur : M. G. PIGNAULT

Directeur : M. le Professeur C. VITON

Directeur : M. le Professeur A. MOUGNIOTTE

Directeur : M. N. LEBOISNE

## ACKNOWLEDGEMENTS

*I would like to express my special appreciation and thanks to my supervisors Professor Anne Giroir-Fendler, Professor Leonarda Francesca Liotta and Dr. Sonia Gil, you have been a tremendous mentor for me. I would like to thank you for encouraging my research and for allowing me to grow as a research scientist. Your advice on both research as well as on my career have been priceless. I would also like to thank, Professor Jose Luis Valverde, Professor Claude Descorme. I want to thank you for your brilliant comments and suggestions, thanks to you. All of you have been there to support me when I collected data for my Ph.D. thesis.*

*A special thanks to my family. Words cannot express how grateful I am to my mother, my father, for all of the sacrifices that you've made on my behalf. Your prayer for me was what sustained me thus far. Also my aunt (Mabroka sihaib) and my uncle (Tarek Hadod , God bless his soul), they were of my supporters the length of the study period. I would also like to thank all of my friends who supported me, and incited me to strive towards my goal. At the end I would like express appreciation to my beloved wife Mariam which was always my support in the moments when there was no one to answer my queries.*



## Abstract

In the first part of my work, I have prepared four different catalysts based on manganese oxides: a perovskite ( $\text{LaMnO}_3$ ), via sol-gel method; a simple oxide ( $\text{Mn}_2\text{O}_3$ ), by rapid method and an Octahedral Molecular Sieve (OMS-2) by two different preparation methods, via solid state (OMSs) and hydrothermal method (OMS<sub>h</sub>). The physicochemical properties of these catalysts were characterized by X-ray diffraction (XRD),  $\text{N}_2$  adsorption–desorption, TGA/DTA, ICP-OES and  $\text{H}_2$ -TPR. Their catalytic performances were evaluated in the oxidation of toluene. Three consecutive catalytic cycles were performed for each catalyst in order to reach steady state performances. In order to assess the stability of the catalysts under reaction conditions, the catalytic performances were studied upon long-term experiments running for 24 h at 25% of toluene conversion. Tests of toluene oxidation over a typical industrial catalyst, such as a commercial Pd/ $\text{Al}_2\text{O}_3$  catalyst containing 0.78 wt% Pd, were also performed for comparison purposes. The crystalline features detected in the XRD patterns are well consistent with the formation of the desired structures. Based on their specific surface area and their low-temperature reducibility, the catalysts were ranked as follows: OMSs >  $\text{Mn}_2\text{O}_3$  > OMS<sub>h</sub> >  $\text{LaMnO}_3$ . This trend was in good agreement with the performances observed in the catalytic removal of toluene. A kinetic model was proposed and a good agreement was obtained upon fitting with the experimental data.

In the second part of my work,  $\text{LaMnO}_3$  (LM) catalysts with molar ratio of citric acid (CA) to metal nitrates (Mn and La) ranging from 0.5 to 2 (LM 0.5 to LM 2) were synthesized by citrate sol–gel method, in order to study effect of citric acid ratio on the physico-chemical properties and the catalytic performances. The physicochemical properties of these catalysts were characterized by X-ray diffraction (XRD),  $\text{N}_2$  adsorption–desorption and by inductively coupled plasma atomic emission spectroscopy (ICP-AES). Over selected samples, additional characterizations by

thermogravimetric and differential thermal analysis (TGA/DTA), temperature-programmed reduction by hydrogen ( $H_2$ -TPR) and X-ray photoelectron spectroscopy (XPS) were carried out. The results show that the molar ratio of citric acid to metal nitrates significantly influenced the TGA/DTA profile of gels along with the physico-chemical properties of the catalysts. The crystalline features detected by XRD are well consistent with the formation of  $LaMnO_3$  perovskite phase. Small features of  $Mn_2O_3$  were detected in the diffraction patterns of all LM catalysts except for high CA/Mn+La nitrates molar ratio (1.9 and 2.0). Conversely,  $La_2O_3$  peaks appeared for values ranging from 1.6 to 2, the highest intensity being detected at molar ratio equal to 2. The catalytic performances were evaluated in the oxidation of toluene, performing three consecutive catalytic cycles in order to reach steady-state performances. In order to assess the stability of the catalysts under reaction conditions, long-term experiments running for 24 h at 17 % of toluene conversion were carried out. The catalysts LM1.2, LM1.3 and LM1.5 showed the best catalytic performances in terms of toluene conversion, LM0.8 was poor performing, while LM1 and LM1.7 exhibited an intermediate behaviour.

Keywords: Perovskite, OMS, Manganese Oxide, Oxidation of Toluene, catalytic oxidation, VOC



## Résumé (en français)

Dans la première partie de mon travail, j'ai préparé quatre catalyseurs différents à base d'oxydes de manganèse: une perovskite ( $\text{LaMnO}_3$ ), par voie sol-gel; un oxide simple ( $\text{Mn}_2\text{O}_3$ ), par méthode rapide et un tamis moléculaire octaédrique (OMS-2) par deux méthodes de préparation différentes, via l'état solide (OMS) et la méthode hydrothermale (OMS<sub>h</sub>). Les propriétés physicochimiques de ces catalyseurs ont été caractérisées par diffraction des rayons X (DRX), adsorption-désorption de  $\text{N}_2$ , analyses thermogravimétriques (ATD/ATG), analyses chimiques (ICP-OES) et réduction en température programmée ( $\text{H}_2$ -RTP). Leurs performances catalytiques ont été évaluées dans la réaction d'oxydation du toluène. Trois cycles catalytiques consécutifs ont été réalisés pour chaque catalyseur afin de confirmer les performances. Afin d'évaluer la stabilité des catalyseurs dans des conditions réactionnelles, les performances catalytiques ont été étudiées sur des expériences de longue durée à température constante, pendant 24 h à 25% de conversion du toluène. Des tests d'oxydation du toluène sur un catalyseur de référence, type  $\text{Pd}/\text{Al}_2\text{O}_3$  contenant 0,78% en poids de Pd, ont également été effectués à des fins de comparaison. Les caractéristiques cristallines détectées dans les modèles DRX sont bien compatibles avec la formation des structures désirées. Sur la base de leur surface spécifique et de leur réductibilité à basse température, les catalyseurs ont été classés comme suit : OMSs >  $\text{Mn}_2\text{O}_3$  > OMS >  $\text{LaMnO}_3$ . Cette tendance est en bon accord avec les performances observées dans l'élimination catalytique du toluène. Un modèle cinétique a été proposé et un bon accord a été obtenu lors de l'ajustement avec les données expérimentales. Dans la seconde partie de mon travail, des catalyseurs  $\text{LaMnO}_3$  (LM) avec un rapport molaire acide citrique (CA) sur nitrates métalliques (Mn et La) allant de 0,5 à 2 (LM 0,5 à LM 2) ont été synthétisés par méthode sol-gel citrate, afin d'étudier l'effet du rapport

de l'acide citrique sur les propriétés physico-chimiques et les performances catalytiques. Les propriétés physicochimiques de ces catalyseurs ont été caractérisées par diffraction des rayons X (DRX), adsorption-désorption de N<sub>2</sub> et par spectroscopie d'émission atomique de plasma à couplage inductif (ICP-AES). Sur des échantillons sélectionnés, des caractérisations supplémentaires par analyse thermogravimétrique et thermique différentielle (ATD/ATG), une réduction programmée en température par de l'hydrogène (H<sub>2</sub>-TPR) et une spectroscopie de photoélectrons X (XPS) ont été réalisées. Les résultats montrent que le rapport molaire acide citrique sur nitrates métalliques influence significativement le profil obtenu en ATD/ATG des solides non calcinés ainsi que les propriétés physico-chimiques des catalyseurs. Les caractéristiques cristallines détectées par DRX sont bien compatibles avec la formation de la phase perovskite LaMnO<sub>3</sub>. De petites caractéristiques de Mn<sub>2</sub>O<sub>3</sub> ont été détectées dans les diagrammes de diffraction de tous les catalyseurs LM, à l'exception du rapport molaire élevé des nitrates CA / (Mn + La) (1,9 et 2,0). Inversement, des pics La<sub>2</sub>O<sub>3</sub> sont observés pour des valeurs allant de 1,6 à 2, l'intensité la plus élevée étant détectée au rapport molaire égal à 2. Les performances catalytiques ont été évaluées dans l'oxydation du toluène en réalisant trois cycles catalytiques consécutifs pour atteindre des performances stables. Afin d'évaluer la stabilité des catalyseurs dans des conditions de réaction, des expériences à température constante ont été effectuées pendant 24 h à 17% de conversion du toluène. Les catalyseurs LM1.2, LM1.3 et LM1.5 ont montré les meilleures performances catalytiques en oxydation totale du toluène, tandis que LM1 et LM1.7 présentaient un comportement intermédiaire et LM0.8 était peu actif.

Mots-clés: Pérovskite, OMS, Oxyde de manganèse, Oxydation du toluène, oxydation catalytique, COV

## **Abstract (in italiano)**

Nella prima parte del mio lavoro, ho preparato quattro diversi catalizzatori a base di ossidi di manganese: una perovskite ( $\text{LaMnO}_3$ ), tramite metodo sol-gel;  $\text{Mn}_2\text{O}_3$ , mediante metodo rapido e un setaccio molecolare ottaedrico (OMS-2) mediante due diversi metodi di preparazione, tramite lo stato solido (OMS) e il metodo idrotermale (OMSh). Le proprietà fisico-chimiche di questi catalizzatori sono state caratterizzate tramite diffrazione di raggi X (XRD), adsorbimento-desorbimento di  $\text{N}_2$ , TGA / DTA, ICP-OES e  $\text{H}_2$ -TPR. Le loro proprietà catalitiche sono state valutate nell'ossidazione del toluene. Sono stati eseguiti tre cicli catalitici consecutivi per ciascun catalizzatore al fine di raggiungere conversioni stazionarie. Al fine di valutare la stabilità dei catalizzatori in condizioni di reazione, le prestazioni catalitiche sono state studiate su esperimenti a lungo termine eseguiti per 24 ore al 25% della conversione del toluene. Prove di ossidazione del toluene su un tipico catalizzatore industriale, come un catalizzatore commerciale Pd/ $\text{Al}_2\text{O}_3$  contenente 0,78% in peso di Pd, sono state eseguite per confronto. I picchi cristallini rilevate nei pattern XRD sono ben coerenti con la formazione delle strutture desiderate. Sulla base della loro superficie specifica e della loro riducibilità a bassa temperatura, i catalizzatori sono stati classificati nell'ordine: OMS migliore di  $\text{Mn}_2\text{O}_3$ , migliore di OMSh, migliore di  $\text{LaMnO}_3$ . Questo trend è in buon accordo con le conversioni catalitiche del toluene. È stato proposto un modello cinetico e si è ottenuto un buon accordo con i dati sperimentali.

Nella seconda parte del mio lavoro, catalizzatori di  $\text{LaMnO}_3$  (siglati come LM) sono stati sintetizzati con il metodo sol-gel citrato, con rapporto molare tra acido citrico (CA) e nitrati metallici (Mn e La) compreso tra 0.5 e 2 (serie siglata come LM 0.5 LM 2), al fine di studiare l'effetto del rapporto acido citrico sulle proprietà fisico-chimiche e sulle proprietà catalitiche. Le proprietà fisico-chimiche di questi catalizzatori sono state caratterizzate tramite diffrazione di raggi X (XRD), adsorbimento-desorbimento di  $\text{N}_2$  e spettroscopia di emissione atomica al plasma accoppiata induttivamente (ICP-AES). Su campioni selezionati, sono state effettuate ulteriori

caratterizzazioni, mediante analisi termica termogravimetrica e differenziale (TGA/DTA), riduzione a temperatura programmata in presenza di idrogeno ( $H_2$ -TPR) e spettroscopia fotoelettronica a raggi X (XPS). I risultati mostrano che il rapporto molare tra acido citrico e nitrati metallici ha influenzato in modo significativo il profilo TGA/DTA dei gels assieme alle proprietà fisico-chimiche dei catalizzatori. I picchi cristallini rilevati da XRD sono ben coerenti con la formazione della fase di perovskite  $LaMnO_3$ . Inoltre, ad alta concentrazione di CA, ovvero per il rapporto molare compreso tra 1.6 e 2.0, compare un picco molto poco intenso, attribuito alla fase  $La_2O_3$ . La più alta quantità di  $La_2O_3$  è stata rilevata per un rapporto di acido citrico rispetto agli ioni totali dei metalli uguale a 2.0, sebbene si tratti sempre di quantità trascurabili rispetto alla fase perovskitica. Inoltre impurità attribuite alla fase  $Mn_3O_4$  sono state osservate per i campioni della serie LM1.6-LM2. In conclusione, la migliore purezza di fase in termini di formazione della perovskite  $LaMnO_3$  è stata registrata per i valori del rapporto molare CA/metalli totali nell'intervallo 0.5-1.5.

Le proprietà catalitiche sono state valutate anche per la serie LM a varie concentrazioni di acido citrico nell'ossidazione del toluene, effettuando tre cicli catalitici consecutivi al fine di raggiungere conversioni stazionarie. Per valutare la stabilità dei catalizzatori in condizioni di reazione, sono stati eseguiti esperimenti a lungo termine per 24 ore al 17% della conversione del toluene. I catalizzatori LM1.2, LM1.3 e LM1.5 hanno mostrato le migliori prestazioni catalitiche in termini di conversione del toluene, LM0.8 ha avuto scarso rendimento, mentre LM1 e LM1.7 hanno mostrato un comportamento intermedio.

Parole chiave: Perovskite, OMS, Ossido di Manganese, Ossidazione del Toluene, ossidazione catalitica, VOC

## List of Tables

<b>1</b>	<b>Bibliographic study .....</b>	<b>19</b>
1	Introduction .....	20
1.1	Impact of Volatile Organic Compounds (VOC) .....	21
1.2	Sources and emissions of VOC in Europe, 1990-2014 .....	22
1.3	Toluene.....	25
1.4	VOC control technologies.....	27
1.5	Catalytic Oxidation of VOC .....	29
1.5.1	Noble metal catalysts.....	30
1.5.2	Transition metal oxide .....	32
1.6	Manganese-based catalysts .....	34
1.6.1	Manganese Oxides .....	34
1.6.2	Perovskite-type oxide (LaMnO <sub>3</sub> ).....	35
1.6.3	Octahedral Molecular Sieve (OMS-2).....	36
1.7	Mechanisms and kinetics of catalytic oxidation of VOC .....	39
1.8	Conclusions .....	43
<b>2</b>	<b>Experimental section .....</b>	<b>46</b>
2.1	Catalyst preparation .....	47
2.1.1	Mn <sub>2</sub> O <sub>3</sub> (Rapid preparation method) .....	47
2.1.2	LaMnO <sub>3</sub> (Sol-gel method).....	48

2.1.3 Octahedral Molecular Sieve (OMS-2).....	49
2.1.4 OMS <sub>h</sub> (Hydrothermal method).....	50
2.2 Characterization of Catalysts.....	52
2.2.1 X-ray diffraction (XRD) .....	52
2.2.2 Determination of surface area by physisorption analysis .....	54
2.2.3 Elementary analysis (ICP-OES).....	57
2.2.4 Thermal gravimetric analysis (TGA) and Differential thermal analysis (DTA). 57	
2.2.5 Fourier transform Infrared spectroscopy (FT-IR) .....	58
2.2.6 Temperature programmed reduction (TPR).....	58
2.2.7 X-ray photoelectron spectroscopy (XPS) .....	59
2.3 Toluene catalytic oxidation .....	60
2.3.1 Experimental set-up.....	61
<b>3 Manganese oxide-based catalysts for toluene oxidation.....</b>	<b>64</b>
3.1 Introduction .....	65
3.2 Thermogravimetric and differential thermal analysis.....	65
3.3 XRD characterization.....	69
3.4 N <sub>2</sub> adsorption-desorption at -196 °C.....	71
3.5 H <sub>2</sub> -TPR.....	72
3.6 Catalytic performances in the catalytic oxidation of toluene. ....	73
3.7 Kinetic study.....	79
3.8 Conclusions .....	84

<b>4</b>	<b>The effect of citric acid ratio on LaMnO<sub>3</sub> properties.....</b>	<b>85</b>
4.1	Introduction .....	86
4.2	XRD characterization.....	86
4.3	N <sub>2</sub> adsorption-desorption at -196 °C.....	98
4.4	Thermogravimetric and differential thermal analysis.....	90
4.5	FT-IR .....	92
4.6	H <sub>2</sub> -TPR.....	95
4.7	X-ray photoelectron spectroscopy (XPS) .....	97
4.8	Catalytic performances in the catalytic oxidation of toluene.....	100
4.9	Conclusions .....	104
<b>5</b>	<b>General conclusions.....</b>	<b>105</b>
<b>7</b>	<b>Appendix.....</b>	<b>108</b>
<b>6</b>	<b>References.....</b>	<b>111</b>

## List of Figures

<b>Figure 1.1</b> Schematic picture of photochemical ozone formation in the troposphere.....	22
<b>Figure 1.2</b> Contributions to VOC emissions by sectors in 2016 for EU-28 .....	23
<b>Figure 1.3</b> Changes in the emissions of NMVOC in EU-28 since 1990.....	24
<b>Figure 1.4</b> NMVOC emissions in the EU-28, trend in emissions from the five most important key categories, 1990–2014 .....	25
<b>Figure 1.5</b> Molecular structure of Toluene .....	25
<b>Figure 1.6</b> Classification of VOC control techniques .....	29
<b>Figure 1.7</b> The crystal structure of $Mn_2O_3$ .....	35
<b>Figure 1.8</b> Bulk structure of perovskite ( $LaMnO_3$ ) .....	36
<b>Figure 1.9</b> Structure of cryptomelane .....	38
<b>Figure 1.10</b> Schematic of reaction mechanism for toluene oxidation over OMS-2 catalyst..	41
<b>Figure 2.1</b> Diagram of preparation of $Mn_2O_3$ (Rapid preparation method).....	48
<b>Figure 2.2</b> Diagram of preparation of $LaMnO_3$ (Sol-gel method) .....	49
<b>Figure 2.3</b> Diagram of preparation of OMS (Solid-state method) .....	50
<b>Figure 2.4</b> Diagram of preparation of OMS (Hydrothermal method) .....	51
<b>Figure 2.5</b> Bench of dynamic calcination .....	51
<b>Figure 2.6</b> Electric oven (static calcination) .....	52
<b>Figure 2.7</b> Bragg's diffraction. ....	53
<b>Figure 2.8</b> Six standard types of adsorption isotherm defined by IUPAC .....	55
<b>Figure 2.9</b> Experimental set-up.....	62
<b>Figure 2.10</b> Temperature ramp.....	63
<b>Figure 3.1</b> DTA and TGA profiles received under air for all catalysts (a) $LaMnO_3$ , (b) $Mn_2O_3$ , (c) OMS <sub>h</sub> and (d) OMSs .....	68
<b>Figure 3.2</b> XRD patterns of catalysts $LaMnO_3$ , $Mn_2O_3$ , OMS <sub>h</sub> and OMSs .....	71



<b>Figure 3.3</b> (a), (b) and (c) N <sub>2</sub> adsorption–desorption isotherms and (d), (e) and (f) pore-size distributions of catalysts .....	<b>72</b>
<b>Figure 3.4</b> H <sub>2</sub> -TPR profiles of samples LaMnO <sub>3</sub> , Mn <sub>2</sub> O <sub>3</sub> , OMS <sub>h</sub> , OMS <sub>s</sub> .....	<b>75</b>
<b>Figure 3.5</b> Evolution of the toluene conversion as a function of temperature, while cooling the reactor, upon three consecutive runs (a) LaMnO <sub>3</sub> and Mn <sub>2</sub> O <sub>3</sub> , and (b) OMS <sub>s</sub> and OMS <sub>h</sub> .....	<b>76</b>
<b>Figure 3.6</b> Toluene conversion versus temperature during second consecutive run (cooling ramp).....	<b>78</b>
<b>Figure 3.7</b> Lifetime toluene oxidation test conducted at 25% of toluene conversion during 24h.....	<b>79</b>
<b>Figure 3.8</b> Comparison between experimental and predicted toluene molar flow for catalysts LaMnO <sub>3</sub> , Mn <sub>2</sub> O <sub>3</sub> , OMS <sub>h</sub> and OMS <sub>s</sub> .....	<b>83</b>
<b>Figure 4.1</b> XRD patterns of LaMnO <sub>3</sub> samples, (a) low molar ratio of CA to total metal ions (La <sup>3+</sup> + Mn <sup>2+</sup> ), (b) medium molar ratio and (c) high molar ratio. ....	<b>88</b>
<b>Figure 4.2</b> Relationship between the surface area of the catalysts and the molar ratio of CA to total metal ions (La <sup>3+</sup> + Mn <sup>2+</sup> ). ....	<b>90</b>
<b>Figure 4.3</b> DTA and TGA profiles registered under air for selected non-calcined catalysts and for pure CA, used as reference.....	<b>92</b>
<b>Figure 4.4</b> FTIR spectra of the gels with LM0.5, LM0.8, LM1, LM1.2 and LM2.....	<b>93</b>
<b>Figure 4.5</b> FT-IR spectra of the dried gel and synthesized powder for LM1.3 .....	<b>94</b>
<b>Figure 4.6</b> H <sub>2</sub> -TPR profiles of selected LaMnO <sub>3</sub> catalysts.....	<b>96</b>
<b>Figure 4.7</b> XP survey spectrum recorded for the sample LM1 .....	<b>99</b>
<b>Figure 4.8</b> Experimental Mn2p XP spectra for selected LM samples.....	<b>99</b>
<b>Figure 4.9</b> Relationship between the Mn/La surface atomic ratio and the molar ratio of CA to total metal ions (La <sup>3+</sup> + Mn <sup>2+</sup> ) for selected LM catalysts.. ....	<b>100</b>

**Figure 4.10** Evolution of the toluene conversion as a function of temperature, while cooling the reactor, upon three consecutive runs (a) LM0.8 and LM1, (b) LM1.2 and LM1.3 and (c) LM1.5 and LM1.7. .... **102**

**Figure 4.11** Toluene conversion versus temperature during the second consecutive run (cooling ramp). In the inset, the range of temperature at which conversion values between 40-80% were achieved is displayed. .... **103**

**Figure 4.12** Figure 4.10. Lifetime toluene oxidation test performed at ~17 % of toluene conversion during 24 h. .... **104**

## List of Tables

<b>Table 1.1</b> Physical and chemical properties of toluene .....	<b>26</b>
<b>Table 1.2</b> Summarize of noble metal catalyst systems for the oxidation of toluene .....	<b>32</b>
<b>Table 1.3</b> Catalytic conversion for combustion of toluene reported in the literature .....	<b>38</b>
<b>Table 1.4</b> Summarize of activation energy for oxidation of toluene over different catalysts system and kinetics models used .....	<b>42</b>
<b>Table 3.1</b> Physicochemical properties of the catalysts .....	<b>70</b>
<b>Table 3.2</b> Results of quantitative analysis from H <sub>2</sub> -TPR profiles .....	<b>74</b>
<b>Table 3.3</b> Catalytic performances of the catalysts in the oxidation of toluene. Data were collected upon cooling.....	<b>77</b>
<b>Table 3.4</b> Statistical meaningful of kinetic model parameters .....	<b>82</b>
<b>Table 4.1</b> Physicochemical properties of the catalysts. ....	<b>88</b>
<b>Table 4.2</b> FT-IR spectroscopic results. ....	<b>95</b>
<b>Table 4.3</b> BE of O1s and Mn2p of selected LM oxides and Mn/La atomic ratio. ....	<b>98</b>
<b>Table 4.4</b> Catalytic performances of the catalysts in terms of temperatures for achieving 10, 50 and 90% of toluene conversion. Data were collected upon cooling. ....	<b>103</b>

## Chapter 1

### **Bibliographic study**

## 1 Introduction

Volatile organic compounds (VOCs) are those organic compounds with a saturated vapour pressure of over 10.3 Pa at normal temperature (293.15 K) and pressure (101.325 kPa). The VOCs are a large group of carbon-based chemicals that easily evaporate at room Temperature (de Rivas, López-Fonseca, Jiménez-González, & Gutiérrez-Ortiz, 2011; Li, Wang, & Gong, 2009). VOCs are classified as major contributors to air pollution. They contribute both indirectly as ozone/smog precursors and directly as substances toxic to the environment (Lakshmanan et al., 2010). Rapid urbanization and industrialization contribute to the growing emissions of VOCs into the environment. Emission of VOCs can be from a wide range of outdoor and indoor sources.

The effect of VOCs on the atmosphere depends on the nature of VOCs, and their concentration, and emission sources. However, they has been identified as been responsible for stratospheric ozone depletion, tropospheric ozone formation, ground level smog formation, climate change, sick building syndrome, decay of plants, toxicity of the atmosphere, and carcinogenic effects in humans (Masui, Imadzu, Matsuyama, & Imanaka, 2010). The emission of VOCs can be controlled using methods based on recovery and destruction, in the methods based on destruction; the VOCs are converted into carbon dioxide and water. Catalytic oxidation is one of the most effective and economically feasible techniques for the oxidation of VOCs into CO<sub>2</sub>, water, and other relatively less harmful compounds. The catalytic oxidation targets the complete destruction of VOCs rather than transferring it to another phase as in other techniques (Carabineiro, Chen, Martynyuk, et al., 2015).

The purpose of this work is to synthesis catalytic active metal oxides based on Manganese oxides for volatile organic compounds (VOCs). Background information on VOCs and their impacts are introduced in this Section. The legislation and available control technologies regarding VOCs are also presented here with the emphasis on catalytic oxidation. This section

also includes the theoretical background of the material synthesis and various characterization techniques used in this work.

### **1.1 Impact of Volatile Organic Compounds**

Volatile organic compounds (VOC) are an important class of air pollutants and cover a wide-ranging class of compounds that differ in their properties and chemistry, but display similar behaviour in the atmosphere. Several definitions can be found to describe VOC. For instance, the United States Environmental Protection Agency (US EPA) defines a VOC based on their relative photochemical reactivity in the atmosphere, whilst under European Union (EU) it is defined in terms of volatility and reactivity (Heinsohn & Kabel, 1998). The definition used here (EU) includes any organic compound having a vapour pressure of 0.01 kPa or more at 293.15 K ("European Union emission inventory report 1990–2014 under the UNESCO Convention on Long-range Transponder Air Pollution (LYRA)," 2016). VOC are also sometimes designated as non-methane volatile organic compound (NMVOC), as methane is inert and does not participate in the formation of photochemical smog.

The release of VOC into the atmosphere has widespread environmental implications and has been linked to the stratospheric ozone depletion, the formation of ground level ozone (photochemical smog) and the enhancement of the global greenhouse effect (Barbour et al., 2007; Heinsohn & Kabel, 1998; Monks et al., 2009). Even so, these compounds require special attention due their toxicity (human health effects), high stability and persistence in the environment.

Ground level ozone is the major component of photochemical smog (Heinsohn & Kabel, 1998). High concentrations of ozone can cause impacts ranging from minor effects on the respiratory system to premature mortality. The production of ozone can be illustrated by the following scheme (Figure 1):

This cycle starts with the decomposition of  $\text{NO}_2$  to  $\text{NO}$ , which reacts to  $\text{O}_2$  to form  $\text{O}_3$ . On the other hand,  $\text{O}_3$  is used to oxidize  $\text{NO}$  into  $\text{NO}_2$ . This cycle generates a small contribution to the background ozone concentration. It is important to notice that the concentration of ozone is only a function of the intensity of the light and does not depend strongly on the concentration of  $\text{NO}_x$ .

In the presence of VOC, a new cycle is reestablished and the role of VOC is to convert  $\text{NO}$  to  $\text{NO}_2$  without using up ozone. In this case, ozone will not be consumed by reacting with  $\text{NO}$  and it will accumulate in the atmosphere. In this way, although VOC do not take part in the main reaction of ozone formation, their presence will cause accumulation of ozone at ground level.

## **1.2 Sources and emissions of VOC in Europe, 1990-2014**

The sources of VOC emissions can be divided into biogenic and anthropogenic sources (Heinsohn & Kabel, 1998; Monks et al., 2009). The biogenic sources cannot be easily controlled, and includes the emissions from plants, trees, wild animals, natural forest fires, and anaerobic processes.

The emissions of VOC as result of human activities arise from transport, evaporation, solvent usage, industrial processes (oil refining or chemical manufacture), petrol storage and distribution, landfilled wastes, food manufacture and agriculture. A recent study by the European Union emission inventory report 1990–2014 shows the most significant sources of VOC emissions in the countries of European Union were the industrial processes and product use (49 %), followed by commercial, institutional and households, agriculture and road transport. (see Figure 1.2) ("European Union emission inventory report 1990–2014 under the UNESCO Convention on Long-range Transponder Air Pollution (LYRA)," 2016).

Significant progress already been made in reducing the main air pollutants, and the EU-28 emissions of VOC have dropped 85% since 1990. This reduction has primarily been due to the significant reduction achieved in the road transport (due to the introduction of vehicle catalytic converters and the switching from petrol to diesel cars) and in the use solvents (as a result of the introduction and implementation of the solvent emissions and paints directives (Figure 1.3).



Between 2013 and 2014, Member States reported a decrease of 4.1%, mainly due to decreased emissions in Germany, France and Italy. In 2014, the Member States that contributed most (i.e. more than 10 %) to NMVOC emissions were Germany, Italy and the United Kingdom .

The most important key categories for NMVOC emissions were (2D3d — Coating application)', (1A4bi — Residential: Stationary) and (2D3a — Domestic solvent use including fungicides). Together, they made up 38 % of total emissions (Figure 1.4). Among the top five key categories, the highest relative reductions in emissions between 1990 and 2014 were in the most important key category, (2D3d — Coating applications) (– 52.7 %).

### 1.3 Toluene.

Toluene is a man-made aromatic hydrocarbon produced mostly from petroleum. This chemical intermediate is the predominant feedstock in benzene production and a key octane boosting component for gasoline blending. Toluene is also used as a raw material in the production of other chemicals (*e.g.*, toluene diisocyanate and benzoic acid) and as a solvent in paints and coatings, inks, adhesives, and pharmaceuticals (Scott et al., 1962).

Toluene's molecular formula is  $C_6H_5CH_3$ ; its molecular structure is represent as:

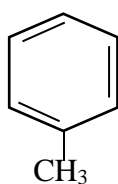


**Figure 1.5:** Molecular structure of Toluene

- Physical and chemical properties

Toluene is a clear, colorless liquid with a sweet, pungent odor. It is produced commercially, primarily through the catalytic conversion of petroleum or recovered as a by-product of the coke oven industry.

**Table 1.1:** Physical and chemical properties of toluene.

<b>Molecular formula</b>	C <sub>6</sub> H <sub>5</sub> CH <sub>3</sub>
<b>Molecular weight</b>	92.13 g/mol
<b>Vapour pressure</b>	28.7 mm Hg at 25°C
<b>Boiling point</b>	110.6°C
<b>Conversion factor</b>	1 ppm = 3.77 mg/m <sup>3</sup>

- **Health Effects**

Exposure to toluene has been shown to cause eye, nose, and throat irritation as well as headaches, dizziness, and feelings of intoxication. It has also been linked to neurological effects including poorer performances in tests of short-term memory, attention and concentration, visual scanning, perceptual motor speeds, and finger dexterity in the completion of physical tasks as well as negative effects on colour vision and auditory capacity. In controlled exposure studies, healthy adults exposed to toluene for 4.5 to 7 hours reported increased eye, nose, and throat irritation as well as headaches, dizziness or feelings of intoxication at concentrations ranging from 189 to 566 mg/m<sup>3</sup> (Andersen et al., 1983; Bælum, Lundqvist, Møhlhave, & Andersen, 1990).

#### **1.4 VOC control technologies.**

There are many different techniques available to control VOCs emissions. These techniques are basically classified into two different groups: (i) process and equipment modification and (ii)

add-on-control techniques. In the first group, control of VOCs emissions are achieved by modifying the process equipment, raw material, and/or change of process, while in the other class an additional control method has to be adopted to regulate emissions. Though the former is the most effective and efficient method, its applicability is limited, as usually it is not possible to modify the process and/or the equipment. The techniques in the second group are further classified into two sub-groups, namely the destruction and the recovery of VOCs. An organisational tree diagram showing various VOC control techniques is presented in Figure. 1.6.

The emission of VOCs can be controlled using methods based on recovery and destruction. The techniques based on recovery include absorption, adsorption, membrane separation, and condensation. High concentrations of VOCs, especially water-soluble compounds can be removed from flue gas streams by absorption using a suitable solvent. The disposal of VOCs and the spent solvent from an absorber are the common problems faced by the absorption processes. Physical and/or chemical adsorption is another technique in which a suitable adsorbent (activated carbon, zeolite, polymeric adsorbents etc.) is employed to selectively adsorb the VOCs. Adsorption approach is economical only in situations where VOCs are highly diluted in a flue gas stream. The high cost of the adsorbents and the necessity of frequent regeneration of the adsorbent are the major limitations of adsorption processes (Kujawa, Cerneaux, & Kujawski, 2015). The VOCs can be removed using condensation induced by increasing the system pressure at a given temperature or lowering the temperature at a given pressure. One of the limitations of the condensation processes is the disposal of the spent coolants. Due to the energy intensive nature of the process, condensation is limited to only evaporative solvents (Shah, Thonon, & Benforado, 2000). Membrane separation is another possible alternative for the removal of VOCs. Silicon rubber membranes are the most commonly used membrane for the separation of VOCs. In the biofiltration process, VOCs in the air is removed biologically in a solid phase reactor (Leson & Winer, 1991). In this approach, the contaminated wet-gas is fed at the bottom of the filter and the

contaminants in air diffuse into a wet, biologically active layer (i.e., biofilm) on the surface of the filter particles. The biofilm with aerobic bacteria degrades the target pollutant(s) and produces CO<sub>2</sub>, water, and microbial biomass. Both the membranes and biofiltration process are costly and their operation/maintenance is expensive.

In the methods based on destruction, the VOCs are converted into carbon dioxide and water. The destruction processes can be thermal, catalytic, or biological oxidation. Thermal oxidation or thermal incineration is suitable for removing VOCs from flue gas streams with a high flow rate and a high concentration of VOCs. More than 99% of the VOCs can be burned by thermal oxidation, typically at high temperatures (>1000 °C), which requires additional fuel and temperature resistant materials. Incomplete thermal combustion produces undesirable by products such as dioxins and carbon monoxide in the incinerator flue gas. Moreover, noxious by products are formed as a result of thermal incineration (Moretti, 2002). The maximum concentration of the VOCs must be less than the lower explosive limit (LEL) of a particular compound in order to avoid any explosions (Khan & Kr. Ghoshal, 2000). In practice, a maximum concentration of 25% of the LEL is used, which can be achieved by diluting with ambient air. Catalytic oxidation systems directly combust VOCs in a manner similar to thermal oxidisers. The main difference is that the catalytic system operates at a lower temperature. This is made possible by the use of catalysts that reduce the combustion energy requirements.

## **1.5 Catalytic Oxidation of VOC**

Catalytic oxidation is one of the most effective and economically feasible techniques for the oxidation of VOCs into CO<sub>2</sub>, water, and other relatively less harmful compounds. The catalytic oxidation targets the complete destruction of VOCs rather than transferring it to another phase as in other techniques, such as in condensation and adsorption. In this approach, the VOCs are oxidized in presence of a suitable catalyst at much lower temperatures (250-500 °C) than thermal oxidation processes (M. Chen, Qi, Fan, Zhou, & Zheng, 2008; X. Chen, Carabineiro, Bastos, et

al., 2014; X. Chen, Carabineiro, Tavares, et al., 2014; Scirè, Minicò, Crisafulli, Satriano, & Pistone, 2003).

Catalytic combustion is a more thermally efficient process than the other non-catalytic thermal oxidation processes and can be used for dilute effluent streams of VOCs (<1% VOCs). Furthermore, it can be more energy efficient if used in the recuperative mode, coupling with a heat exchanger after the catalytic combustion chamber. As catalytic combustion takes place at lower operating temperatures and its start-up fuel requirement is lower. Therefore, moderate volumes of contaminated air can be treated at much lower fuel costs (Musialik-Piotrowska, 2007; Peng & Wang, 2007). Although catalytic oxidation can be applied effectively to treat waste gas streams with varying concentrations of VOCs and flow rates, it is most suitable for moderate flow rates and a low concentration of VOCs (Ojala et al., 2011).

### **1.5.1 Noble metal catalysts**

Supported noble metals (Pt, Pd, Rh etc.) are attractive as catalysts due to their high efficiency for the removal of VOCs at low temperatures (Avgouropoulos, Oikonomopoulos, Kanistras, & Ioannides, 2006; Liotta, 2010; Tidahy, Siffert, Wyrwalski, Lamonier, & Aboukais, 2007). The most common support materials for the noble metal catalysts are ceramics or metallic material in monolithic or honeycomb form. Table 1.2 summarizes some noble metal catalyst systems for the oxidation of toluene reported recently. Noble-metal-based catalysts are expensive and can be deactivated by sintering or poisoning (Liotta, 2010) and alone they are not normally selective enough (Karuppiah et al., 2012). Also they are less stable in the presence of chloride compounds (Everaert & Baeyens, 2004). Several investigations on noble-metal catalysts on different supports have been reported (Cant & Hall, 1970). Performance of these catalysts depends on the method of preparation, precursor type, particle size, metal loading, concentration of the VOCs, reactor type, and the overall gas flow rate (Cant, Angove, & J. Patterson, 1998; Carballo & Wolf, 1978;

Radic, Grbic, & Terlecki-Baricevic, 2004). Larger the heat of formation of an oxide the lesser the activity of the catalyst. Use of noble-metal catalysts in propylene oxidation indicates that the total reaction rate increases with the oxygen pressure and decreases with the olefin pressure. For Rh and Ir the oxidation rate increases with the olefin pressure and decreases with the oxygen concentration. On the contrary, Ru catalysts show higher oxidation rate with increased oxygen pressure while the rate is independent of the olefin pressure (Cant & Hall, 1970; Carballo & Wolf, 1978). Paulis et al. studied the effect of chlorine, which is normally added as a catalyst precursor, on the oxidation of toluene on the Pt/Al<sub>2</sub>O<sub>3</sub> catalyst (Paulis, Peyrard, & Montes, 2001). Chlorinated precursors increase the surface acidity and decrease the adsorption of carbonates and bicarbonates on the surface of the support during CO oxidation. Moreover, using chlorinated precursors will result in platinum oxychloride species, which have a higher reduction temperature. Mixed noble-metal catalysts where Hosseini et al. studied toluene oxidation over a series of bimetallic Pd/Au/TiO<sub>2</sub>-ZrO<sub>2</sub> catalysts (Hosseini et al., 2009). They found that the Au/Pd catalysts showed higher activity than the monometallic Au or Pd catalysts. The highest toluene oxidation performance was found to be at a Pd/Au ratio of 4. The enhanced performance of the bimetallic catalyst is related to the synergistic effects between palladium and gold. Barakat et al. demonstrated the synergistic effects by using the Pd-Nb-V/TiO<sub>2</sub> catalyst for toluene oxidation (Barakat et al., 2012). They showed that doping by a hierarchically structured titania support with Nb and V enhances the catalytic activity of the support in the oxidation of VOCs. Modification with vanadium increases the efficiency of titania supported palladium catalysts for the oxidation of short chain alkenes (Garcia, Solsona, & Taylor, 2004).



**Table 1.2:** Summarize of noble metal catalyst systems for the oxidation of toluene.

<b>Catalyst</b>	<b>Support</b>	<b>Temp (°C)</b>	<b>Conversion %</b>	<b>References</b>
<b>Pt</b>	Activated carbon	109	100	(Joung et al., 2014)
<b>Au</b>	Fe <sub>2</sub> O <sub>3</sub>	260	90	(Han et al., 2014)
<b>Au</b>	Co <sub>3</sub> O <sub>4</sub>	138	90	(Y. Liu et al., 2014)
<b>Pt</b>	Al <sub>2</sub> O <sub>3</sub>	200	95	(Rui, Chen, Lu, & Ji, 2014)
<b>Pd</b>	Nb <sub>2</sub> O <sub>5</sub>	440	90	(Rooke et al., 2015)
<b>Pt</b>	LaMnO <sub>3</sub>	177	90	(Xiangang Wang, Cheung, Di, & Huang, 2012)
<b>Pd</b>	LaMnO <sub>3</sub>	226	90	(Xiangang Wang et al., 2012)
<b>Au</b>	CuO	315	100	(Carabineiro, Chen, Martynyuk, et al., 2015)
<b>Au</b>	MgO	290	100	(Carabineiro, Chen, Martynyuk, et al., 2015)

### 1.5.2 Transition metal oxide.

Non-noble metal-based catalysts can be either supported or unsupported metal oxides (Carabineiro, Chen, Konsolakis, et al., 2015). The supported catalysts show better activity and performance in the oxidation of VOCs due to greater dispersion of the active component. The transition and rare earth metal oxides are used as non-noble-metal catalysts. The most commonly used metal-oxide catalysts include copper oxide, manganese dioxide, iron oxide, nickel oxide, chromium oxide, and cobalt oxide (Galvita, Filez, Poelman, Bliznuk, & Marin, 2014; Garcia et al., 2010; Y.-C. Huang, Luo, Yang, Lin, & Chuang, 2010; Morales, Agüero, & Cadus, 2013;

Solsona et al., 2011; Xia et al., 2009). The non-noble-metal catalysts have several advantages, including being readily available and their low price that make them a good alternative to expensive noble metal catalysts. Although non-noble metal oxides have relatively lower activity than the noble-metal catalysts, they are commonly used for the oxidation of VOCs due to their low cost (Ciuparu, Lyubovsky, Altman, Pfefferle, & Datye, 2002; Delimaris & Ioannides, 2008; G3lin & Primet, 2002; Kim, 2002; Rotter, Landau, Carrera, Goldfarb, & Herskowitz, 2004). Other advantages include the following: long lifetime, masking tolerance, capability of regeneration, and the availability of a range of metal oxides in different sizes and shapes (Zimowska et al., 2007). Support materials and the preparation methods are crucial in determining the performance of metal-oxide catalysts. Support plays an important role in determining the physicochemical properties of the active phase (Satterfield, 1991). Porous materials with a high surface area and large pores favor high dispersion and good catalytic activity in the oxidation of VOCs.

During the oxidation reactions over metal oxides, oxygen can be activated by interacting with oxide surfaces. Coordination, electron transfer, dissociation, and incorporation into the oxide lattice may be steps in the activation process. Two possible states of activated oxygen can be recognized (Satterfield, 1991):

1. Adsorbed oxygen ( $O^-$ ).
2. Lattice-incorporated oxygen species ( $O^{2-}$ ).

The participation of these species is a function of the type of catalyst used (p-oxide or n-oxide) and the oxidation temperature. For instance, p-type semiconductors easily adsorb oxygen as  $O^-$ , which are the active species in oxidation, while in n-type semiconductors lattice oxygen is usually involved (Mars Van Krevelen mechanism) (Satterfield, 1991). Arai and co-workers (Arai, Yamada, Eguchi, & Seiyama, 1986) confirmed the participation of both types of oxygen species in the complete oxidation of methane. At low temperatures the oxidation reaction proceeds with the participation of adsorbed surface oxygen, while at higher temperatures lattice oxygen dominated the oxidation reaction.

## 1.6 Manganese-based catalysts

Manganese oxide is among low cost active catalysts for the oxidation of VOCs (Castaño, Molina, & Moreno, 2015). They have been evaluated for the destruction of many VOCs, including n-hexane (Todorova et al., 2010), acetone (Parida & Samal, 1999), benzene (Genuino, Dharmarathna, Njagi, Mei, & Suib, 2012), ethanol (Aguero, Scian, Barbero, & Cadús, 2008; Bastos et al., 2012), toluene (Aguero et al., 2008; Zhang et al., 2014a), propane (Finocchio & Busca, 2001) and NO<sub>x</sub> (Kang, Park, Kim, & Yie, 2007). The manganese-based catalysts are attractive due to their high efficiency in the oxidation and low toxicity. Performance of manganese oxide depends mainly on the catalyst structure, methods of preparation, surface area, nature of the support material, and the oxidation state (Einaga, Yamamoto, Maeda, & Teraoka, 2015). The catalytic properties of MnO<sub>x</sub> are attributed to the ability of manganese to form oxides with different oxidation states and their high oxygen storage capacity (OSC). Although the nature of the active sites for catalytic oxidation is not well established, several authors attribute their high activity to the mixed valence of framework manganese and to the higher mobility of lattice oxygen. In table 3 catalytic conversion for combustion of toluene reported in the literature.

### 1.6.1 Manganese Oxides.

Manganese oxides ( $\alpha$ -MnO<sub>2</sub>,  $\beta$ -MnO<sub>2</sub>,  $\gamma$ -MnO<sub>2</sub>, Mn<sub>3</sub>O<sub>4</sub>, Mn<sub>2</sub>O<sub>3</sub>) have been extensively studied as catalytic materials in the oxidation of many pollutants as mentioned above.

Literature reports that manganese oxides may offer promising catalytic activity towards the total oxidation of VOCs (Bastos, Órfão, Freitas, Pereira, & Figueiredo, 2009; Brock et al., 1998). Manganese oxide catalysts, such as Mn<sub>3</sub>O<sub>4</sub> (Baldi, Finocchio, Milella, & Busca, 1998), Mn<sub>2</sub>O<sub>3</sub> (Baldi, Escribano, Amores, Milella, & Busca, 1998) and MnO<sub>2</sub> (Lahousse et al., 1998), are

known to exhibit high performances in the catalytic combustion of VOCs (Puértolas et al., 2013). S.H. Kim et al. (Kim & Shim, 2010) have reported that the reactivity of manganese oxides shows an order of  $\text{Mn}_3\text{O}_4 > \text{Mn}_2\text{O}_3 > \text{MnO}_2$  in the total oxidation of benzene and toluene. Similarly, Ramesh et al. (Ramesh et al., 2008) have observed that the reactivity shows an order of  $\text{Mn}_2\text{O}_3 > \text{MnO}_2 > \text{MnO}$  in CO oxidation.

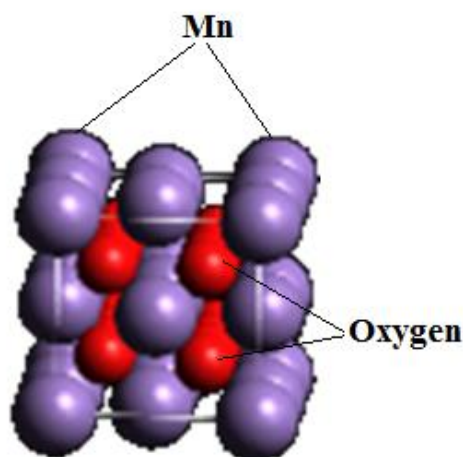


**Figure 1.7:** The crystal structure of  $\text{Mn}_2\text{O}_3$ .

### 1.6.2 Perovskite-type oxide ( $\text{LaMnO}_3$ ).

Perovskite-type oxide is represented by the general formula  $\text{ABO}_3$  as showed in in Figure 1.8. The A cations can be rare earth, alkaline earth, alkali and other large ions such as  $\text{Pb}^{2+}$  and  $\text{Bi}^{3+}$  that occupied into the dodecahedral oxygen coordination. The ideal structure of perovskite is cubic. Deviations from the ideal structure are orthorhombic, rhombohedral, tetragonal, monoclinic and triclinic structures, although the latter three ones are rare and poorly characterized (Peña & Fierro, 2001). The ideal cubic structure becomes unstable because the 12-coordination site is larger than the  $\text{An}^+$  cation and another important structural feature of a perovskite is a distortion in the individual  $\text{MO}_6$  octahedral. Moreover, the possibility to partially substitute either A and/or B position (general formula  $\text{A}_x\text{A}'_{1-x}\text{ByB}'_{1-y}\text{O}_3$ ). Perovskite type oxides containing transition metals are attracting great attention as catalysts for heterogeneous oxidation due to the defect structure and the role of adsorbed oxygen.

The role of perovskite in oxidative catalysis. Adsorbed oxygen ( $\alpha$ -oxygen) or lattice oxygen ( $\beta$ -oxygen) in the perovskite structure Based on the concept, oxygen available for the oxidation reaction is desorbed from perovskite at low temperature. Spinicci et al. (Spinicci, Delmastro, Ronchetti, & Tofanari, 2003) Studied oxygen desorption from perovskite using  $\text{LaMnO}_3$  as a representative material by the temperature programmed desorption technique (TPD).

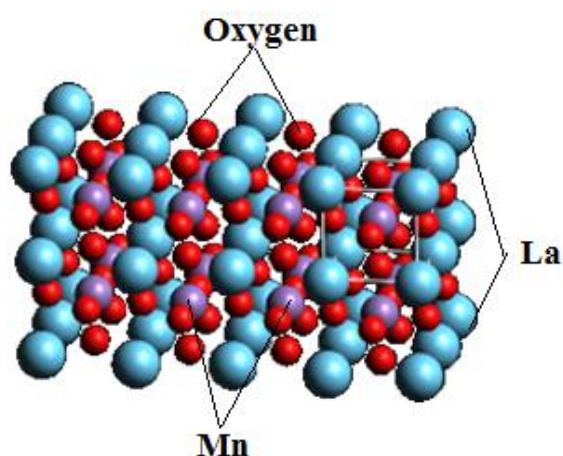


**Figure 1.8:** Bulk structure of perovskite ( $\text{LaMnO}_3$ ).

Perovskite-type metal oxides, more specifically  $\text{LaMnO}_3$ -based perovskites, have attracted much attention due to their adequate catalytic activity and good thermal stability for catalytic oxidation of various hydrocarbons. For example, Spinicci et al. (Spinicci, Faticanti, Marini, De Rossi, & Porta, 2003) investigated the catalytic combustion of acetone, isopropanol and benzene over  $\text{LaMnO}_3$  perovskites, finding that presence of surface oxygen species, easily available and sufficiently mobile, was the fundamental requirement for the high catalytic activity of  $\text{LaMnO}_3$ .

### 1.6.3 Octahedral Molecular Sieve (OMS-2).

Octahedral molecular sieves (OMS) have received considerable attention for over 50 years, due to their exceptional catalytic properties and their shape-selective character (Brock et al., 1998; Feng, Kanoh, & Ooi, 1999). The open frameworks of these materials are composed of edge and corner shared  $\text{MnO}_6$  octahedra, the internal pores being occupied by cations and water molecules.

Cryptomelane-type manganese oxide (K-OMS-2) is one group of the octahedral molecular sieves family (OMS) called hollandite, and has tunnel structures that consist of 2 x 2 arrays of  $\text{MnO}_6$  octahedra (Figure 1.9). Inside the tunnels, potassium cations and small amounts of water stabilize the structure, and can be partially ion-exchanged with other cations with appropriate sizes. The tunnel dimensions are 0.46 nm x 0.46 nm and the average manganese oxidation state is around 3.8, which corresponds to a larger proportion of Mn (IV) with lower amounts of Mn (III) (Feng et al., 1999; Pasero, 2005). The open tunnel structure and mixed valences of OMS-2 make this material very attractive for oxidation catalysis and, therefore, the synthesis of cryptomelane material with high purities, small particle size, high surface areas, and high yield has been a challenge in recent years.

There are some studies concerning the oxidation of several VOC over cryptomelane, namely, benzene (Luo, Zhang, Garcia-Martinez, & Suib, 2008; Luo, Zhang, Huang, & Suib, 2000), toluene (Domínguez et al., 2009), ethanol (Gandhe, Rebello, Figueiredo, & Fernandes, 2007; Peluso, Pronsato, Sambeth, Thomas, & Busca, 2008) and ethyl acetate (Gandhe et al., 2007). The high activity of this catalyst was attributed to the presence of the redox couple Mn(III)/Mn(IV), high mobility of lattice oxygen, open structure and high hydrophobicity (Peluso et al., 2008).

In order to further improve the electronic and catalytic properties, other metal cations have been introduced inside the tunnels or into the framework, by subsequent ion exchange (Cai, Liu, Willis, & Suib, 2001; Shen, Suib, & O'Young, 1994) or by substitution during synthesis (X. Chen, Shen, Suib, & O'Young, 2001; J. Liu et al., 2004). It was observed that the introduction of alkali metal into the tunnel could significantly modify the physical and chemical properties of cryptomelane, specially the surface acid-base properties (J. Liu, Makwana, Cai, Suib, & Aindow, 2003). Liu et al. (J. Liu et al., 2003) synthesized for the first time manganese oxides with  $\text{Li}^+$ ,  $\text{Na}^+$ ,  $\text{Rb}^+$  as tunnel cations and found that the nature of the cation greatly influences the catalytic properties of OMS-2 towards total oxidation of cyclohexane. Moreover, octahedral molecular

sieves with  $\text{Co}^{2+}$ ,  $\text{Ag}^+$  and  $\text{Cu}^{2+}$  as tunnel cations showed high catalytic activities for CO oxidation at low temperatures (R. Hu, Cheng, Xie, & Wang, 2007; Nicolas-Tolentino, Tian, Zhou, Xia, & Suib, 1999).

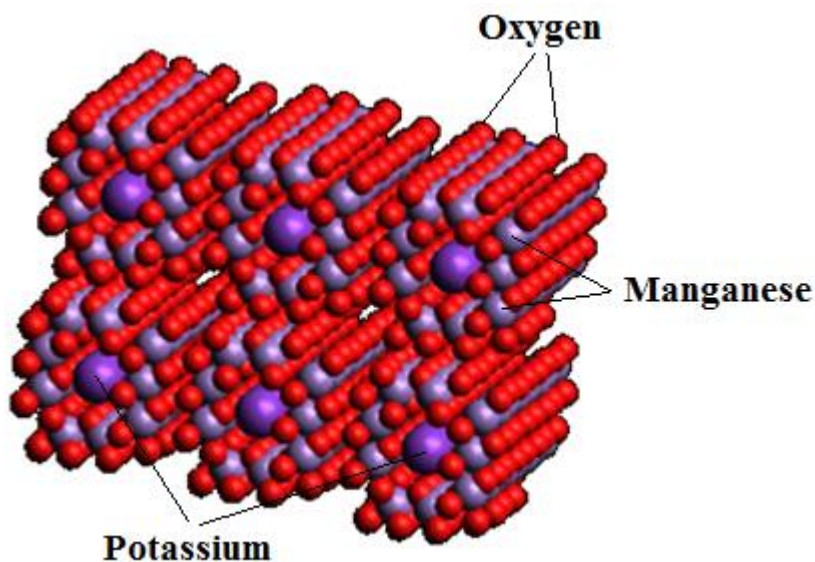


**Figure 1.9:** Structure of cryptomelane.

**Table 1.3:** Catalytic conversion for combustion of toluene reported in the literature.

Catalysts	Preparation Method	Oxidation condition	Toluene conversion	Reference
<b>LaMnO<sub>3</sub></b>	Citrate sol-gel Glycine combustion Co-precipitation	1000 ppm Toluene, 15000 mL g <sup>-1</sup> h <sup>-1</sup>	T <sub>50</sub> = 203 °C T <sub>50</sub> = 239 °C T <sub>50</sub> = 213 °C	(Zhang et al., 2014a)
<b>LaMnO<sub>3</sub></b>	Citrate sol-gel	1000 ppm Toluene, 60000 mL g <sup>-1</sup> h <sup>-1</sup>	T <sub>50</sub> = 358 °C	(Giroir-Fendler et al., 2016)
<b>OMS-2</b>	Refluxing Solid-state reaction	1000 ppm Toluene, 20000 h <sup>-1</sup>	T <sub>50</sub> = 215 °C T <sub>50</sub> = 270 °C	(Sun, Chen, Wang, & Quan, 2011)
<b>M<sub>2</sub>O<sub>3</sub></b>	PMMA-templating strategy	1000 ppm Toluene, 20000 mL g <sup>-1</sup> h <sup>-1</sup>	T <sub>50</sub> = 268 °C	(Y. Liu et al., 2013)

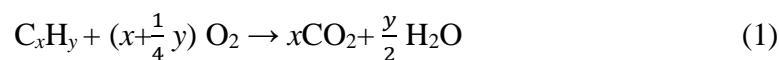
<b>M<sub>2</sub>O<sub>3</sub></b>	Solution combustion synthesis	1000 ppm Toluene, 19100 h <sup>-1</sup>	T <sub>50</sub> = 245 °C	(Piumetti, Fino, & Russo, 2015)
<b>Catalysts</b>	<b>Preparation Method</b>	<b>Oxidation condition</b>	<b>Toluene conversion</b>	<b>Reference</b>
<b>5%Mn<sub>x</sub>O<sub>y</sub>/Al<sub>2</sub>O<sub>3</sub></b>	Incipient wetness impregnation	4000 ppm Toluene, 3600 mL g <sup>-1</sup> h <sup>-1</sup>	T <sub>50</sub> = 335 °C	(C.-H. Wang, 2004)
<b>30%Mn<sub>x</sub>O<sub>y</sub>/Al<sub>2</sub>O<sub>3</sub></b> <b>60%Mn<sub>x</sub>O<sub>y</sub>/Al<sub>2</sub>O<sub>3</sub></b>	Impregnation	1000 ppm Toluene, 200000 mL g <sup>-1</sup> h <sup>-1</sup>	T <sub>50</sub> = 340°C T <sub>50</sub> = 290 °C	(Saqr, Kondarides, & Verykios, 2011)
<b>Mn<sub>x</sub>O<sub>y</sub>/TiO<sub>2</sub></b>	Impregnation	1000 ppm Toluene, 35000 h <sup>-1</sup>	T <sub>50</sub> = 315°C	(Larsson, Andersson, Wallenberg, & Svensson, 1996)
<b>15% Mn<sub>x</sub>O<sub>y</sub>/Al<sub>2</sub>O<sub>3</sub></b>	Incipient wetness impregnation	1000 ppm Toluene, 4800 h <sup>-1</sup>	T <sub>50</sub> = 300 °C	(Kim, 2002)

### 1.7 Mechanisms and kinetics of catalytic oxidation of VOCs.

There are ranges of volatile compounds, which play a direct role in atmospheric chemistry. Although the catalytic oxidation of VOCs has been extensively studied, it is still difficult to provide a generalized correlation and a single reaction mechanism due to the different properties of pollutants and reaction conditions. Hermia and Vigneron have established a correlation between the oxidizability of VOCs and their molecular weight (Hermia & Vigneron, 1993). According to them, the higher the molecular weight, the more difficult it is to oxidize VOCs. This correlation agrees well with the order established by Palazzolo and Tichenor regarding the ease of oxidation: alcohols < aldehydes < aromatics < ketones < acetates < alkanes (Tichenor & Palazzolo, 1987).



At sufficiently high reaction temperatures, the catalytic oxidation mainly gives CO<sub>2</sub> and H<sub>2</sub>O according to the following reaction:



The mechanisms proposed for the complete catalytic oxidation of VOCs generally fall into three main categories: (i) Mars–van Krevelen (MVK) model, (ii) Langmuir- Hinshelwood (L-H) model, and (iii) Eley-Rideal (E-R) model.

Mars-van Krevelen model considers that the reaction occurs between the adsorbed VOCs and the lattice oxygen of the catalyst rather than the oxygen in the gas phase. This model assumes that the oxidation of the VOCs takes place in two steps as shown in Figure 1.10. When the reactants contain no gaseous oxygen, the catalytic oxidation of toluene consists of two irreversible steps, namely toluene oxidation by lattice oxygen and the reduction of manganese cations, and the re-oxidation of the catalyst by lattice oxygen from the bulk OMS-2. The conversion of toluene in the absence of oxygen could be attributed to substrate oxidation with oxygen supplied from the solid OMS-2. In this case, the OMS-2 catalyst seem to be a reservoir of oxygen species to sustain oxidation in the absence of gas-phase oxygen due to the coexistence of the mixed-valent Mn and the facile transform between Mn<sup>4+</sup> and Mn<sup>3+</sup> (DeGuzman et al., 1994). The presence of coupled Mn<sup>4+</sup>/Mn<sup>3+</sup> sites allows electron exchange and, hence, oxygen mobility throughout the bulk and the surface. Moreover, it could be found that the intensity of the CO<sub>2</sub> bands increases with increasing temperature, implying the mobility of lattice oxygen could enhance the production of CO<sub>2</sub>. This clearly notes that the higher the mobility of lattice oxygen from the bulk to the surface, the better the catalytic activity of total oxidation toluene on OMS-2. This model has been widely used for kinetics modeling of oxidation reactions of hydrocarbons over metal oxide catalysts (Ordóñez, Bello, Sastre, Rosal, & Díez, 2002). According to the Mars-van Krevelen mechanism, Equation 2 can express the rate of oxidation of the VOCs.

$$-r_{VOC} = \frac{k_{O_2} k_{voc} P_{voc} P_{O_2}}{\gamma k_{voc} P_{VOC} + k_{O_2} P_{O_2}} \quad (2)$$

Where,  $-r_{VOC}$ : reaction rate (mol/m<sup>3</sup>/s);  $P_{VOC}$ : partial pressure of the VOCs;  $P_{O_2}$ : partial pressure of oxygen;  $k_{voc}$ : rate constant of VOCs oxidation;  $k_{O_2}$ : rate constant of catalyst re-oxidation;  $\gamma$  is the stoichiometry coefficient of O<sub>2</sub> in the oxidation.

The Langmuir-Hinshelwood (L-H) mechanism assumes that the reaction takes place between the adsorbed VOCs and the adsorbed oxygen. Therefore, it is essential for both the VOCs and oxygen molecule (species) to be adsorbed on the surface of the catalyst (Behar et al., 2015). The VOCs and oxygen may adsorb on similar type of active sites (single site L-H model) or two

different types of active sites (dual site L-H model). Accordingly, the rate expressions for the single site L-H model and dual site LH model are different as expressed by Equation 3 and Equation 4, respectively.

$$-r_{VOC} = \frac{kK_{O_2}K_{voc}P_{voc}P_{O_2}}{1 + K_{voc}P_{voc} + K_{O_2}P_{O_2}} \quad (3)$$

$$-r_{VOC} = \frac{kK_{O_2}K_{voc}P_{voc}P_{O_2}}{(1 + K_{voc}P_{voc})(1 + K_{O_2}P_{O_2})} \quad (4)$$

Where,  $K_{O_2}$  is the equilibrium constant for the adsorption of oxygen and  $K_{voc}$  is the equilibrium constant for the adsorption of VOCs. The advantage of this model is that it not only includes the reaction rate but also takes into consideration of the adsorption of VOCs and oxygen.

According to the Eley–Rideal (E–R) mechanism, the reaction occurs between the adsorbed oxygen species and reactant molecules in the gas phase. The controlling step is the reaction between an adsorbed molecule and a molecule in the gas phase (Behar et al., 2015). The following equation represents the kinetic expression based on the E-R mechanism.

$$-r_{VOC} = \frac{kK_{voc}P_{voc}P_{O_2}}{(1 + K_{voc}P_{voc})} \quad (5)$$

The validity of each mechanism strongly depends on the properties of the catalyst (active metal and the support) as well as on the nature of the VOCs. Generally, one of the above models provides a good fit for the experimental data for the oxidation of the VOCs over metal-oxide and noble metal catalysts.

**Table 1.4:** Summarize of activation energy for oxidation of toluene over different catalysts system and kinetics models used.

<b>Catalyst</b>	<b>Model type</b>	<b>Activation energy (kJ/mol)</b>	<b>Reference</b>
<b>Pt/Al<sub>2</sub>O<sub>3</sub></b>	Mars-van Krevelen	71	(Radic et al., 2004)
<b>Pd/activated- C</b>	Langmuir-Hinshelwood	79.5	(Bedia, Rosas, Rodríguez-Mirasol, & Cordero, 2010)
<b>Cu<sub>1.5</sub>Mn<sub>1.5</sub>O<sub>4</sub></b>	Mars-van Krevelen	108.5	(Behar et al., 2015)
<b>Pt/<math>\gamma</math>-Al<sub>2</sub>O<sub>3</sub></b>	Mars-van Krevelen	104.6	(Ordóñez et al., 2002)
<b>LaMnO<sub>3</sub></b>	Power law	97	(Y. Liu et al., 2012)
<b>Cu<sub>0.13</sub>Ce<sub>0.87</sub>O<sub>y</sub></b>	Langmuir-Hinshelwood	106.7	(C. Hu, 2011)
<b>MnNi</b>	Langmuir-Hinshelwood and Eley-Rideal	50	(Duplančić, Tomašić, & Gomzi, 2017)
<b>Al/Al<sub>2</sub>O<sub>3</sub>-MnNi metallic monolith</b>	Langmuir-Hinshelwood and Eley-Rideal	96	(Duplančić et al., 2017)
<b>Mn-Al</b>	Mars-van Krevelen	84	(Chlala et al., 2016)
<b>La<sub>0.75</sub>Ag<sub>0.25</sub>MnO<sub>3</sub></b>	Eley-Rideal	43.3	(Borzęcka ,2012)
<b>La<sub>0.75</sub>Ag<sub>0.25</sub>MnO<sub>3</sub>+0.3%Pt</b>	Eley-Rideal	34	(Borzęcka ,2012)
<b>La<sub>0.75</sub>Ag<sub>0.25</sub>MnO<sub>3</sub>+0.3%Pd</b>	Eley-Rideal	38.6	(Borzęcka ,2012)

Table 1.4 summarizes the kinetics models and the estimated activation energies for the oxidation of toluene reported in the literature. The activation energy varies between 34 and 108 kJ/mol.

## 1.8 Conclusions.

In conclusion, Volatile Organic Compounds (VOCs) emitted from industrial processes and automobile are not only harmful to human health because they are malodorous, mutagenic and/or carcinogenic but also because they can form toxic photochemical oxidants and suspended particulate matters through photochemical reactions. Many countries have already enacted stringent legislations to abate VOC emissions. In order to efficiently remove VOCs, various technologies have been developed, including adsorption, bio-degradation, membrane separation, thermal incineration and photo-catalytic oxidation (Zhang et al., 2014b). Among these technologies, catalytic oxidation is considered as the most promising process for limiting VOCs' emissions. Indeed, catalytic oxidation might be operated at temperatures much lower compared to thermal incineration. Noble metal catalysts demonstrated higher activity compared to base metal catalysts; however, their cost is much higher. Therefore, many efforts are being paid to the development of transition metal oxide-based catalysts with high catalytic activity. Among them, manganese oxide-based catalysts are the most active.

In this thesis, different manganese oxide catalysts have been prepared in order to improve the catalytic performance of these systems for VOC abatement at low temperature.

This PhD thesis is subsequently organized as follows:

Chapter 1 is the background of the research work and literatures survey.

Chapter 2 introduces the materials and experimental methodologies used for catalyst preparation, characterization and activity measurement.

Chapter 3 collects the results on the preparation of manganese oxide catalysts, their catalytic performances for toluene oxidation, stability and durability in the reaction.

Chapter 4 collects the results on the optimization of the perovskite  $\text{LaMnO}_3$  system and more particularly the impact of the ratio between citric acid and manganese precursor. For that different catalysts catalytic performances for toluene oxidation, stability and durability in the reaction are performed and discussed in relation with chemical and physical properties.

Chapter 5 provide the general conclusions, prospects and references, respectively.

## Chapter 2

### Experimental section

## 2.1 Catalyst preparation

Based on the state-of-the-art, different synthesis routes were selected for the preparation of different families of Mn oxide catalysts. The rapid preparation method for  $\text{Mn}_2\text{O}_3$  ( $\text{Mn}_2\text{O}_3\text{R}$ ) (CUI et al., 2014), the sol-gel method was the most appropriate for perovskites ( $\text{LaMnO}_3$ ) (Zhang et al., 2014a), the solid state route for OMSs (Sun et al., 2011), the hydrothermal synthesis for OMSs (Ding et al., 2005).

### 2.1.1 $\text{Mn}_2\text{O}_3$ (Rapid preparation method)

4.9018 g (20 mmol) of  $(\text{Mn}(\text{CH}_3\text{COO})_2 \cdot 4\text{H}_2\text{O})$ , 99%, CAS:6156-78-1, Sigma-Aldrich) was dissolved in 100 mL of ethanol. After addition of 40 mL ( $\text{NH}_3 \cdot \text{H}_2\text{O}$  25%, CAS: 007-001-01-2, Sigma-Aldrich), the solution, which was initially colourless, turned to light red. However, no precipitate was formed. Subsequently,  $1.5 \text{ L min}^{-1}$  air was bubbled into the solution for 5 min at  $50 \text{ }^\circ\text{C}$ . The solution gradually changed to deep black as colloids were formed. These colloids appeared to be evenly dispersed in the bulk of the solution and stable. Finally, the suspension was centrifuged, dried at  $110 \text{ }^\circ\text{C}$  over night showed in Figure 2.1, and calcined at  $500 \text{ }^\circ\text{C}$  (the heating rate of  $5 \text{ }^\circ\text{C min}^{-1}$ ) for 2 h in a quartz tubular reactor under air atmosphere shown in Figure 2.6.



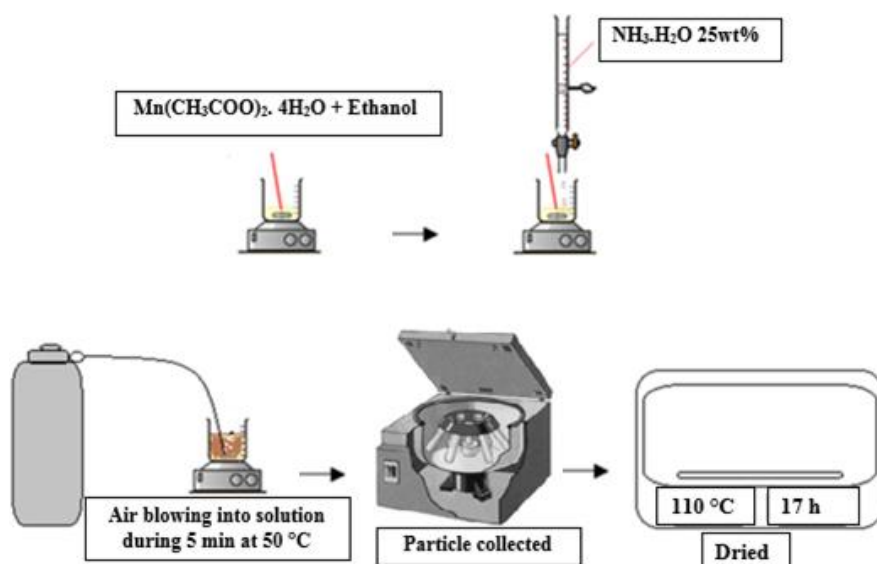


**Figure 2.1:** Diagram of preparation of Mn<sub>2</sub>O<sub>3</sub> (Rapid preparation method).

### 2.1.2 LaMnO<sub>3</sub> (Sol-gel method)

Nitrates (La (NO<sub>3</sub>)<sub>3</sub>·6H<sub>2</sub>O, 99 %, CAS: 10277-43-7, Fluka and Mn (NO<sub>3</sub>)<sub>2</sub>·4H<sub>2</sub>O, 98 %, CAS: 20694-39-7, Alfa Aesar) were used as metal precursors to prepare the LaMnO<sub>3</sub> perovskite-type oxides. Equimolar amounts of the nitrates were weighed and mixed in a beaker. Distilled water was used to prepare the aqueous nitrates solution. Citric acid (CA) was purchased from Alfa Aesar (> 99.5 %). The CA to total metal ions (La<sup>3+</sup> + Mn<sup>2+</sup>) molar ratio was fixed at 1.5. After citric acid addition, the solution was heated up to 80 °C under magnetic stirring to evaporate the excess water. The preparation was dried at 120 °C overnight as shown in Figure 2.2, then the resulting powder was transferred in a quartz tubular reactor (see Figure 2.5) and calcined under dynamic air flow (Figure 2.5) from 25 up to 200 °C (2 °C min<sup>-1</sup>), holding time 1h and subsequently from 200 °C up to 750 °C (5 °C min<sup>-1</sup>), holding time 2 h at 750 °C.

In order to investigate the effect of citric acid ratio on LaMnO<sub>3</sub> properties, the molar ratio of CA to total metallic ions (sum of La<sup>3+</sup> and Mn<sup>2+</sup>) was varied from 0.5 to 2. The weighted amount of CA was added at room temperature to the aqueous solution of La and Mn nitrates. The solution was heated up to 80 °C under magnetic stirring to evaporate the excess water, then it was dried at

120°C overnight. The resulting solid was treated **under static air in a muffle furnace** (Figure 2.6) at 200 °C (2°Cmin<sup>-1</sup>) for 1 h and, then, it was calcined from 200 °C up to 750°C (5°C min<sup>-1</sup>) holding time 2 h at 750 °C.

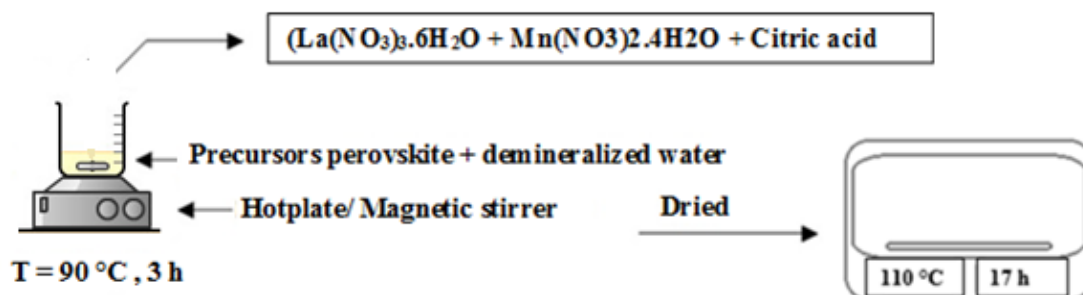


**Figure 2.2** Diagram of preparation of  $\text{LaMnO}_3$  (Sol-gel method).

### 2.1.3 OMS<sub>s</sub> (Solid-state method).

9.48 g of ( $\text{KMnO}_4$ , 99% , CAS : 7722-64-7, Sigma–Aldrich), and 22.05 g ( $\text{Mn}(\text{Ac})_2 \cdot 4\text{H}_2\text{O}$ , 99%, CAS:6156-78-1, Sigma–Aldrich) were homogeneously grounded in an agate mortar. The powder was further introduced in a capped glass bottle and maintained at 80 °C for 4 h. A black powder was received. After washing with deionized water, the solid was dried at 100 °C for 12 h as shown in Figure 2.3. Then, the resulting materials was finally calcined at 500 °C (the heating rate of 5 °C min<sup>-1</sup>) for 2 h in a quartz tubular reactor under air atmosphere.

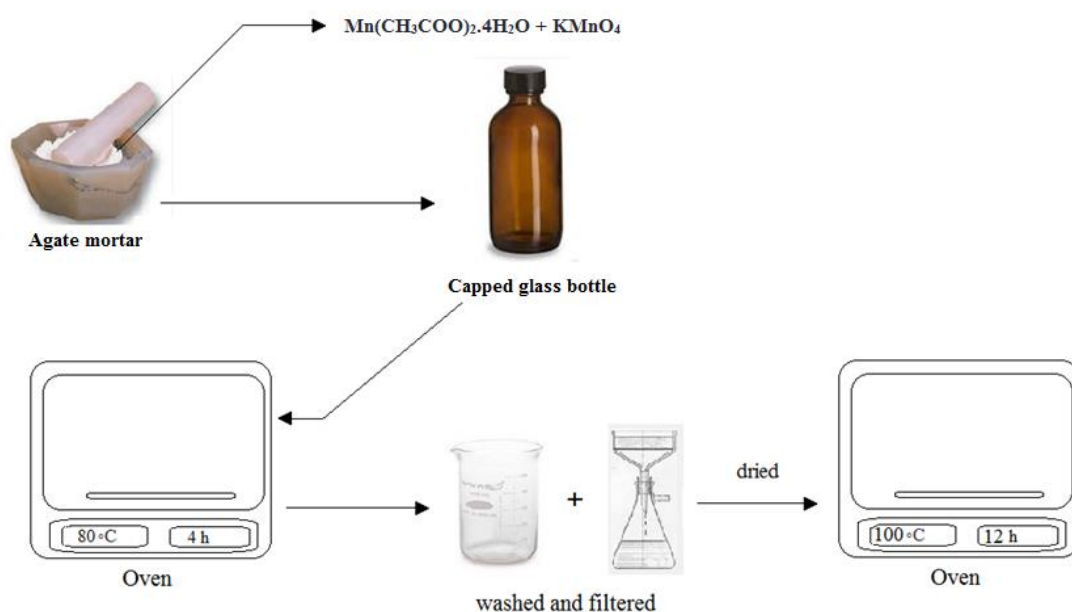


**Figure 2.3** Diagram of preparation of OMS (Solid-state method).

#### 2.1.4 OMS<sub>h</sub> (Hydrothermal method).

0.04 mole (6.76 g) of ( $\text{MnSO}_4 \cdot \text{H}_2\text{O}$ , 99 %, CAS: 10034-96-5, Sigma–Aldrich) was dissolved in 40 mL of water. The pH of the solution was adjusted to 1.0 using concentrated  $\text{HNO}_3$  (Sigma–Aldrich, 90%). An aqueous permanganate solution, prepared by dissolving 0.028 mole (4.40 g) of ( $\text{KMnO}_4$ , 99%, CAS: 7722-64-7, Sigma-Aldrich) in 150 mL of water, was then added slowly to the previous solution under vigorous stirring. The pH of the mixture was adjusted again to 1.0. The mixture was subsequently transferred in a glass liner and sealed in a stainless steel autoclave.

The autoclave was placed in an oven and maintained at  $100^\circ\text{C}$  for 16 hours. After cooling, the received black precipitate was filtered and then washed thoroughly with water. In Figure 2.4 the diagram of preparation of OMS<sub>h</sub> is displayed.

The sample was finally dried at  $120^\circ\text{C}$  for 16 hours and calcined at  $500^\circ\text{C}$  (the heating rate of  $5^\circ\text{C min}^{-1}$ ) for 2 h in a quartz tubular reactor under air atmosphere (see Figure 2.5).

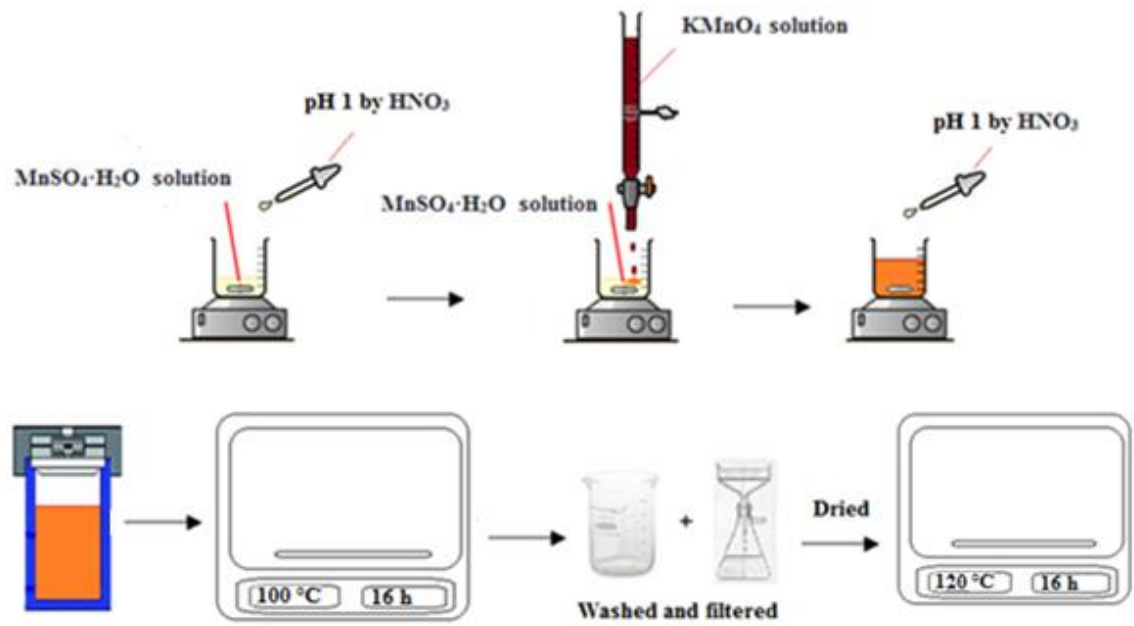


**Figure 2.4:** Diagram of preparation of OMS (Hydrothermal method).

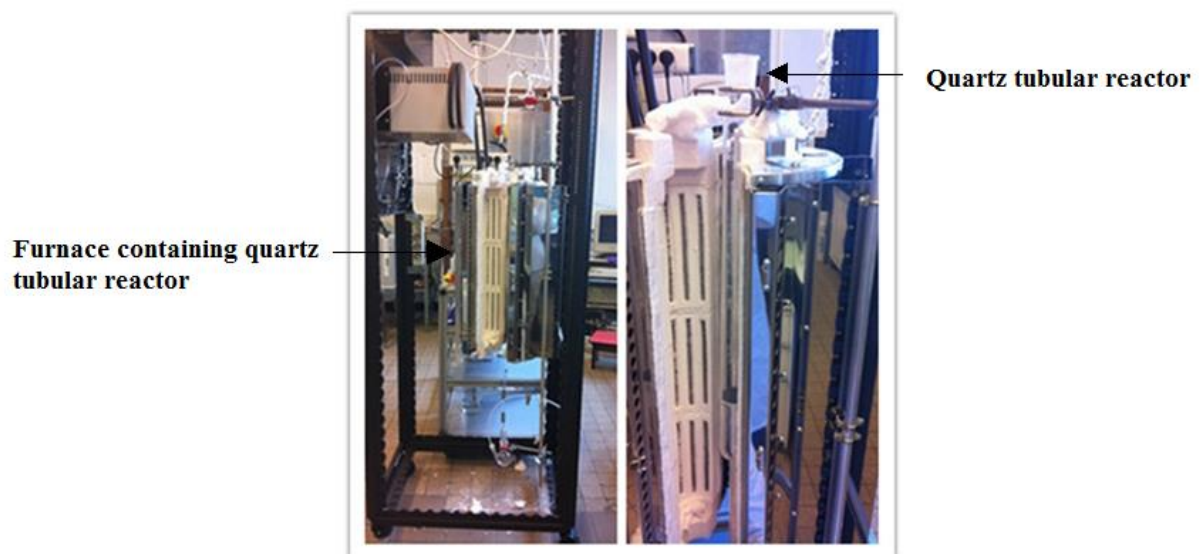


**Figure 2.5:** Bench of dynamic calcination.



**Figure 2.6:** Electric oven (static calcination).

## 2.2 Characterization of Catalysts.

### 2.2.1 X-ray diffraction (XRD).

X- Rays irradiating a crystal are scattered in a specular fashion by atoms in lattice planes of the crystal. X-rays scattered from successive crystallographic planes (hkl) will interfere constructively if the path length difference is equal to an integer multiple of the wavelength. The path difference between two waves undergoing constructive interference is given by  $2d\sin\theta$ , as showed in Figure 2.7. This a Bragg's law in the form:

$$n \lambda = 2d_{hkl} \sin\theta \quad (2.1)$$

Where  $\lambda$  is the wavelength of the X-ray and  $\theta$  is the incidence angle and the characteristic interplanar spacing of a set of planes with hkl Miller index.

Diffracted X-ray beams make an angle of  $2\theta$  with the incident beam. Because the crystallites can lie in all directions while still maintaining the Bragg condition, the reflections lie on the surface of cones whose semi-apex angles are equal the reflection angles  $2\theta$ . The diffraction pattern of a powder sample is taken in automatic diffractometer that use scintillation or CCD detectors to record angle and intensity of the diffracted beams.

The X-ray powder diffraction of a compound provides a convenient and characteristic fingerprint, which can be used in qualitative analysis. Values of spacing's line intensities can be compared with those listed in the Powder Diffraction File. The lattice parameters are readily obtained from  $d$ -spacing's with the help of computer programs that have been developed for this purpose. Powder X-ray diffraction data are also useful in the analysis of the relative concentration of different phases in a mixture and in the elucidation of phase diagrams. The phases of a mixture can be identified using the procedure describe above, and their proportions can be determined by comparing the intensities of the characteristic lines from each phase to those from a standard. Additionally, when phases are soluble in each other, the solubility limits can be determined by following the shifts of the cell parameters.

Powder X-ray diffraction (XRD) patterns were recorded on a Bruker D8 X-ray diffractometer at room temperature with  $\text{CuK}\alpha$  radiation ( $\lambda = 1.5418 \text{ \AA}$ ). The diffractograms were recorded for

$2\theta$  values comprised between  $10$  and  $80^\circ$  using a  $0.02^\circ$  step with an integration time of  $4$  s. The diffraction patterns have been indexed by comparison with the Joint Committee on Powder Diffraction Standards (JCPDS) files.

High temperature X-ray diffraction patterns were performed on a Bruker D8 diffractometer equipped with a special chamber HTK1200N. The radiation used was the same  $\text{CuK}\alpha$  and the conditions were  $2\theta = 5 - 80^\circ$ ,  $\text{step} = 0.02^\circ$ .

Low angle X-ray diffraction was performed on a Bruker AXS D5005 diffractometer using the  $\text{CuK}\alpha$  radiation ( $\lambda = 1.5418 \text{ \AA}$ ) as an X-ray source. The diffractograms were recorded for  $2\theta$  values comprised between  $0.5$  and  $10^\circ$  using a  $0.02^\circ$  step with an integration time of  $10$  s.

### **2.2.2 Determination of surface area by physisorption analysis.**

From a bulk material chemical bonds are broken leads surface formed. Getting increasing to chemisorption from the formation of new bonds with gas phase species. However, even in the absence of specific chemical reaction, the solid surface of a material will in general absorb a gas due to weak Van der Waals type interactions. The volume of adsorbed gaseous species will depend on both temperature and pressure as well as the surface area of the material. After saturation of the first monolayer of adsorbate, further adsorption may happened on the top of this layer, but with a lower heat of adsorption.

Determination of surface area by gas adsorption includes determination of the volume of an inlet gas (nitrogen) adsorbed on a solid surface as a function of increasing pressure. When pressure is reduced back to zero, any possible hysteresis is revealed by also due adsorbed volume. IUPAC is defined Six standard types of adsorption isotherm are shown in Figure 2.8. The Type I isotherm is typical of systems where there is strong chemisorption which saturates at one monolayer coverage. This type of isotherm may also be observed for microporous solids. Type II isotherms are typical of physisorption on finely divided non-porous solids where multilayers may build on

top of the first adsorbate monolayer. Type III and type V isotherms are characteristics of adsorption where the heat of adsorption onto the adsorbate (nitrogen) itself exceeds the heat of adsorption to the substrate (solid), as founded with water on hydrophobic materials. Type VI and V isotherms feature a hysteresis loop generated by the capillary condensation of the adsorbate in the mesopores of the solid. Finally, the rare type VI step-like isotherm is shown by nitrogen adsorption on some carbonaceous materials (Day, 1992).

If adsorption saturates at monolayer coverage, the surface area is easily determined from the Langmuir adsorption isotherm, which assumes that equilibrium coverage is achieved when rates of adsorption and desorption are equal (Satterfield, 1991). However, the most common method of measuring the surface area of powder is that developed by Brunauer, Emmett and Teller using the so called BET method (Brunauer, Emmett, & Teller, 1938). In essence, the BET isotherm is an extension of the Langmuir isotherm that also considers multilayer adsorption. As in the Langmuir approach, the heat of adsorption for the first monolayer is assumed independent of coverage. The heat of adsorption for layers other than the first is assumed equal to the heat of liquefaction of the adsorbed gas. Summation over an infinite number of adsorbed layers gives the final expression



$$\frac{P}{V(P_0 - P)} = \frac{1}{V_m C} + \frac{(C - 1)P}{V_m C P_0} \quad (2.2)$$

Where  $V$  is the volume of gas adsorbed at pressure  $P$ ,  $V_m$  is the volume of the monolayer,  $P_0$  is the saturation pressure of the adsorbate, and  $C$  is a constant related exponentially to the heats of adsorption and liquefaction of the adsorbate as  $C = e^{(q_1 - q_L)/RT}$

$$C = e^{(q_1 - q_L)/RT} \quad (2.3)$$

Where  $q_1$  is the heat of adsorption of the first layer and  $q_L$  is the heat of liquefaction of the adsorbate. In general, the higher the value of  $C$  the more the isotherm approaches the type II form and the more accurate the surface area can be determined.

According to the BET equation (2.3) defined above, plots of  $P/V(P_0 - P)$  versus  $P/P_0$  should give straight lines whose slope and intercept can be used to evaluate  $V_m$  and  $C$ . From volume of the monolayer ( $V_m$ ) and the cross-section area of the adsorbate, the total surface area of the adsorbent can be estimated. Additionally, from the adsorption-desorption isotherm, pore size distributions were obtained applying the Barrett-Joyner-Halenda (BJH) equation to the desorption branch of the isotherm. Total pore volume was estimated from the  $N_2$  uptake at a  $P/P_0$  value of 0.995.

- **Conditions for surface area determination.**

Nitrogen adsorption-desorption isotherms at  $-196^\circ\text{C}$  were obtained using a Micromeritics Tristar 3000 surface area and porosity analyser. Before measurement, the samples were outgassed at  $300^\circ\text{C}$  for 3 h. The specific surface area (SSA) of each sample was obtained using the Brunauer-Emmett-Teller (BET) method. The porous volume and the pore size distribution were calculated using the Barrett-Joyner-Halenda (BJH) method.

### **2.2.3 Elementary analysis (ICP-OES).**

Inductively-Coupled Plasma Optical Emission Spectroscopy (HORIBA Jobin Yvon Activa ICP-OES) used for elementary analysis. The sample first dissolved in an acid solution (mixture of HF and HCl solutions; mixture of HF, H<sub>2</sub>SO<sub>4</sub> and HNO<sub>3</sub> solutions) which is introduced into the spectrometer. Excited atoms and ions produced from each element emit a characteristic radiation whose intensity is measured. This intensity is then correlated to the amount of each element.

### **2.2.4 Thermal gravimetric analysis (TGA) and Differential thermal analysis (DTA).**

Thermogravimetric is a technique in which the mass of the sample is monitored against time or temperature while the temperature of the sample, in a specified atmosphere, is programmed. In order to enhance the steps in the thermogravimetric curve, the derivative thermogravimetric (DTG) trace is frequently drawn.

Differential thermal analysis (DTA) is a technique in which the difference in temperature between the sample and a reference material is monitored against time or temperature while the temperature of the sample, in a specified atmosphere is programmed. The DTA curve is generally a plot of the difference of temperature ( $\Delta T$ ) as the ordinate against the temperature (or time) as the abscissa.

- **Equipment and conditions**

Thermogravimetric and differential thermal analysis (TGA/DTA) were carried out over the dried catalysts (non-calcined catalysts) in the temperature range 25-900 °C (10 °C min<sup>-1</sup>) on a SETARAM Setsys Evolution 12 calorimeter, using 2–7 mg of sample, under flowing air.

### **2.2.5 Fourier Transform Infrared Spectroscopy (FT-IR).**

The FT-IR transmission spectra were recorded between 400 and 4000  $\text{cm}^{-1}$  for all the samples using a Spectrum Two FT-IR Spectrometer PerkinElmer.

### 2.2.6 Temperature programmed reduction (TPR).

Temperature-Programmed Reduction (TPR) determines the number of reducible species present on the catalyst surface and reveals the temperature at which the reduction of each species occurs. The basic reaction during  $\text{H}_2$ -TPR test shown in the following equation 2.4:



where MO is the metal oxide and M the metal. However, most of time the metal oxide is not reduced to metal but to lower oxidation states species.

The TPR analysis begins by flowing an analysis gas (typically hydrogen in an inert carrier gas such as nitrogen or argon) through the sample, usually at ambient temperature. While the gas is flowing, the temperature of the sample increased linearly with time and the consumption of hydrogen by adsorption/reaction is monitored. Changes in the concentration of the gas mixture downstream from the reaction cell are determined. This information yields the volume of hydrogen uptake.

- **Equipment and conditions.**

Temperature-programmed reduction (TPR), were performed in a commercial BELCAT-B unit with TCD detection. Samples (ca. 0.1 g), were loaded into a U-shaped quartz tube and pre-treated at 250°C for 30 min under Ar flow ( $50 \text{ cm}^3 \text{ min}^{-1}$ ). After cooling down, the temperature was ramped from room temperature to 900°C ( $10^\circ\text{C min}^{-1}$ ), using a reducing gas mixture consisting of 5 vol.%  $\text{H}_2$  in Ar ( $50 \text{ cm}^3 \text{ min}^{-1}$ ).  $\text{H}_2$  uptakes upon TPR experiments were calculated as follows:

$$H_2 \text{ uptake} = \frac{\text{mmol}_{H_2 \text{ consumed}}}{\text{mmol}_{Mn}} \quad (2.4)$$

The average oxidation state of Mn was calculated from the total consumption of hydrogen upon TPR experiments (total H<sub>2</sub>-uptake), considering the overall Mn loading in the catalysts and assuming that, the final oxidation state of Mn was +2.

### 2.2.7. X-ray photoelectron spectroscopy (XPS)

X-ray photoelectron spectroscopy (XPS) is a surface-sensitive quantitative spectroscopic technique that measures the elemental composition at the parts per thousand range, empirical formula, chemical state and electronic state of the elements that exist within a material. XPS spectra are obtained by irradiating a material with a beam of X-rays while simultaneously measuring the kinetic energy and number of electrons that escape from the top 0 to 10 nm of the material being analyzed. XPS requires high vacuum ( $P \sim 10^{-8}$  millibar) or ultra-high vacuum (UHV;  $P < 10^{-9}$  millibar) conditions, although a current area of development is ambient-pressure XPS, in which samples are analyzed at pressures of a few tens of millibar.

Commercial XPS instruments use either a focused 20- to 500-micrometer-diameter beam of monochromatic Al K<sub>α</sub> X-rays, or a broad 10- to 30-mm-diameter beam of non-monochromatic (polychromatic) Al K<sub>α</sub> X-rays or Mg K<sub>α</sub> X-rays. Because the energy of an X-ray with particular wavelength is known (for Al K<sub>α</sub> X-rays,  $E_{\text{photon}} = 1486.7$  eV), and because the emitted electrons' kinetic energies are measured, the electron binding energy of each of the emitted electrons can be determined by using an equation that is based on the work of Ernest Rutherford (1914):

$$E_{\text{binding}} = E_{\text{photon}} - (E_{\text{kinetic}} + \phi)$$

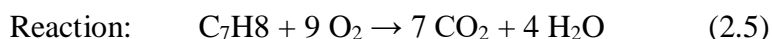
where  $E_{\text{binding}}$  is the binding energy (BE) of the electron,  $E_{\text{photon}}$  is the energy of the X-ray photons being used,  $E_{\text{kinetic}}$  is the kinetic energy of the electron as measured by the instrument and  $\phi$  is the work function dependent on both the spectrometer and the material. This equation is

essentially a conservation of energy equation. The work function term  $\phi$  is an adjustable instrumental correction factor that accounts for the few eV of kinetic energy given up by the photoelectron as it becomes absorbed by the instrument's detector.

- **Equipment and conditions.**

The X-ray photoelectron spectroscopy (XPS) analyses were performed with a VG Microtech ESCA 3000Multilab, equipped with a dual Mg/Al anode. As excitation source was used the unmonochromatized Al K $\alpha$  radiation (1486.6 eV). The sample powders were analysed as pellets, mounted on a double-sided adhesive tape. The pressure in the analysis chamber was in the range of 10<sup>-8</sup> Torr during data collection. The constant charging of the samples was removed by referencing all the energies to the C1s 2p set at 285.1 eV, arising from adventitious carbon. Analyses of the peaks were performed with the software CasaXPS. Atomic concentrations were calculated from peak intensity using the sensitivity factors provided with the software. The binding energy values are quoted with a precision of  $\pm 0.15$  eV and the atomic percentage with a precision of  $\pm 10\%$ .

### **2.3 Toluene catalytic oxidation.**



Toluene is one of the main volatile organic compounds (VOCs), which are released from the industrial processes. This component has adverse effects over human health. Total combustion of VOCs to produce harmless products such as CO<sub>2</sub> and H<sub>2</sub>O, is an effective way to remove them.

In this sense, the toluene total combustion can be performed by two ways: non-catalytic combustion and catalytic combustion. The latter allow to oxidize the toluene at lower temperature, and therefore, at safer and cheaper conditions.

The reaction rate can be expressed in relation to the appearance either of the product C, or relative to the disappearance of the reactant T, as follows:

$$r = -\frac{dn_T}{dt} = \frac{1}{7} \cdot \frac{dn_C}{dt} \quad (2.6)$$

where  $dn_T/dt$  is the toluene molar flow

The toluene molar flow can be calculated through the toluene conversion:

$$\frac{dn_T}{dt} = N_{T,0} \cdot \frac{dx_T}{dt} \quad (2.7)$$

where  $N_{T,0}$  is the toluene molar flow at the inlet

$x_T$  (toluene conversion) can be calculated by the following formula:

$$x_T = \frac{C_{CO_2}}{C_{CO_2}(\text{total toluene conversion})} \quad (2.8)$$

The toluene molar flow at the inlet can be calculated with the ideal gas law. In the case of catalytic reactions, the specific activity is obtained through the division of the reaction rate by the catalyst weight (100 mg).

### 2.3.1 Experimental set-up.



**Figure 2.9.** Experimental set-up.

1. Air gauges
2. Cooling bath with saturators
3. Saturator by-pass valve
4. Furnace
5. Mass flow controllers (Important note: you can read “Helium” and “Oxygen”, but this TP only works with compressed air. “Helium” controller monitors the airflow that goes to the saturation system, whereas “Oxygen” controller monitors an airflow).
6. Fixed-bed reactors
7. Reactor by-pass valves
8. Mass flow indicators
9. Temperature controller
10. Infrared analyzer

11. Temperature data logger
12. Gas chromatograph (GPC, PERKIN ELMER Clarus-500)

The reactive mixture, containing 1000 ppm  $C_7H_8$  and synthetic air(80/20 vol%) with a total flow of  $100 \text{ mL min}^{-1}$ , was introduced over the catalyst at room temperature before heating at a ramp rate of  $5^\circ\text{C min}^{-1}$  up to  $100^\circ\text{C}$  for 30 min, in order to stabilize the system. Subsequently, a second temperature ramp of  $2^\circ\text{C min}^{-1}$  was applied up to  $400^\circ\text{C}$ . Toluene and the possible organic products were analyzed using a gas chromatograph (GPC, PERKIN ELMER Clarus-500) equipped with both a flame ionization detector (FID) and thermal conductivity detector (TCD) and using a capillary column (Chromosorb101) for the organic reaction intermediates and a packing column (Carboxen 1000) for the permanent gas, respectively. In addition, CO and  $CO_2$  were continuously measured on-line by IR (ROSE- MOUNT Xstream analyzer). No other organic hydrocarbon was ever detected among the reaction products. After such a treatment, all catalysts were tested upon cooling the reactor down to room temperature as shown in figure 2.10. This sequence was repeated three times. Reproducible results were systematically obtained upon successive toluene oxidation runs. Moreover, the catalytic performance of the catalysts were evaluated upon long term toluene oxidation test, running for 24 h of toluene conversion, to evaluate the catalysts stability.

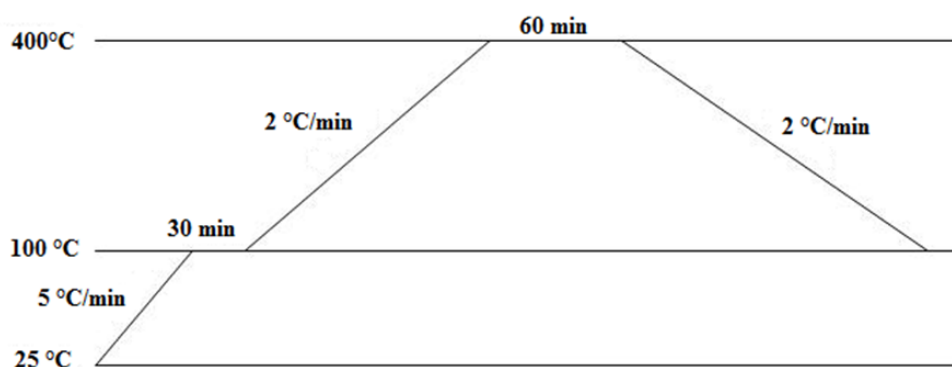


**Figure 2.10.** Temperature ramp.



## Chapter 3

**Manganese oxide-based  
catalysts for toluene oxidation.**

### 3.1 Introduction

This chapter focuses on the manganese oxide-based catalysts that are the most active ones (A. Gil, Gandía, & Korili, 2004; Mellan et al., 2013), although such oxides usually exhibit low specific surface area and poor thermal stability. An interesting way to obtain new manganese oxide-based structures (LaMnO<sub>3</sub>, OMS and Mn<sub>2</sub>O<sub>3</sub>), with smaller crystallite size (i.e. higher specific surface area) and improved stability, is the implementation of new preparation methods. This study allowed us to investigate their physicochemical properties and catalytic performances were evaluated in the catalytic oxidation of toluene.

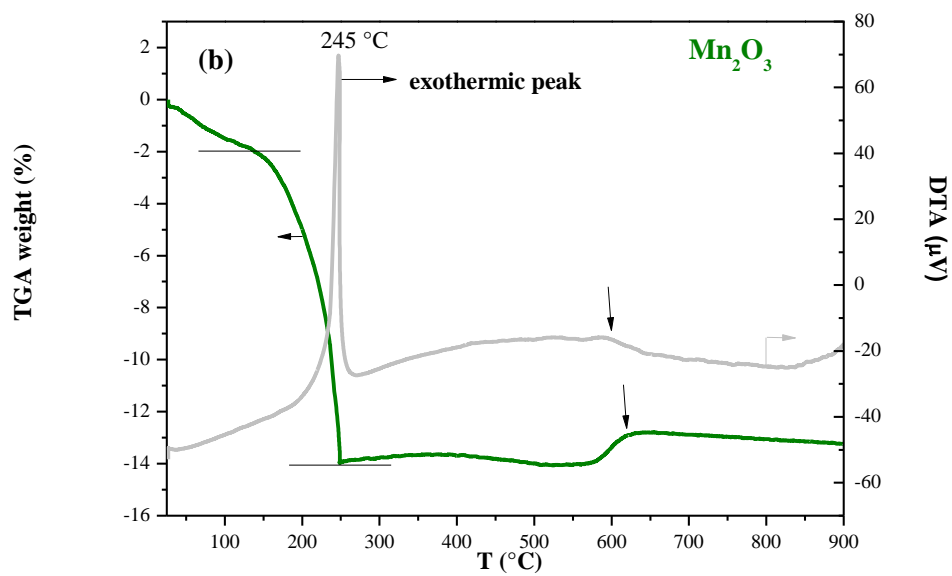
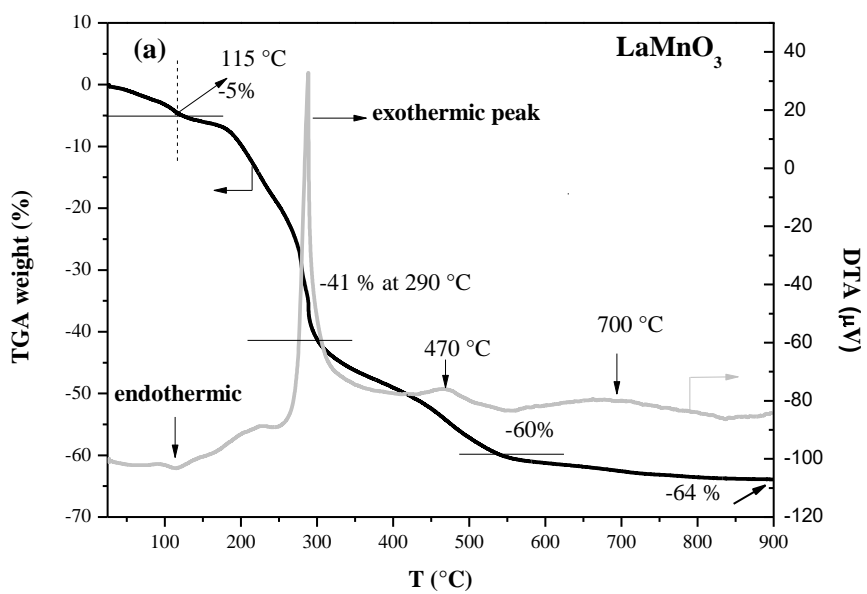
The results presented in this chapter constituted the first part of this PhD work and were published in part in (Sihaib et al., 2017)

### 3.2 Thermogravimetric and differential thermal analysis.

The thermal stability and crystallization of the prepared samples was studied using TGA/DTA analyses that were carried out under air in the temperature range 25–900°C on the dried catalysts (still containing the organic precursors). The results are presented in Figure 3.1. In the case of the LaMnO<sub>3</sub> perovskite catalyst, the TG plot shows a first small weight loss (-5wt%) around 115°C, corresponding to the removal of residual water in the gel, accompanied by a small endothermic peak in the DTA profile. Subsequently, a sharp exothermic peak with a concurrent pronounced weight loss of ca. 41 % was registered at 290°C, indicating that the decomposition of nitrate ions and citric acid contained in the gel occurred suddenly, in a single step, with the production of large amounts of gas such as H<sub>2</sub>O, CO<sub>2</sub> and NO<sub>x</sub> (Mali & Ataie, 2005). The second small exothermic peak observed at 470°C with an additional weight loss (-60 wt% on the overall) might be attributed to the decomposition of unreacted citric acid. At around 700°C, the crystallization of the perovskite structure occurs. Accordingly, a broadened exothermic peak is visible in the DTA with a further small weight loss. At the end, i.e. at 900°C the overall weight loss was -64 wt%.

In the case of  $\text{Mn}_2\text{O}_3$ , after a preliminary small weight loss (-2 wt%) at around 140°C, corresponding to the removal of residual water, a significant weight loss (-14%) due to the oxidation of the organic precursors was observed along with a sharp exothermic peak centred at 245°C. Upon increasing the temperature, the  $\text{Mn}_3\text{O}_4$  phase is oxidized to  $\text{Mn}_2\text{O}_3$ , with a small weight gain ca. 630°C accompanied by a broad exothermic peak (Larcher, Sudant, Patrice, & Tarascon, 2003).

As it concerns the TGA plots of  $\text{OMS}_h$  and  $\text{OMS}_s$ , slightly different thermal stabilities were observed, with an overall weight loss of 11 and 13 wt%, respectively. For both samples, four different steps can be detected in the TG curves: a first step from 25 to ca. 200°C where a weight loss (around 3-5.5 wt%) occurred. According to the literature (X. Chen, Shen, Suib, & O'Young, 2002; Ding et al., 2005; H. Huang, Meng, Labonte, Doble, & Suib, 2013; Luo et al., 2008; Schurz et al., 2009), loss of the water physically adsorbed on the surface or in the porous structure of the molecular sieves took place. Subsequently, a weight loss (ca. 3wt.%) was observed between 200 and 600°C as a result of the release of chemically adsorbed water and of any organic residual precursors if still present (Ding et al., 2005; Schurz et al., 2009). At the end of such step crystallization of the OMS structure occurs. In a third step, between 600-700°C, both OMS samples lost ca. 3 and 1.4wt% for  $\text{OMS}_h$  and  $\text{OMS}_s$ , respectively. This could be due to the evolution of the lattice oxygen species and the transformation of the OMS structure to  $\text{Mn}_2\text{O}_3$  (Luo et al., 2008; Schurz et al., 2009). Above 800°C (fourth step) due to a further oxygen release (weight loss of 1.7 and 2.5 wt% for  $\text{OMS}_h$  and  $\text{OMS}_s$ , respectively), transformation to  $\text{Mn}_3\text{O}_4$  took place (Luo et al., 2008; Schurz et al., 2009). Broad exothermic peaks in the temperature range 200-800 ° C. accompany the so far discussed weight losses.



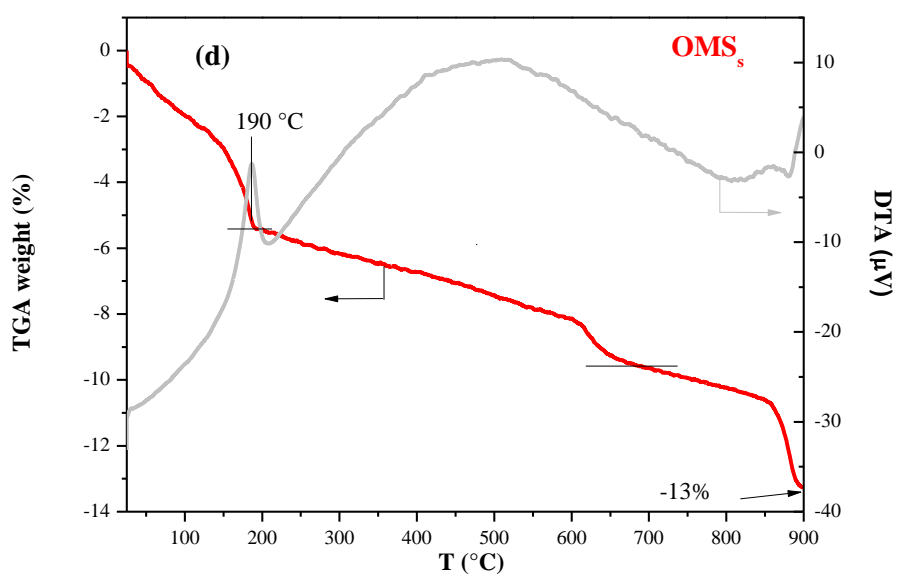
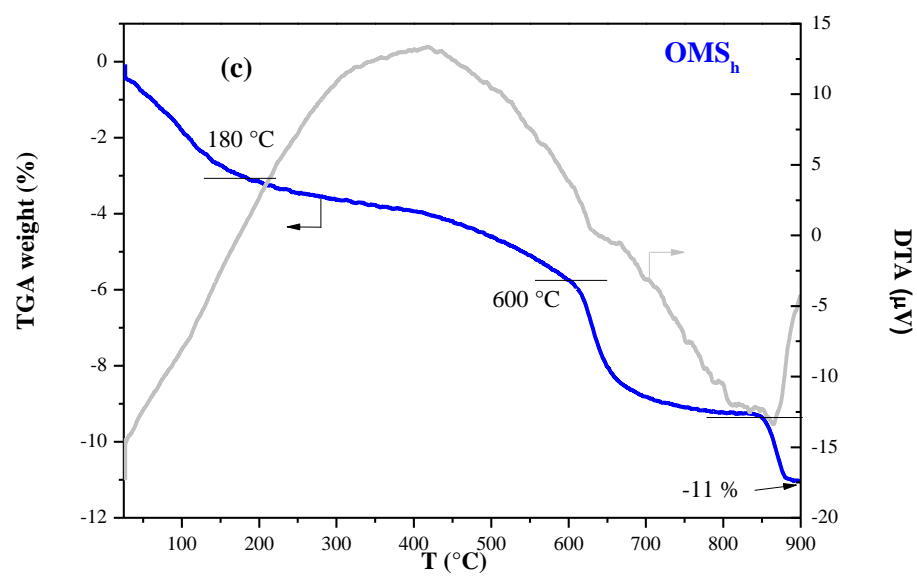


**Figure 3.1:** DTA and TGA profiles received under air for all catalysts (a)  $\text{LaMnO}_3$ , (b)  $\text{Mn}_2\text{O}_3$ , (c)  $\text{OMS}_h$  and (d)  $\text{OMS}_s$ .

### 3.3 XRD characterization

XRD patterns were acquired after calcination of the catalysts at 500°C, except in the case of LaMnO<sub>3</sub>, which required a higher calcination temperature for the crystallization of the perovskite structure (750°C). The XRD patterns are shown in Figure 3.2. The crystallite sizes ( $d_{\text{XRD}}$ ), calculated according to the Debye-Scherrer equation, are listed in Table 3.1 along with other physicochemical properties.

The crystal structure of each sample was deduced by comparison with the standard powder diffraction files (PDF) from the International Centre for Diffraction Data (ICDD). The diffraction lines of the LaMnO<sub>3</sub> sample were in good accordance with those of the reference La<sub>0.951</sub>Mn<sub>0.951</sub>O<sub>3</sub> (PDF 89-8775) with rhombohedral symmetry (space group R-3c). Diffraction line at  $2\theta = 28.98^\circ$  was assigned to the presence of La<sub>2</sub>O<sub>3</sub> (PDF 5-602). Moreover, diffraction peaks assignable to Mn<sub>3</sub>O<sub>4</sub> (PDF 2-1062) were also detected. Comparing with previous results (Zhang et al., 2014a), the perovskite structure and phase purity seem to depend on the synthesis conditions, such as on the citric acid to total metal ions molar ratio.

The XRD pattern for Mn<sub>2</sub>O<sub>3</sub> was also in good agreement with the reference Mn<sub>2</sub>O<sub>3</sub> sample (PDF 04-008-6383) with cubic symmetry. Characteristic diffraction lines of Mn<sub>3</sub>O<sub>4</sub> were also present.

The OMS<sub>h</sub> structure corresponded to K<sub>0.34</sub>Mn<sub>4</sub>O<sub>8</sub> (PDF 04-017-1191) with a tetragonal symmetry, whereas the OMS<sub>s</sub> structure corresponded to KMn<sub>8</sub>O<sub>16</sub> (PDF 00-012-0706), with tetragonal symmetry.

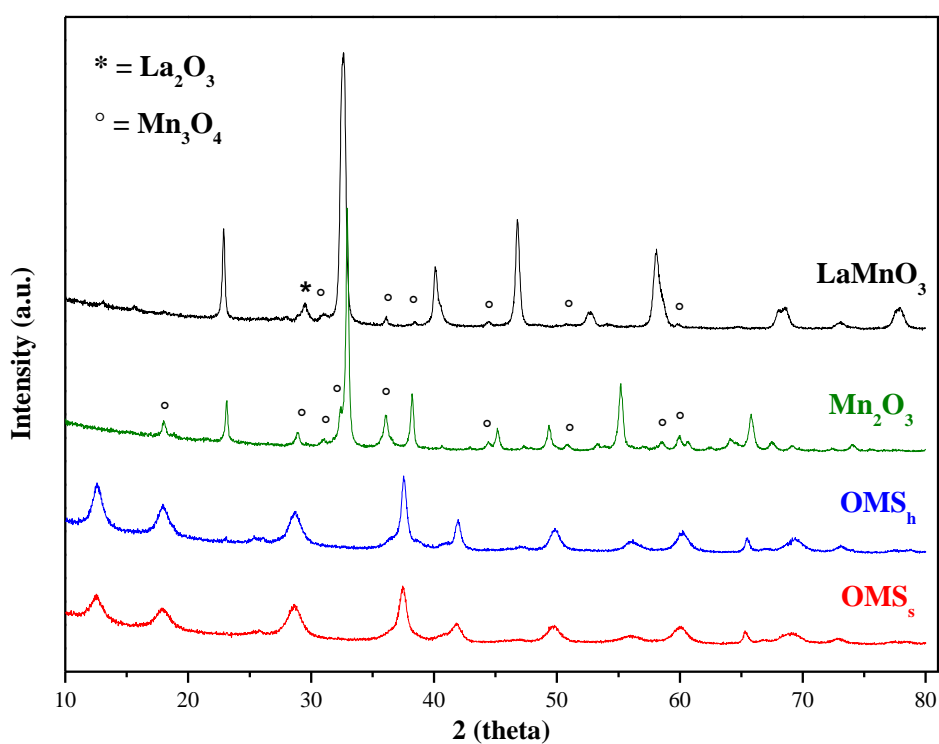
**Table 3.1** Physicochemical properties of the catalysts.

Catalyst	Pretreatment	SSA <sup>a</sup> (m <sup>2</sup> g <sup>-1</sup> )	pore volume (cm <sup>3</sup> g <sup>-1</sup> )	D <sub>p</sub> <sup>b</sup> (nm)	Mn (wt.%)	d <sub>XRD</sub> <sup>c</sup> (nm)
LaMnO <sub>3</sub>	750°C 2h in air	6	0.046	18	21.6	42.1
Mn <sub>2</sub> O <sub>3</sub>	500°C 2h in air	37	0.20	18	69.6	38.3
OMS <sub>h</sub>	500°C 2h in air	71	0.69	35	52.2	21.3
OMS <sub>s</sub>	500°C 2h in air	95	0.25	12	55.3	23.7

<sup>a</sup>SSA: Specific surface area

<sup>b</sup>D<sub>p</sub>: pore diameter

<sup>c</sup>d<sub>XRD</sub> Crystallite size

**Figure 3.2:** XRD patterns of catalysts LaMnO<sub>3</sub>, Mn<sub>2</sub>O<sub>3</sub>, OMS<sub>h</sub> and OMS<sub>s</sub>.

### 3.4 N<sub>2</sub> adsorption-desorption (at -196 °C)

N<sub>2</sub> adsorption–desorption isotherms and pore size distributions of the so far prepared catalysts are presented on Figure 3.3. The specific surface areas and pore volumes are summarized in Table 3.1. As observed from Figure 3.3, the N<sub>2</sub> adsorption–desorption isotherms were all characteristic of a mixed microporous and mesoporous structures with H3-type of hysteresis (Pawelec, La Parola, Navarro, Murcia-Mascarós, & Fierro, 2006; Xiaobin Wang et al., 2011). Such mixed porous structure was also evidenced by the pore-size distributions on Figure 3.3. While most pores were in the range 10–40 nm, additional micropores were systematically observed in minor amount in the range 1.0–4.0 nm.

As shown in Table 3.1, OMS<sub>S</sub> exhibited the largest specific surface area (95 m<sup>2</sup> g<sup>-1</sup>) but not the highest pore volume (0.25 cm<sup>3</sup> g<sup>-1</sup>). OMS<sub>H</sub> had a lower SSA (71 m<sup>2</sup> g<sup>-1</sup>) but the highest pore volume (0.69 cm<sup>3</sup> g<sup>-1</sup>). The physicochemical properties of the OMS catalysts, such as the specific surface area and the porous texture, appeared to be directly influenced by the preparation method. Mn<sub>2</sub>O<sub>3</sub> showed intermediate SSA and pore volume (37 m<sup>2</sup> g<sup>-1</sup> and 0.20 cm<sup>3</sup> g<sup>-1</sup>, respectively). Finally, LaMnO<sub>3</sub> had the lowest SSA and pore volume (6 m<sup>2</sup> g<sup>-1</sup> and 0.046 cm<sup>3</sup> g<sup>-1</sup>, respectively). However, one must take into consideration that LaMnO<sub>3</sub> was calcined at 750°C instead of 500°C.



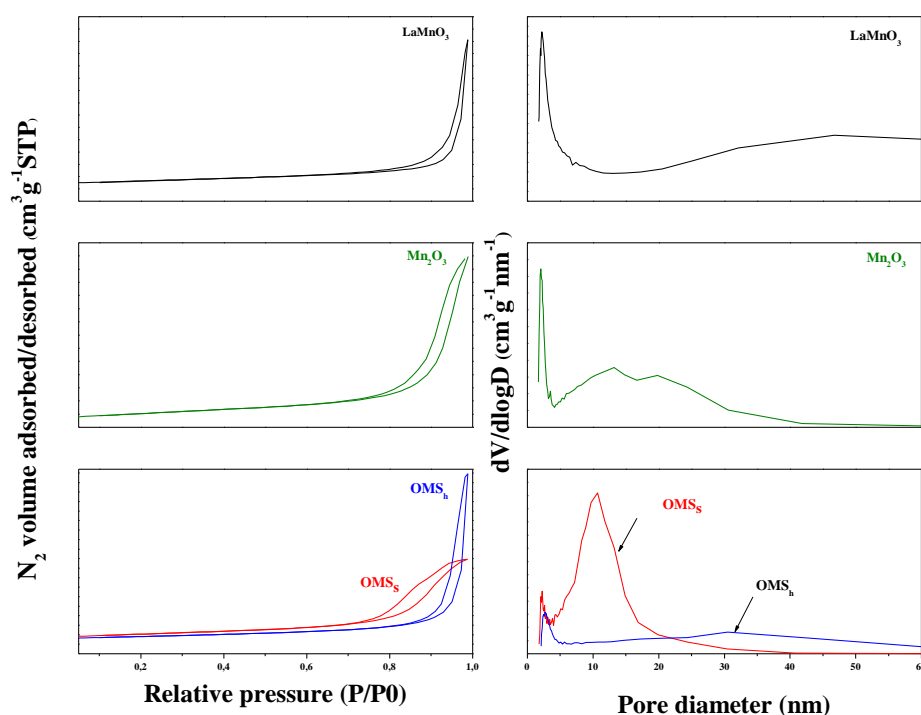


**Figure 3.3.** (a), (b) and (c)  $N_2$  adsorption–desorption isotherms and (d), (e) and (f) pore-size distributions of catalysts.

### 3.5 $H_2$ -TPR

In order to investigate the relative reducibility of the samples,  $H_2$ -TPR experiments were conducted.  $H_2$ -TPR profiles are shown on Figure 3.4. The corresponding  $H_2$  consumptions are summarized in Table 3.2. It could be observed that all catalysts showed two overlapping reduction peaks, except  $OMS_S$ , corresponding to a two-step reduction process. The first one occurred in the temperature range 200-600°C, while the second one occurred at higher temperature, above 700°C. In the case of  $Mn_2O_3$  both peaks appeared below 600°C.

The reduction profile registered for the  $LaMnO_3$  perovskite catalyst was in good agreement with our previous results (Zhang et al., 2014a) in terms of reduction temperature and  $H_2$  consumptions. A first broad peak ca. 400°C, with a small shoulder at about 360°C, was observed. Such small contribution of this late peak at low temperature was attributed to the

removal of some surface adsorbed oxygen species (Najjar, Lamonier, Mentré, Giraudon, & Batis, 2011; Zhang et al., 2014a). At higher temperature, larger H<sub>2</sub> consumption occurred, with the maximum centred at 414°C, which accounted for the reduction of Mn<sup>4+</sup> into Mn<sup>3+</sup>. The overall H<sub>2</sub> consumption in the temperature range 200-600°C was 0.229 mmol<sub>H<sub>2</sub></sub> mmol<sub>Mn</sub><sup>-1</sup> (see Table 3.2). By increasing the temperature further, an intense peak centred at 828 °C was noticed, related to the subsequent reduction of Mn<sup>3+</sup> into Mn<sup>2+</sup> (Najjar et al., 2011; Zhang et al., 2014a). The H<sub>2</sub>-uptake was higher (0.331 mmol<sub>H<sub>2</sub></sub> mmol<sub>Mn</sub><sup>-1</sup>) than the one registered around 400°C, indicating that the two oxidation states (Mn<sup>4+</sup> and Mn<sup>3+</sup>) coexist in the initial form of the catalyst.

For the Mn<sub>2</sub>O<sub>3</sub> nanocrystals, two peaks centred around 320 and 440°C were observed, corresponding to a stepwise reduction process from Mn<sub>2</sub>O<sub>3</sub> to Mn<sub>3</sub>O<sub>4</sub> and MnO (Iablokov, Frey, Geszti, & Kruse, 2010).

H<sub>2</sub>-TPR profiles for the two prepared OMS showed clear differences depending on the preparation method. Assuming that MnO was the final reduction state (Sun et al., 2011), in the case of sample OMS<sub>h</sub>, the first reduction peak at low temperature was assigned to the reduction of MnO<sub>2</sub>/Mn<sub>2</sub>O<sub>3</sub> to Mn<sub>3</sub>O<sub>4</sub>. The second peak ca. 800°C, with an H<sub>2</sub>-uptake of 0.253 mmol<sub>H<sub>2</sub></sub> mmol<sub>Mn</sub><sup>-1</sup>, was attributed to the reduction of Mn<sub>3</sub>O<sub>4</sub> to MnO (Sun et al., 2011; Sun, Liu, Chen, & Quan, 2015). The reduction profile of the OMS<sub>s</sub> sample consisted of one single peak, around 300 °C, which appeared at a lower temperature than that observed for OMS<sub>h</sub>. Similar results were reported for an OMS sample prepared by sol-gel method in the presence of maleic acid and methoxypolyethylene glycol (Yu et al., 2008).

**Table 3.2.** The results of quantitative analysis from H<sub>2</sub>-TPR profiles.

Catalyst	H <sub>2</sub> -uptake (mmol <sub>H2</sub> mmol <sub>Mn</sub> <sup>-1</sup> ) <sup>a</sup>			Mn average oxidation state
	200-600°C	700-900°C	Total	
LaMnO <sub>3</sub>	0.229	0.331	0.560	3.12
Mn <sub>2</sub> O <sub>3</sub>	0.418	-	0.418	2.84
OMS <sub>h</sub>	0.852	0.253	1.105	4.21
OMS <sub>s</sub>	0.646	-	0.646	3.29

<sup>a</sup>Calculated by TPR experiments

From the comparison between the two OMS samples, it was concluded that the Mn species in OMS<sub>s</sub> were more reducible at low temperatures compared to OMS<sub>h</sub>. Nevertheless, the total H<sub>2</sub> consumption was higher in the case of OMS<sub>h</sub> compared to OMS<sub>s</sub>, indicating that the average oxidation state of Mn was higher for OMS<sub>h</sub> (Table 3.2). The preparation method has a great influence over the oxidation state of Mn, showing OMS<sub>s</sub> a higher proportion of Mn<sup>3+</sup> compare to Mn<sup>4+</sup> (average oxidation state of 3.29), while in the case of OMS<sub>h</sub> Mn<sup>4+</sup> is the predominant oxidation state (average oxidation state of 4.21).

### 3.6. Catalytic performances in the catalytic oxidation of toluene

Catalytic activity measurements were performed as light-off experiments. The catalysts stability was further assessed upon consecutive light-off runs.

The catalyst stability was firstly evaluated by performing three consecutive catalytic runs for each catalyst. The conversion-temperature profiles (light-off curves) obtained over the different samples during the cooling ramp upon three consecutive cycles are shown on Figure 3.5. The results obtained upon the second catalytic run for all catalysts are shown in Figure 3.6. Temperatures for achieving 10, 50 or 90 % toluene conversion are listed in Table 3.3. These values were used to compare the catalysts performance.

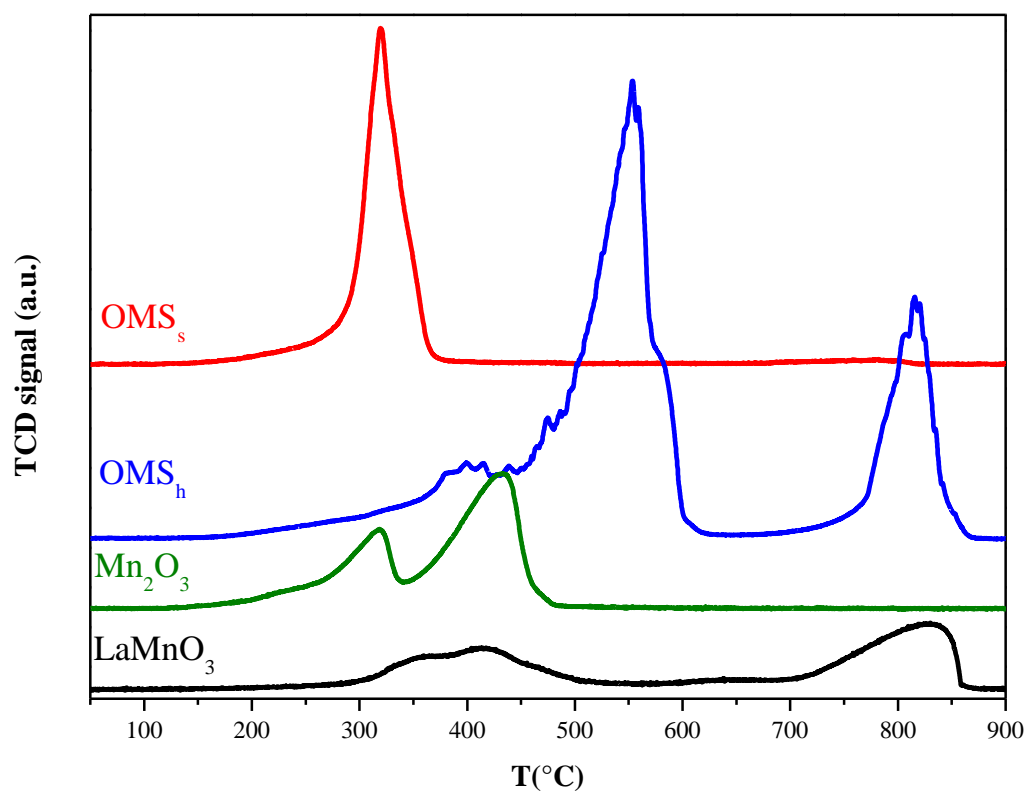


**Figure 3.4.** H<sub>2</sub>-TPR profiles of samples LaMnO<sub>3</sub>, Mn<sub>2</sub>O<sub>3</sub>, OMS<sub>h</sub>, OMS<sub>s</sub>.

Complete conversion of toluene could be successfully achieved below 350°C for all catalysts. The final products of the reaction were CO<sub>2</sub> and H<sub>2</sub>O. No other by-product was ever detected. The catalysts ranked as follows: OMS<sub>s</sub> > Mn<sub>2</sub>O<sub>3</sub> > OMS<sub>h</sub> > LaMnO<sub>3</sub>. OMS<sub>s</sub> exhibited the best catalytic activity in the toluene oxidation with T<sub>10</sub>, T<sub>50</sub> and T<sub>90</sub> values of 195, 234 and 272°C, respectively. Indeed, OMS<sub>s</sub> also exhibited the highest specific surface area and an optimum reducibility at low temperature. On the contrary, LaMnO<sub>3</sub> logically demonstrated the lowest catalytic performances since it exhibited the poorest reducibility at low-temperature and the lowest SSA.

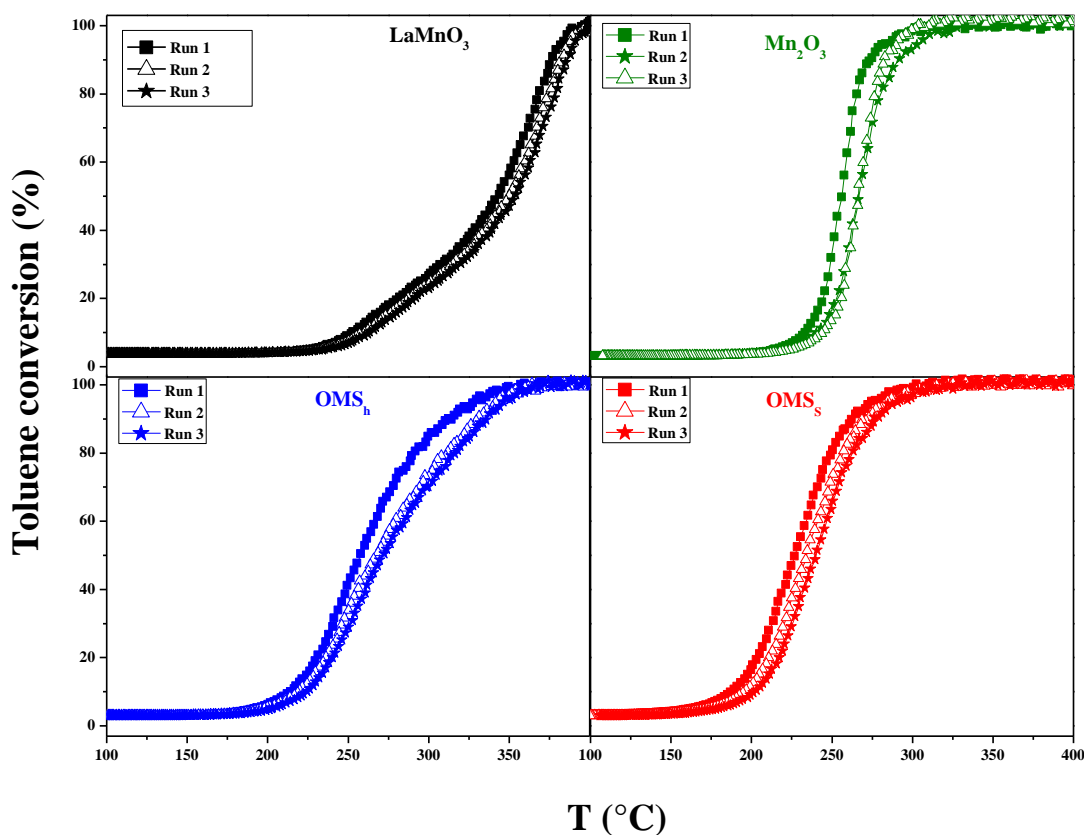


**Figure 3.5.** Evolution of the toluene conversion as a function of temperature, while cooling the reactor, upon three consecutive runs (a)  $\text{LaMnO}_3$  and  $\text{Mn}_2\text{O}_3$ , and (b)  $\text{OMS}_s$  and  $\text{OMS}_h$ .

Moreover, it could be observed that  $\text{OMS}_s$  performed better than  $\text{OMS}_h$ . Total toluene conversion into  $\text{CO}_2$  was achieved at  $300^\circ\text{C}$  over  $\text{OMS}_s$ ; while only 73% conversion was achieved over  $\text{OMS}_h$  at the same temperature. Comparing the specific surface areas of both OMS catalysts, one could conclude that the specific surface area had only a minor impact on the catalytic activity. In fact, toluene has a kinetic diameter of  $5.8\text{\AA}$ , while the OMS structures exhibit pore dimensions ca.  $4.6 \times 4.6\text{\AA}$ . Therefore, catalytic oxidation of toluene obviously occurs on the external surface of OMS. This could be the reason why the surface area would only have a minor influence. On the opposite,  $\text{OMS}_s$  clearly appeared to be more reducible than  $\text{OMS}_h$ , especially at low temperature. It has been pointed out in different studies that the

catalytic oxidation of toluene follows the Mars-Van Krevelen (MVK) mechanism when using transition metal oxides as catalyst (Doornkamp & Ponec, 2000; P. Liu et al., 2017). In this sense, the reaction mechanism involves different redox steps like the oxidation between toluene molecules and surface oxygen species, reduction of oxidized catalyst by toluene, and the oxidation of catalyst by oxygen to form surface oxygen species. For that reason, the ability of the catalyst to shift between different oxidation states at low temperature is expected to improve the catalytic behaviour. In conclusion, the solid state method is to be preferred for the synthesis of highly active OMS-based catalysts.

Stability of the catalysts, reported in Figure 3.5 as the evolution of toluene conversion versus temperature during the cooling ramp for three consecutive cycles, was very similar for all the catalysts, showing all the samples a decrease in the  $T_{50}$  values of about 12°C after three cycles (Table 3.3).

**Table 3.3.** Catalytic performances of the catalysts in the oxidation of toluene. Data were collected upon cooling.

Catalysts	1st Run			2nd Run			3rd Run		
	$T_{10}^{\circ C^1}$	$T_{50}^{\circ C^1}$	$T_{90}^{\circ C^1}$	$T_{10}^{\circ C^1}$	$T_{50}^{\circ C^1}$	$T_{90}^{\circ C^1}$	$T_{10}^{\circ C^1}$	$T_{50}^{\circ C^1}$	$T_{90}^{\circ C^1}$
<b>LaMnO<sub>3</sub></b>	244	283	320	250	289	326	256	295	332
<b>Mn<sub>2</sub>O<sub>3</sub></b>	233	256	274	240	266	292	244	266	282
<b>OMS<sub>h</sub></b>	213	257	311	219	267	330	224	271	336
<b>OMS<sub>s</sub></b>	188	227	263	195	234	272	202	240	276

<sup>1</sup> Light-off temperature at 10, 50 and 90 % toluene conversion, respectively.

The catalytic stability and durability of the catalysts were also evaluated under steady-state conditions at 25% of toluene conversion after the first run. Figure. 3.7 illustrates toluene conversion as a function of time on stream (24 h) for all catalysts. LaMnO<sub>3</sub> and OMS<sub>s</sub> catalysts exhibited relative good catalytic stability and durability, with only a slight decrease in toluene conversion during the first 6 h (from 25% to 23%). However, Mn<sub>2</sub>O<sub>3</sub> and OMS<sub>h</sub> catalysts were

deactivated most quickly during this 6 h, at which point 21 and 15% of toluene conversion, respectively were noted.

Comparison between reported and our own results in toluene oxidation appear in Table 1.2, where the activity of different Mn containing catalysts and one commercial Pd/Al<sub>2</sub>O<sub>3</sub> catalyst are resumed. It can be observed that our results are comparable to that reported for the different Mn containing catalysts, being the OMS<sub>s</sub> one of the most active.

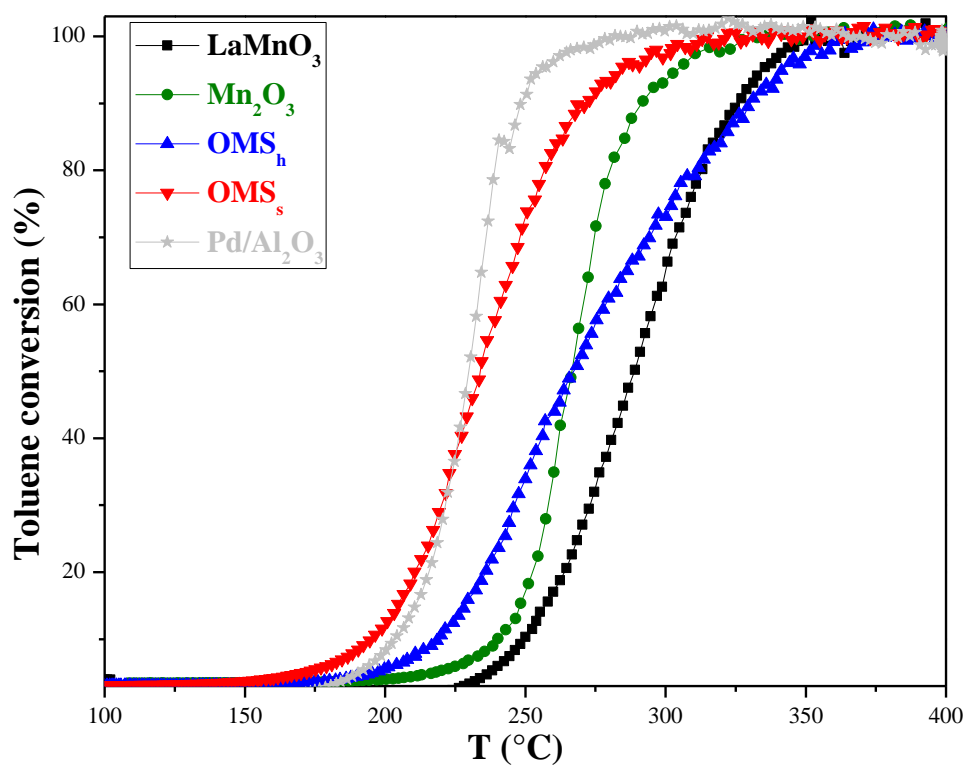


**Figure 3.6.** Toluene conversion versus temperature during second consecutive run (cooling ramp).

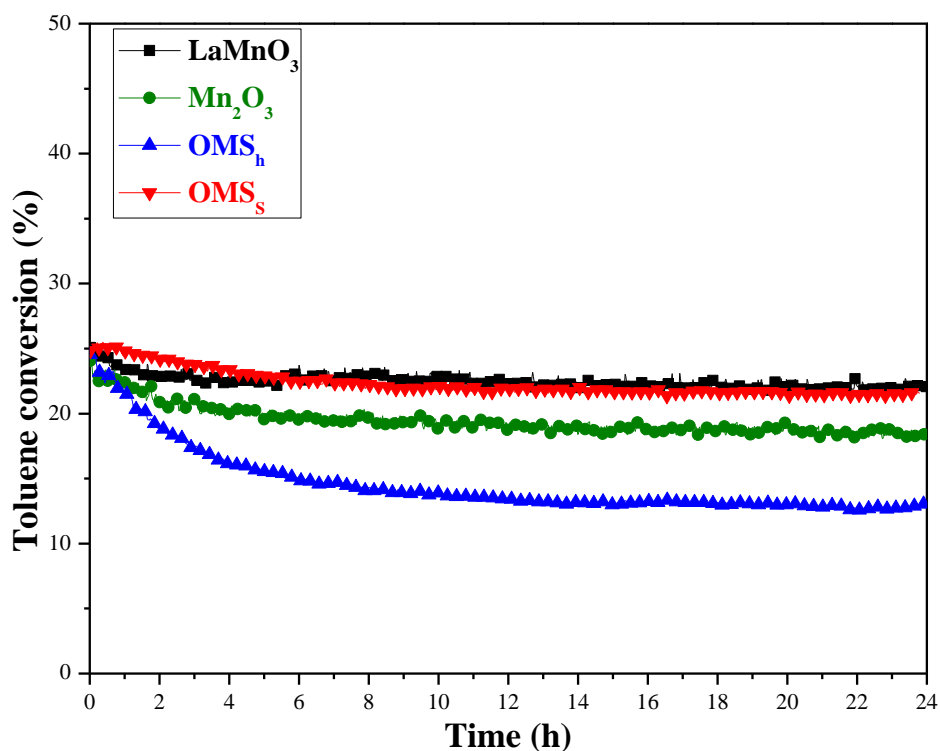


**Figure 3.7.** Lifetime toluene oxidation test conducted at 25% of toluene conversion during 24h.

### 3.7. Kinetic study

A kinetic study of the toluene oxidation was performed by using 100 mg of catalyst placed over a quartz wool plug in a U-shaped reactor. The reactive mixture, containing 1000 ppm C<sub>7</sub>H<sub>8</sub> and synthetic air (80/20vol.%) with a total flow of 100 mL min<sup>-1</sup> was introduced over the catalyst at room temperature before heating at ramp rate of 5 °C min<sup>-1</sup> up to 100°C for 30 min to stabilize the system. Subsequently, a second temperature ramp of 2 °C min<sup>-1</sup> was applied up to 400 °C. Toluene conversion was calculated by Eq. (2.1). The following reaction was considered:



Experimental catalytic activity of the C<sub>7</sub>H<sub>8</sub> transformation was defined by the experimental reaction rate,  $r_{\text{Exp}}$ , expressed as mol s<sup>-1</sup> g<sup>-1</sup> of Mn (Eq. (3.2)):



$$r_{exp} = \frac{Q_v \cdot \left( \frac{P_{T_0} - P_T}{P} \right) \cdot \left( \frac{1}{T * R} \right)}{m_{Mn}} \quad (3.2)$$

Where  $Q_v$  is the total flow of the gas stream  $L s^{-1}$ ;  $P_T$  is the partial pressure of toluene;  $P_{T_0}$  is the partial pressure of toluene in the feed gas;  $P$  is the total pressure in the reactor (1 atm);  $T$  is the temperature at which the volume flow was measured (298 K);  $R$  is the ideal gas constant ( $0.082 \text{ atm L K}^{-1} \text{ mol}^{-1}$ ); and  $m_{Mn}$  is the mass in grams of Mn in the catalyst bed used.

Experimental kinetic data obtained for catalysts  $LaMnO_3$ ,  $Mn_2O_3$ ,  $OMS_h$  and  $OMS_s$  in the oxidation of toluene were used for evaluating the parameters of the power-law rate,  $r_{Th}$ , represented by equation (3.3): pre-exponential factor of the kinetic constant, the activation energy and the partial order of reactions (Behar et al., 2015; Duprat, 2002):

$$r_{Th} = k' P_{O_2}^{n_{O_2}} P_{Tol}^{n_{Tol}} \quad (3.3)$$

Since the partial pressure of  $O_2$  was in excess respect to that of toluene, this equation could be simplified to the next one:

$$r_{Th} = k P_{Tol}^{n_{Tol}} \quad (3.4)$$

Where  $k = k' P_{O_2}^{n_{O_2}}$ ;  $P_{Tol}$  is the partial pressure of toluene; and  $n_{Tol}$  is the partial order of reaction (toluene). The apparent rate constant ( $k$ ) was considered to be temperature dependent according to the Arrhenius equation:

$$k = k_0 \exp\left(\frac{-E_a}{RT}\right) \quad (3.5)$$

Where  $E_a$  is the activation energy ( $J \text{ mol}^{-1}$ );  $R$  is the gas constant ( $J \text{ mol}^{-1} \text{ K}^{-1}$ );  $k_0$  is the pre-exponential factor; and  $T$  is the reaction temperature (K).

The tubular flow reactor with a packed catalyst bed that was used in this work was modelled with a pseudo homogeneous, one-dimensional model. Isothermal conditions and no pressure drops were assumed. Therefore, the following expression for the axial flow profiles through the reactor for the fed gases can be used:

$$\frac{dF_T}{dm_{Mn}} = -r_{Th} \quad (3.6)$$

where  $F_T$  represents the flow-rate of toluene in any point of the fixed bed.

A VBA-Excel application was developed to solve this model (de la Osa, De Lucas, Romero, Valverde, & Sánchez, 2011; S. Gil et al., 2011). The Bader-Deufhard method was used in the evaluation of the set of ordinary differential equations (de la Osa et al., 2011), whereas the Marquard-Levenberg algorithm was used in the nonlinear regression procedure (S. Gil et al., 2011; Marquardt, 1963). The weighted sum of the squared differences between the observed and the calculated outlet flow rates was minimized (de la Osa et al., 2011):

$$SSQ = \sum_i (F_{T,exp} - F_{T,th})^2 \quad (3.7)$$

where  $SSQ$  is the sum of square differences;  $F_{T,exp}$  and  $F_{T,t}$  denote the experimental and theoretical molar effluent of toluene, respectively.

An F-test is a statistical test in which the test statistic has an F-distribution under the null hypothesis. It was used for comparing statistical models that have been fitted to a data set, in order to identify the model that best fits the population from which the data were sampled. The procedure was based on the comparison between the tabulated F value (F-test) and  $F_c$ , which is defined by the following equation [20]:

$$F_c = \frac{\text{regression sum of squares/degree of freedom}}{\text{residual sum of squares/degrees of freedom}} \\ = \frac{\sum_{i=1}^N \{ [f(x, \beta)]^2 i / p \}}{\sum_{i=1}^N \{ [y - f(x, \beta)]^2 i / (N - p) \}} \quad (3.8)$$

Note that if  $F_c > F(p, N-p, 1-\alpha)$  (assuming a value of  $\alpha = 0.05$ , 95% confidence level), the regression is considered to be meaningful, although there is no guarantee that the model is statistically suitable. To avoid this contradiction, the meaningfulness of the parameters in the model must also be evaluated by using the *t*-test, which verifies whether the estimation of  $\beta_i$  (bfi)

differs from a reference value (generally zero). Thus, a parameter will be always meaningful when the following inequality can be achieved:

$$t_{c_i} = \frac{|b_{fi}|}{\sqrt{[V(b_f)]_{ii}}} > t \left( N - p; 1 - \frac{\alpha}{2} \right) \quad (3.9)$$

Where  $[V(b_f)]_{ii}$  represents the diagonal  $j$ th term of the covariance matrix. Finally, the confidence interval of the parameter  $\beta_i$  is defined by:

$$b_{fi} - t \left( N - p; 1 - \frac{\alpha}{2} \right) \sqrt{[V(b_f)]_{ii}} \leq \beta_j \leq b_{fi} + t \left( N - p; 1 - \frac{\alpha}{2} \right) \sqrt{[V(b_f)]_{ii}} \quad (3.10)$$

Where  $F_C$ : function defined by Eq. (3.8);  $t_{c_i}$ : function defined by Eq. (3.9);  $b$ : estimate of  $\beta$ ;  $V(b)$  covariance matrix;  $N$ : total number of experiments;  $x$ : set of independent variables in  $f(x, \beta)$  mode;  $y$ : experimental dependent variable;  $f$ :  $(x, \beta)$ , mathematical model;  $p$ : number of parameters in a model;  $i$ : the species.

**Table 3.4.** Statistical meaningful of kinetic model parameters.

Catalyst	Parameters	Estimated values	$t_c$	$t_{test}$	$t_c/t_{test}$	Statistical significance
LaMnO <sub>3</sub>	$ko$ (mol s <sup>-1</sup> g Mn <sup>-1</sup> bar <sup>-nTol</sup> )	9.86E+08	4.11	1.96	2.1	Yes
	Ea (J mol <sup>-1</sup> )	123312	174.6	1.96	89.1	Yes
	$n_{Tol}$	1.45E+00	108.9	1.96	55.5	Yes
Mn <sub>2</sub> O <sub>3</sub>	$ko$ (mol s <sup>-1</sup> g Mn <sup>-1</sup> bar <sup>-nTol</sup> )	1.90E+08	3.036	1.96	1.55	Yes
	Ea (J mol <sup>-1</sup> )	133680	184.5	1.96	94.13	Yes
	$n_{Tol}$	9.3E-01	27	1.96	13.77	Yes
OMS <sub>h</sub>	$ko$ (mol s <sup>-1</sup> g Mn <sup>-1</sup> bar <sup>-nTol</sup> )	3.70E+11	2.187	1.96	1.11	Yes
	Ea (J mol <sup>-1</sup> )	126520	104.4	1.96	53.26	Yes
	$n_{Tol}$	1.9E+00	78.12	1.96	39.85	Yes
OMS <sub>s</sub>	$ko$ (mol s <sup>-1</sup> g Mn <sup>-1</sup> bar <sup>-nTol</sup> )	8.80E+07	1.15	1.96	0.58	Not
	Ea (J mol <sup>-1</sup> )	96920	45.12	1.96	23	Yes
	$n_{Tol}$	1.9E+00	34.4	1.96	17.55	Yes

In all cases, the regressions were considered meaningful. Table 3.4 provides the corresponding model parameters and t tests.

Comparison of SSQ values identifies Marquardt-Levenberg algorithm model. The t-test showed that the regression could be considered meaningful, because the value of the  $t_c/t_{test}$  ratio was greater than 1.

In Figure 3.8 the experimental and predicted molar flow of toluene for all the catalysts tested are represented. It can be observed an excellent good agreement between the experimental and predicted data even at high temperatures. This result and the fact that high values of the activation energies were estimated by nonlinear regression for all the catalysts would clearly indicate that the reaction is the only rate-limiting step.

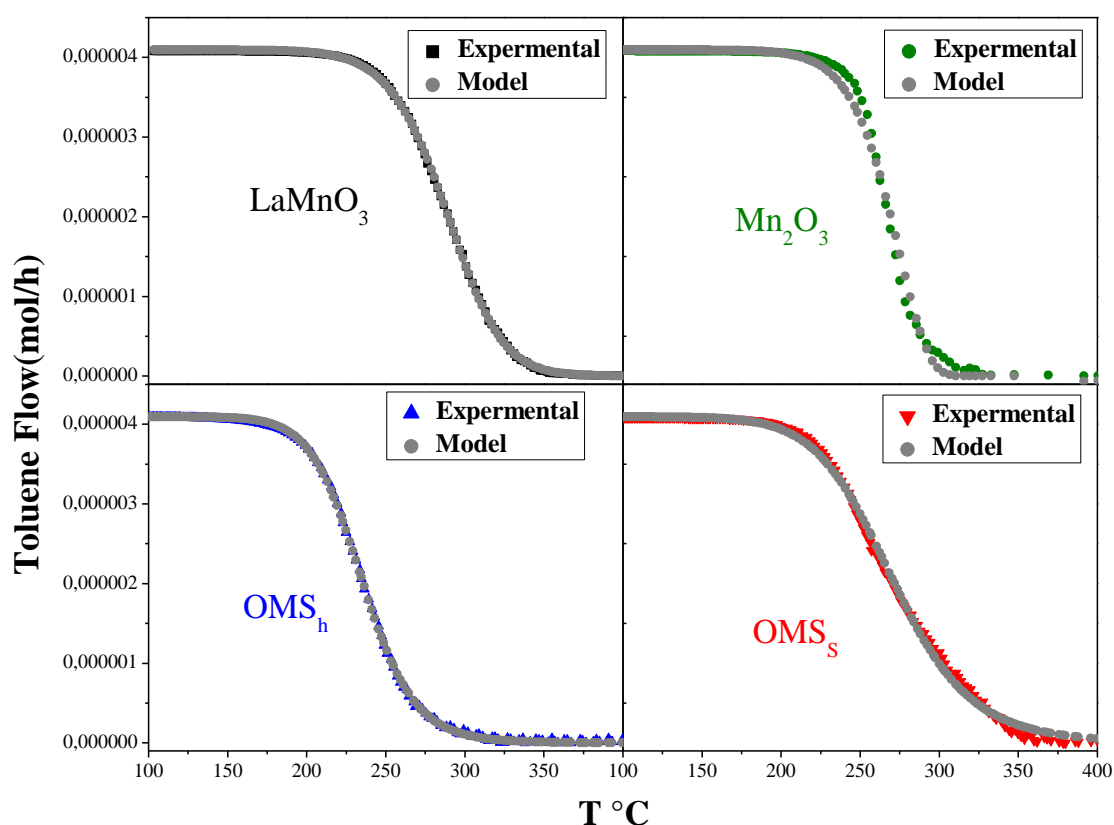


**Figure 3.8.** Comparison between experimental and predicted toluene molar flow for catalysts

LaMnO<sub>3</sub>, Mn<sub>2</sub>O<sub>3</sub>, OMS<sub>h</sub> and OMS<sub>s</sub>.

### 3.8. Conclusions.

Four different catalysts based on manganese oxide ( $\text{LaMnO}_3$ , OMS and  $\text{Mn}_2\text{O}_3$ ) were prepared using several preparation routes. For the synthesis of OMS, two different preparation routes, solid state (OMSs) and hydrothermal method, were employed. The OMSs catalyst, prepared via solid-state method, exhibited the highest catalytic activity for the complete oxidation of toluene at low temperature, which could be related to its higher reducibility and higher specific surface area. The catalytic performances of the catalysts followed the order:  $\text{OMS}_s > \text{OMS}_h > \text{Mn}_2\text{O}_3 > \text{LaMnO}_3$ . In all cases the reaction started at around 200–250 °C with full conversion of toluene being achieved below 350°C. This trend was in agreement with the trend in the evolution of the specific surface area. Also, the loading (wt%) of the active element of the catalysts (Mn) followed a similar trend than the catalytic activities except for  $\text{Mn}_2\text{O}_3$ , which is the one with the highest loading of Mn but its surface area is lower than half of the surface area of the catalyst with the highest catalytic activity (OMSs). All catalysts demonstrated to be stable upon three consecutive runs. A comparison between the present results with the performances of different Mn-containing catalysts, already reported in the literature, show comparable activity with our systems,  $\text{OMS}_s$  being the most active one. Tests of toluene oxidation over a reference  $\text{Pd}/\text{Al}_2\text{O}_3$  catalyst were also performed for comparison purposes. Although for such Pd catalyst, a  $T_{50}$  value slightly lower than the one of  $\text{OMS}_s$  was found, the  $\text{OMS}_s$  was more active at low temperature. A kinetic study was carried out and a model was developed with an excellent good agreement between the experimental and predicted data even at high temperatures. For all the catalysts, the reaction is the only rate-limiting step.

## Chapter 4

**The effect of citric acid ratio  
on  $\text{LaMnO}_3$  properties.**

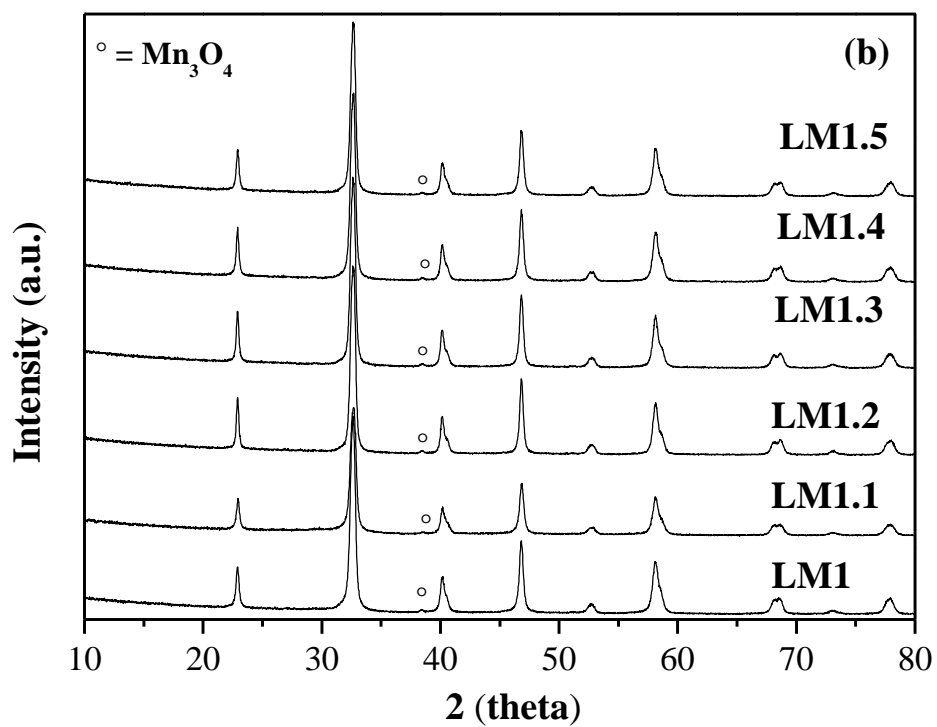
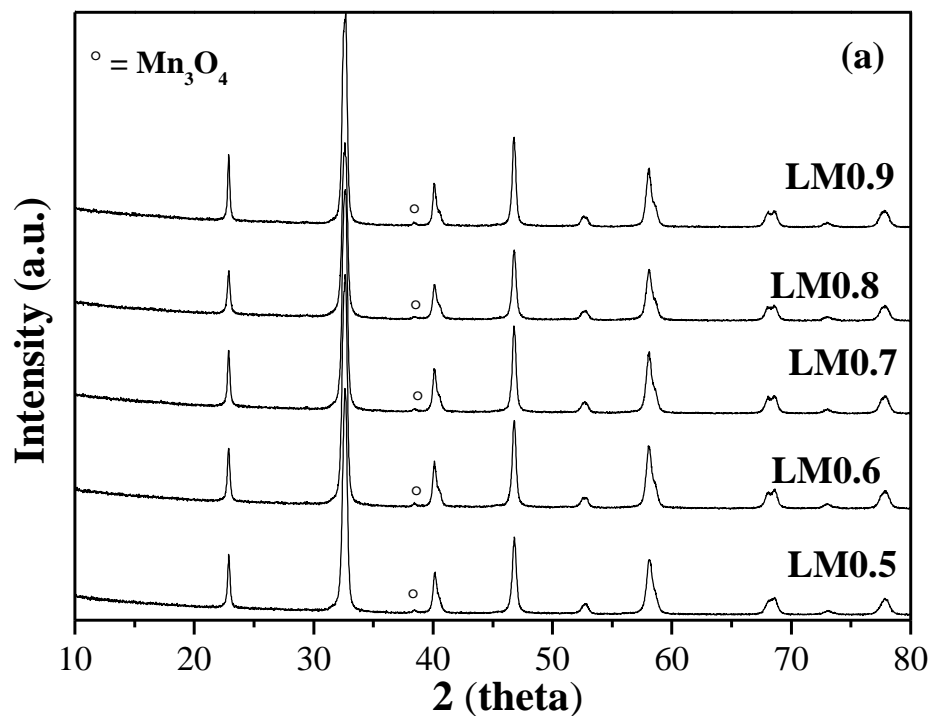
## 4.1 Introduction

This chapter focuses on catalytic properties improvement of LaMnO<sub>3</sub>. Although, as shown in Chapter 3, LaMnO<sub>3</sub> presented the lowest toluene catalytic activity in the range of temperature 100-400 °C, it exhibited relatively good catalytic stability and durability under steady-state conditions at 25% of toluene conversion as a function of time on stream (24 h). For that reasons, it is worth investigating the effects of the preparation method and the experimental conditions on the physicochemical properties and the catalytic performances of LaMnO<sub>3</sub> perovskite. With the purpose to study the effect of the citric acid (CA) concentration on the catalytic properties of the LaMnO<sub>3</sub> perovskites, samples with a CA to (La<sup>3+</sup> + Mn<sup>2+</sup>) ions molar ratio ranging from 0.5 to 2 have been prepared.

## 4.2. XRD characterization

XRD patterns of catalysts LaMnO<sub>3</sub> calcined at 750°C are shown in Figure 4.1 and the physicochemical properties are listed in Table 4.1. The diffraction lines of the LaMnO<sub>3</sub> phase were in good agreement with those of the reference La<sub>0.951</sub>Mn<sub>0.951</sub>O<sub>3</sub> (PDF 89-8775) with rhombohedral symmetry (space group R-3c), confirming our previous results (Sihab et al., 2017; Zhang et al., 2014b). Moreover, along with the characteristic peaks of the perovskite phase, at high concentration of CA, namely for molar ratio in the range 1.6-2.0, a small peak appeared at  $2\theta$  29 °, attributed to La<sub>2</sub>O<sub>3</sub> phase (PDF 5-602), in agreement with the literature (Ghiasi, Malekzadeh, & Ghiasi, 2013). The highest amount of La<sub>2</sub>O<sub>3</sub> impurity was detected at CA to total metal ions (La<sup>3+</sup> + Mn<sup>2+</sup>) molar ratio equal to 2.0 (see Figure. 4.1 C). A careful inspection of the XRD patterns of samples (LM1.6-LM2) revealed also the presence of very small features, at  $2\theta$  38.5 °, ascribed to the phase Mn<sub>3</sub>O<sub>4</sub> (PDF 2-1062). In the overall, the phase purity of LaMnO<sub>3</sub> perovskite was quite high for CA molar ratio values in the range 0.5-1.5. The crystallite size of LaMnO<sub>3</sub> of the prepared samples were calculated using Scherrer equations and are listed in Table 4.1. The average crystal size varied between 18 and 30 nm, with the

smallest sizes at CA to total metal ions ( $\text{La}^{3+} + \text{Mn}^{2+}$ ) molar ratio between 1.1 and 1.5 (see Table 4.1).





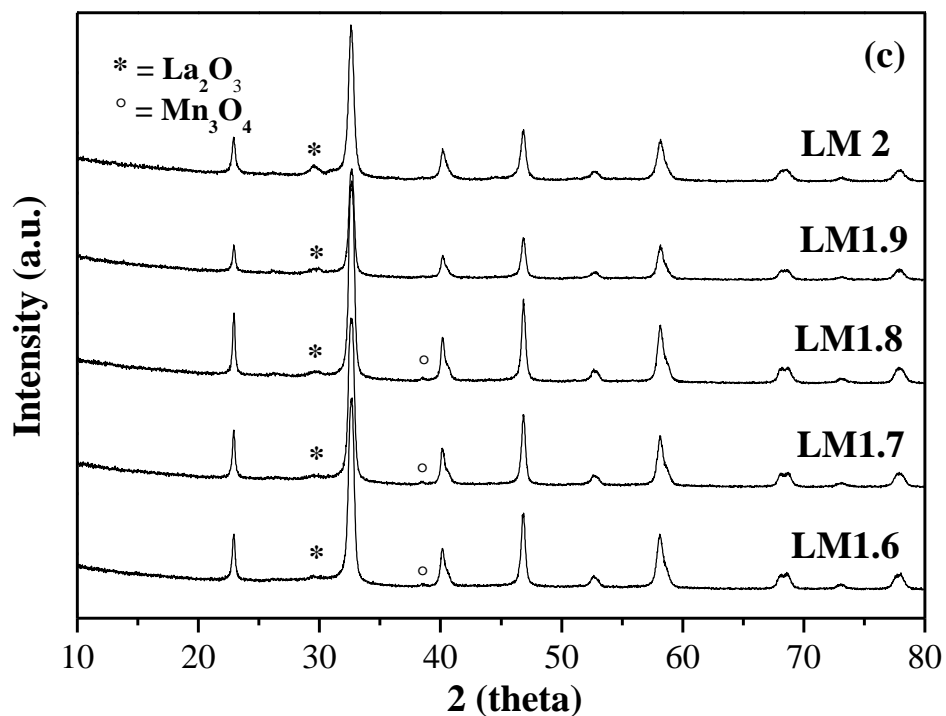


**Figure 4.1.** XRD patterns of LaMnO<sub>3</sub> samples, (a) low molar ratio of CA to total metal ions (La<sup>3+</sup> + Mn<sup>2+</sup>), (b) medium molar ratio and (c) high molar ratio.

**Table 4.1.** Physicochemical properties of the catalysts.

Samples	Calcination static	SSA <sup>1</sup> (m <sup>2</sup> g <sup>-1</sup> )	La/Mn molar ratio	d <sub>XRD</sub> <sup>2</sup> (nm)	H <sub>2</sub> -uptake (mmol g <sup>-1</sup> )			Reducibility <sup>3</sup> %
					250-500 °C	650-900 °C	Total	
LM 0.5	750 °C (2 h) in air	9	1.002	26				
LM 0.6	750 °C (2 h) in air	10	1.077	25				
LM 0.7	750 °C (2 h) in air	11	1.001	22				
LM 0.8	750 °C (2 h) in air	10	1.038	25	1.073	1.923	2.996	51.9
LM 0.9	750 °C (2 h) in air	11	1.062	21				
LM 1	750 °C (2 h) in air	12	1.015	23	1.156	1.883	3.039	55.9
LM 1.1	750 °C (2 h) in air	25	0.995	19				
LM 1.2	750 °C (2 h) in air	26	0.996	18	1.296	0.926	2.222	62.7

<b>LM 1.3</b>	750 °C (2 h) in air	25	1.019	18	1.297	1.175	2.472	62.7
<b>LM 1.4</b>	750 °C (2 h) in air	22	1.013	20				
<b>LM 1.5</b>	750 °C (2 h) in air	21	1.002	20	1.292	0.922	2.216	62.5
<b>LM 1.6</b>	750 °C (2 h) in air	13	1.034	23				
<b>LM 1.7</b>	750 °C (2 h) in air	12	1.047	22	1.066	1.367	2.433	51.6
<b>LM 1.8</b>	750 °C (2 h) in air	5	1.009	25				
<b>LM 1.9</b>	750 °C (2 h) in air	6	1.085	28				
<b>LM 2</b>	750 °C (2 h) in air	5	1.091	30				

<sup>1</sup>SSA: Specific surface area

<sup>2</sup>d<sub>XRD</sub> Crystallite size

<sup>3</sup>Reducibility (250-500°C) of Mn<sup>4+</sup>/Mn<sup>3+</sup> calculated as (experimental uptake mmol H<sub>2</sub>g<sup>-1</sup>/2.067 mmol H<sub>2</sub>g<sup>-1</sup>) x100

### 4.3. N<sub>2</sub> adsorption-desorption at -196 °C

The specific surface areas are summarized in Table 4.1. The relationship between the surface area and the molar ratio CA to total metal ions (La<sup>3+</sup> + Mn<sup>2+</sup>) is displayed in Figure 4.2. LM1.2 possess the largest specific surface area equal to 26 m<sup>2</sup> g<sup>-1</sup> and similar values were measured for LM 1.1 and LM 1.3. For molar ratio values between 0.5-1.0, the BET values were in the range 9-12 m<sup>2</sup> g<sup>-1</sup>, while by increasing the molar ratio values from 1.4 to 2.0, the surface area dramatically decreased from 22 to 5 m<sup>2</sup> g<sup>-1</sup>. It is likely that by increasing the concentration of CA, the increased heat of combustion of the LaMn(C<sub>6</sub>H<sub>5</sub>O<sub>7</sub>)(NO<sub>3</sub>)<sub>3</sub> intermediate species negatively affect the surface area and crystal size of the resulting LM perovskites (Taguchi, Matsu-ura, Nagao, Choso, & Tabata, 1997).

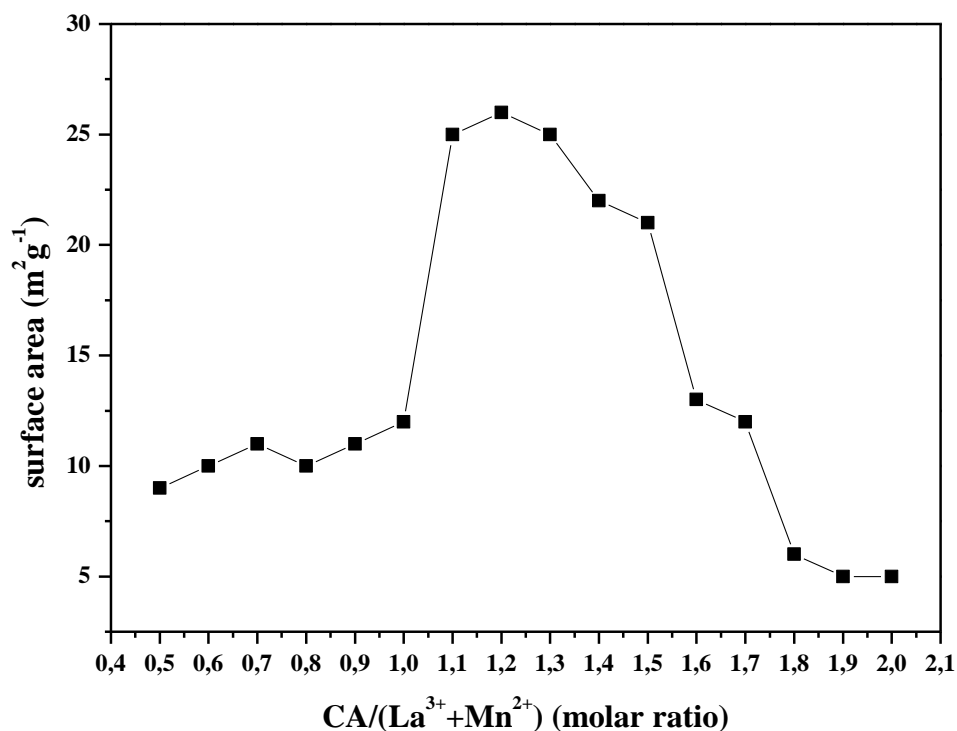


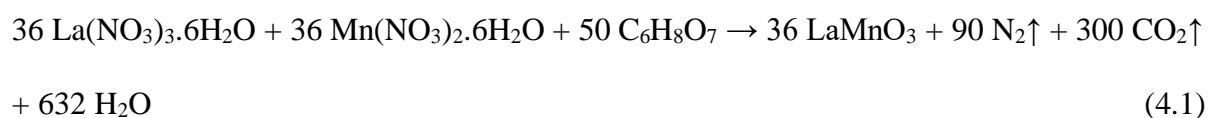
**Figure 4.2.** Relationship between the surface area of the catalysts and the molar ratio of CA to total metal ions (La<sup>3+</sup> + Mn<sup>2+</sup>).

#### 4.4. Thermogravimetric and differential thermal analysis

The thermal stability and crystallization temperature of the catalysts, in the form of dried gels, were studied by TGA/DTA analyses carried out, under air flow, in the range of temperature 25–900°C. In Figure. 4.3, the curves registered for selected samples prepared with low, medium and high CA to total metal ions (La<sup>3+</sup> + Mn<sup>2+</sup>) molar ratio, namely LM0.8, LM1.2 and LM2, are displayed and compared with pure CA. For all LM samples, a weight loss ≤ 10% was observed for between room temperature and ca. 130-155 °C, not detected for pure CA, likely due to residual adsorbed and hydrated water that may remain in the precursors. This step was followed by two major weight losses (up to ~ 50-60 % ) extending between ~200 and 600 °C in coincidence with observation of two exothermic peaks between 250-280 °C and at around

450-470 °C . According with the literature (Mali & Ataie, 2005) and in line with our previous results (Ghiasi et al., 2013), in such range of temperature, the exothermic reaction between citric acid and nitrates occurs. Moreover, between 400 and 600 °C the decomposition of both, carbonate species, such as lanthanum and/or manganese oxycarbonate along with of residual nitrate species, may occur producing the exothermic peaks at ~450 °C. Finally, above 600 °C there was slight mass decrease, which was ascribed to the formation of the final perovskite phase. The progressive decomposition of the LM gels, so far discussed, was correlated to the TGA/DTA curves of pure CA, analyzed as reference. In such case, the main weight loss occurs between ~200-280 °C (90%) with an endothermic peak at 220 °C, attributed to the decomposition of the citrate into carbonate and oxycarbonate (Hammami, Aïssa, & Batis, 2009). Total degradation takes place between 280-500 °C where residual carbonate species were decomposed (weight loss of 10%).

By comparing the TGA curves of the selected LM samples, it results that the overall weight loss registered at 900 °C increased as: LM0.8 < LM1.2 < LM2, in agreement with the increased CA to total metal ions (La<sup>3+</sup> + Mn<sup>2+</sup>) molar ratio used in the preparation. The reaction between citric acid and metal nitrates for LaMnO<sub>3</sub> synthesis is presented as Eq. (4.1):



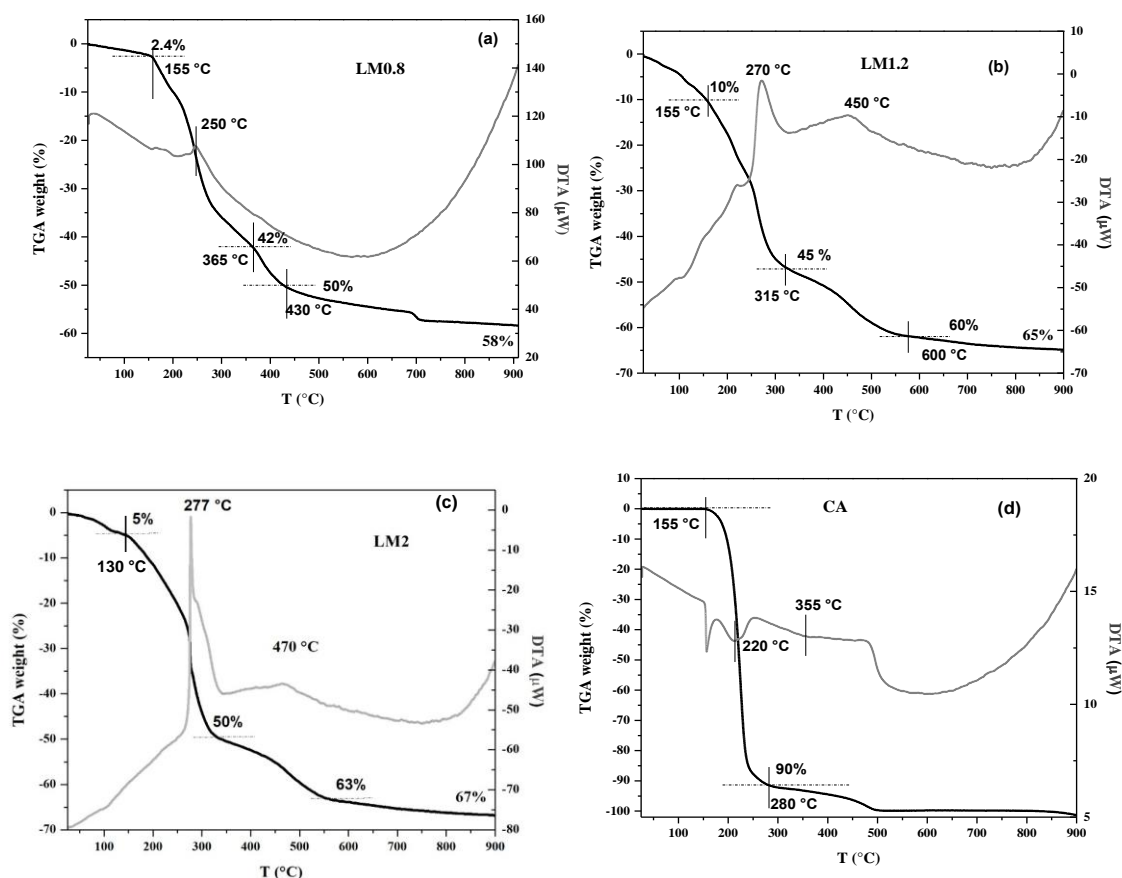


**Figure 4.3.** DTA and TGA profiles registered under air for selected non-calcined catalysts and for pure CA, used as reference.

#### 4.5. FT-IR.

FT-IR spectra of the dried gels and as synthesized powders in the range from 500 to 4000  $\text{cm}^{-1}$ . IR spectra of the dried gels and as-synthesized powders were examined to investigate the chemical and structural changes that took place during the combustion process. The dried gels (Figure 4.4) show several absorption band at about 820, 1032, 1280, 1415, 1580 and  $3350\text{cm}^{-1}$  (Predoana et al., 2007; Taguchi et al., 1997). FT-IR spectroscopic results in Table 4.2 .After calcination, the bands of  $\text{NO}_3^-$  and carboxylic group disappear and bands of the O–H reduce significantly (Figure 4.5). On the other hand, a significant spectroscopic band at about  $600\text{ cm}^{-1}$  appears corresponding to the stretching mode involving the internal motion of a

change in length of the Mn–O–Mn or Mn–O bond (Nagabhushana, Chakradhar, Ramesh, Shivakumara, & Chandrappa, 2007). The band at  $1465\text{ cm}^{-1}$  with a shoulder at  $1370\text{ cm}^{-1}$  can be assigned to the C–O stretching of unidentified carbonates resulting from the decomposition of the citrates. A small band at  $865\text{ cm}^{-1}$ , due to O–C–O bending in the carbonates, can also be observed (Berger et al., 2007). The disappearance of the characteristic bands of the carboxylic group and  $\text{NO}_3^-$  ions in the IR spectra of as-burnt powder suggests that carboxylic group and  $\text{NO}_3^-$  ions take part in the reaction during calcination.

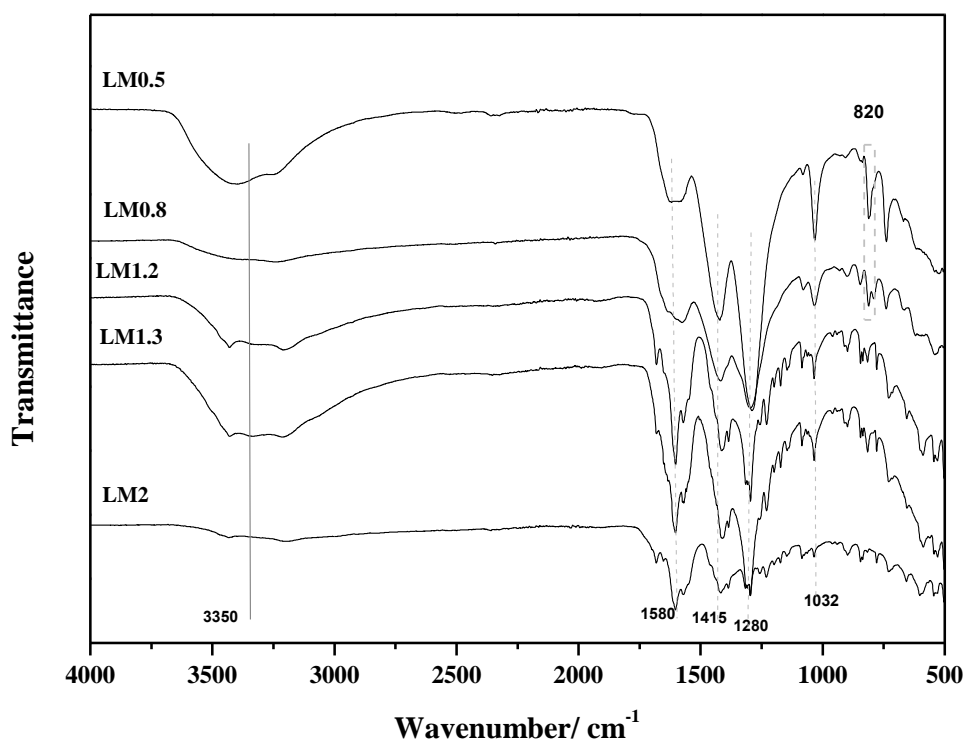


**Figure 4.4.** FTIR spectra of the gels with LM0.5, LM0.8, LM1, LM1.2 and LM2.

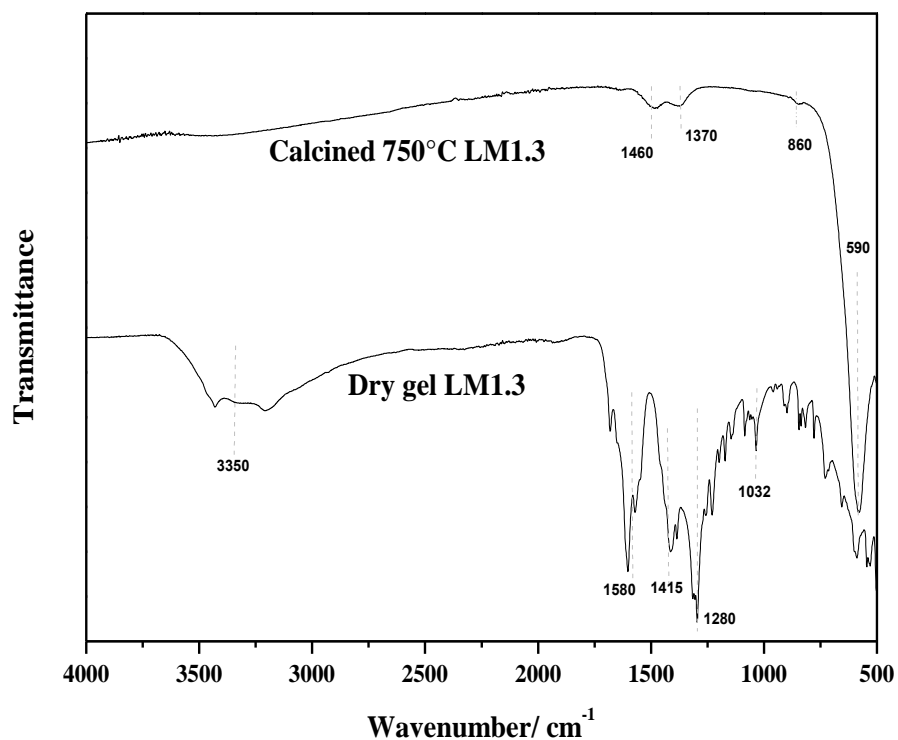


**Figure 4.5.** FT-IR spectra of the dried gel and synthesized powder for LM1.3.

From the results of thermal analysis and IR measurement, we determined the chemical composition of the gels. As for the gel with lower concentration of citric acid namely (LM0.5 and LM0.8) the gel is considered to be  $\text{LaMn}(\text{C}_6\text{H}_5\text{O}_7)(\text{NO}_3)_3$ , where the theoretical weight loss is  $\approx 57\%$ . As for the gel with higher concentration of citric acid LM1.2, LM1.3 and LM2 The disappearance of the peak  $\approx 820\text{ cm}^{-1}$  indicates that the gel is  $\text{LaMn}(\text{C}_6\text{H}_5\text{O}_7)_2$ .

**Table 4.2.** FT-IR spectroscopic results.

Dried gel wavenumber/cm <sup>-1</sup>	Calcined 750°C wavenumber/cm <sup>-1</sup>	Vibration mode	Assignments
–	≈600	Mn–O–Mn or Mn–O bond	
≈820	–	NO <sub>3</sub> <sup>–</sup> ions	
	≈860	O–C–O	
≈1032	–	ν C – OH	
≈1280	–	Ncooh	Introduced by the citric acid
≈1415	–	ν <sub>sym</sub> (COO)	Carbonyl symmetric stretching
–	≈1370 and ≈1465	C–O	Resulting from the decomposition of the citrates
≈1565-1580		ν <sub>asym</sub> (COO)	Carbonyl symmetric stretching
≈3350		νOH	Structural OH group

#### 4.6. H<sub>2</sub>-TPR.

In order to investigate the relative reducibility of the sample as a function of the CA to total metal ions (La<sup>3+</sup> + Mn<sup>2+</sup>) molar ratio, H<sub>2</sub>-TPR experiments were carried out over six selected catalysts characterized by low, medium and high molar ratio values, namely, LM0.8 and LM1, LM1.2 and LM1.3, LM1.5 and LM1.7. The respective surface area values ranged between 10-26 m<sup>2</sup>g<sup>-1</sup>. H<sub>2</sub>-TPR profiles are shown in Figure. 4.6 and the corresponding H<sub>2</sub> consumption of each reduction region is summarized in Table 4.1.



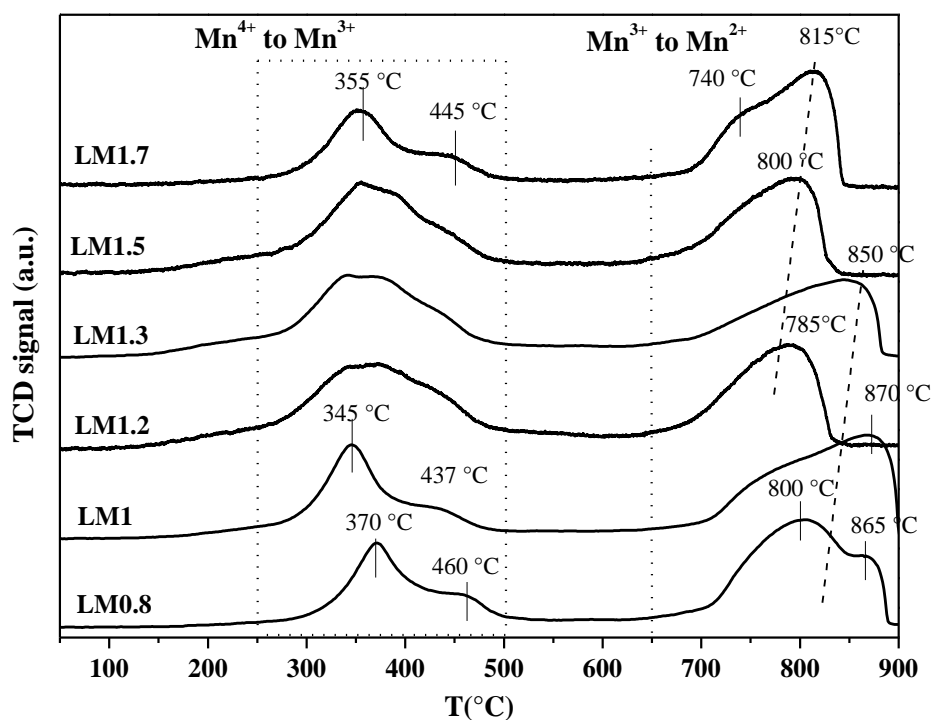


**Figure 4.6.** H<sub>2</sub>-TPR profiles of selected LaMnO<sub>3</sub> catalysts.

For all samples the overall profiles could be divided into two reduction regions, at low temperature between 250-500 °C and at high temperature, above 650 °C. According with previous results of our group (Ghiasi et al., 2013; Zhang et al., 2014b) the hydrogen consumption below 500 °C was ascribed to the reduction of Mn<sup>4+</sup> to Mn<sup>3+</sup> in the perovskite structure. It is worth noting that the shape and temperature of the reduction curves seem to depend on the CA to total metal ions (La<sup>3+</sup> + Mn<sup>2+</sup>) molar ratio of the samples and, therefore, on their textural properties. LM0.8, LM1 and LM1.7 characterized by surface area around 10-12 m<sup>2</sup>/g and crystal size around 22-25 nm, showed a main peak centered between 345 and 370 °C with a shoulder between 437 and 460 °C, while for samples with bigger surface area and relatively smaller crystallites, namely LM1.2, LM1.3 and LM1.5, the reduction of Mn<sup>4+</sup> to Mn<sup>3+</sup> occurs with a broad peak suggesting the presence of less crystalline domains. As reported in Table 4.1, the H<sub>2</sub> uptake between 250-500 °C was ranging between ~ 1.0 and 1.3 mmol H<sub>2</sub> g<sup>-1</sup> that corresponded to reducibility values of Mn<sup>4+</sup> to Mn<sup>3+</sup> between ~ 52-63%.

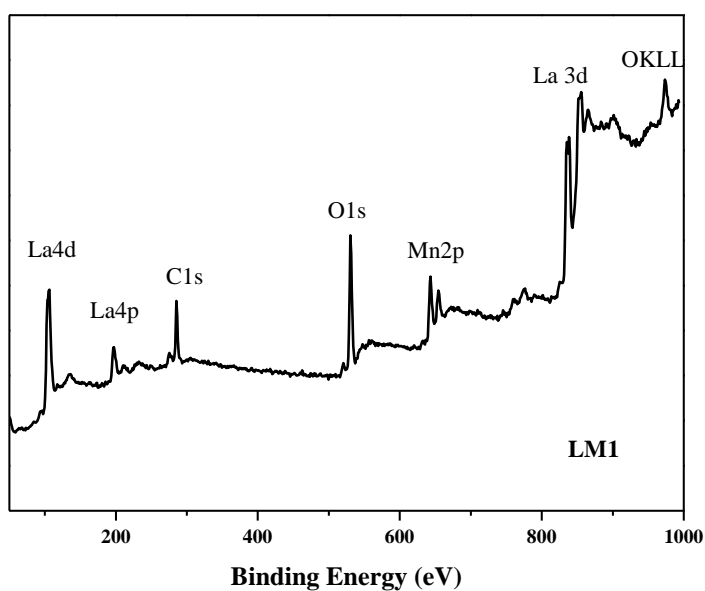
By increasing the temperature above 650 °C a great and broad hydrogen consumption was detected which shape and temperature varied as a function of the samples. Such hydrogen consumption was assigned to the reduction of  $\text{Mn}^{3+}$  into  $\text{Mn}^{2+}$  that occurs in one or two successive steps likely up to some destruction of the perovskite structure. The  $\text{H}_2$  uptake ranging between  $\sim 0.9$  and  $1.9 \text{ mmol H}_2 \text{ g}^{-1}$ , as a function of the sample, correlated with the partial reduction of  $\text{Mn}^{3+}$  into  $\text{Mn}^{2+}$ . On the other hand, based on the total  $\text{H}_2$  consumption, listed in Table 4.1, and considering that 1g of sample contains 4.13 mmol of Mn it is confirmed that  $\text{Mn}^{4+}$  species are present in the perovskite structure.

#### 4.7. X-ray photoelectron spectroscopy (XPS)

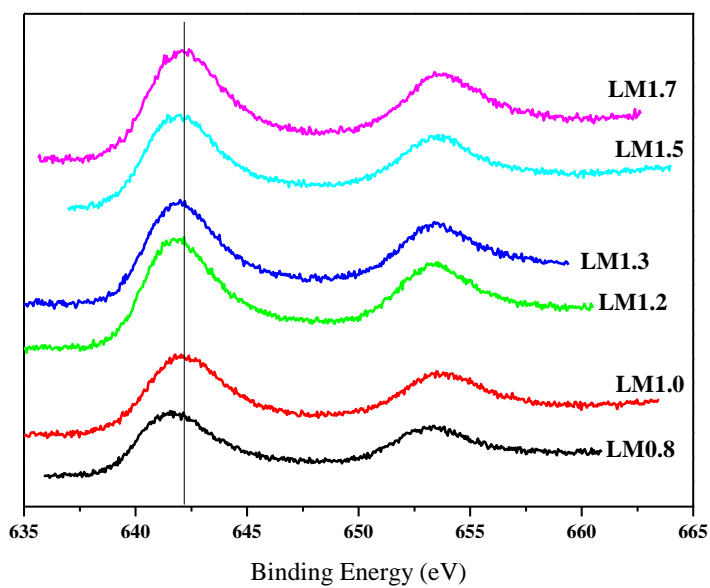
XPS analyses were performed to study the surface composition and oxidation state of selected LM catalysts. A typical XP survey spectrum recorded for the sample LM1 is shown in Figure 4.7.  $\text{La}3d_{5/2}$  binding energy, is 834.0 eV typical of perovskites materials. In Table 4.3 the BE of O1s and Mn2p are listed. In Figure 4.6 the experimental Mn2p XP spectra are displayed for the LM catalysts. Position shapes and spin-orbit separation of main peaks are among the experimental error the same (see Table 4.3 and Figure 4.8). The BE values of  $\text{Mn}2p_{3/2}$  were close enough to those obtained for  $\text{Mn}_2\text{O}_3$  at 641.9 eV. Anyway, the presence of the  $\text{Mn}^{4+}$  ions could not be excluded because of the proximity of its peak to the  $\text{Mn}^{3+}$  ion's one (642.2 eV) (Hammami et al., 2009). The constant BE of the  $\text{La}3d_{5/2}$  and  $\text{Mn}2p_{3/2}$  levels suggest, in accord with the results reported by Taguchi et al. (Taguchi, Sugita, Nagao, & Tabata, 1995), that the chemical bonding for  $\text{LaMnO}_3$  was not affected by different synthetic procedures. Conversely, there are small differences in the Mn/La atomic ratio as a function of the CA/Mn+La nitrates molar ratio. The Mn surface concentration slightly increases by increasing the CA concentration, the highest value being observed for LM1.5, then Mn again decreased (see Figure 4.9). The highest surface concentration of Mn detected for the samples LM1.2, LM1.3 and LM 1.5 somehow correlates with the catalytic trend in toluene conversion.

**Table 4.3.** BE of O1s and Mn2p of selected LM oxides and Mn/La atomic ratio.

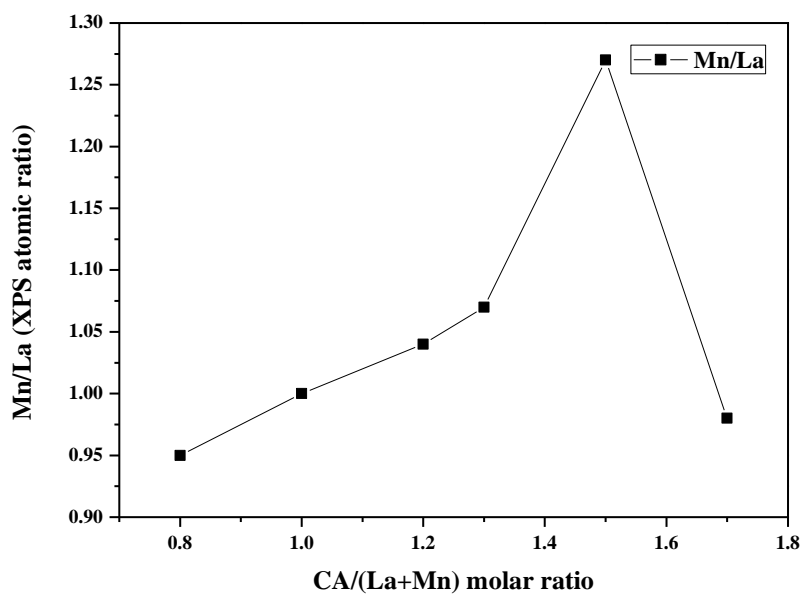
Samples	O1s (eV)	Mn2p 3/2 (eV) $\Delta$ is the spin orbit separation)	Mn/La
<b>LM0.8</b>	529.3 (59%) 531.6 (41%)	641.6 $\Delta=11.6$	0.95
<b>LM1.0</b>	529.6 (70%) 531.9 (30%)	642.1 $\Delta=11.5$	1.00
<b>LM1.2</b>	529.3 (52%) 531.6 (48%)	641.9 $\Delta=11.5$	1.04
<b>LM1.3</b>	529.4 (47%) 531.7 (53%)	641.9 $\Delta=11.5$	1.07
<b>LM1.5</b>	529.5 (66%) 531.7 (34%)	641.9 $\Delta=11.5$	1.27
<b>LM1.7</b>	529.3 (60%) 531.6 (40%)	642.1 $\Delta=11.5$	0.98



**Figure 4.7:** XP survey spectrum recorded for the sample LM1.



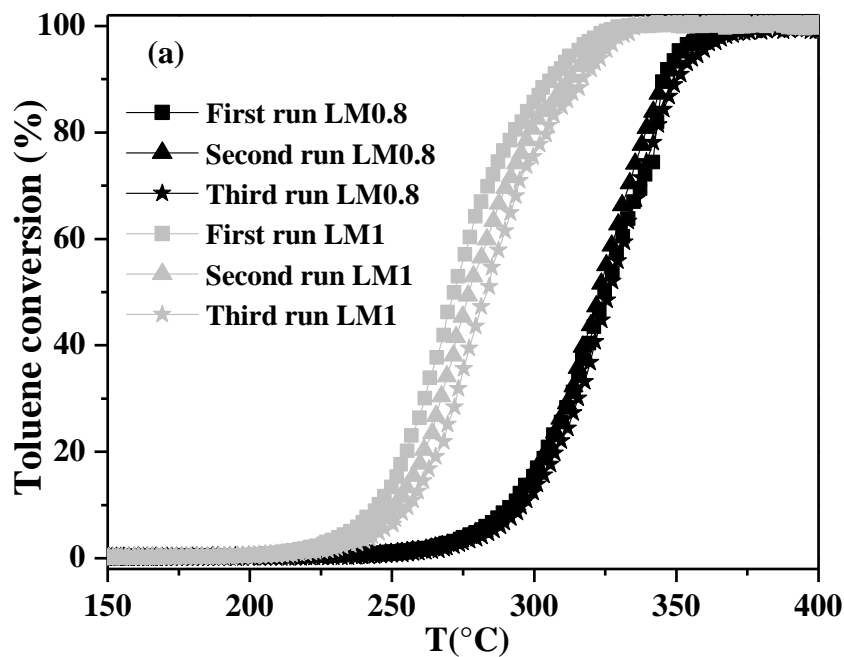
**Figure 4.8.** Experimental Mn2p XP spectra for selected LM samples.



**Figure 4.9.** Relationship between the Mn/La surface atomic ratio and the molar ratio of CA to total metal ions ( $\text{La}^{3+} + \text{Mn}^{2+}$ ) for selected LM catalysts.

#### 4.8. Catalytic performances in the catalytic oxidation of toluene.

Catalytic activity measurements were performed as light-off experiments. The catalysts stability was further assessed upon consecutive light-off runs. In details, the catalyst stability was firstly evaluated by performing three consecutive catalytic runs for each catalyst. The conversion-temperature profiles (light-off curves) obtained upon three consecutive cycles, during the cooling ramp, are shown in Fig. 4.10, where selected catalysts are compared, as follows: (a) LM0.8 and LM1, (b) LM1.2 and LM1.3 and (c) LM1.5 and LM1.7. The temperatures at 10, 50 and 90% of toluene conversion,  $T_{10}$ ,  $T_{50}$  and  $T_{90}$ , respectively, were used to compare the catalytic activities of the samples and are summarized Table 4.4.



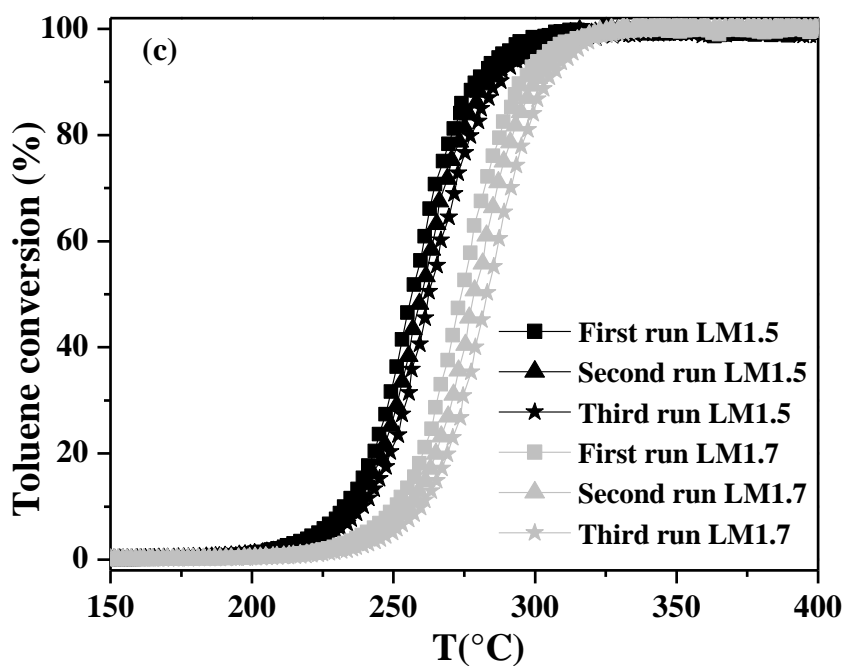
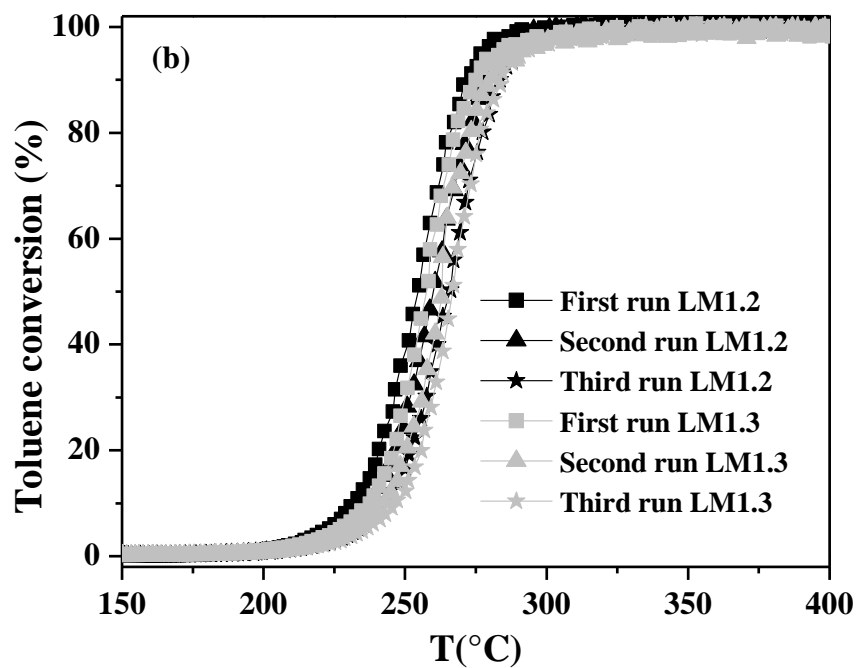


**Figure 4.10.** Evolution of the toluene conversion as a function of temperature, while cooling the reactor, upon three consecutive runs (a) LM0.8 and LM1, (b) LM1.2 and LM1.3 and (c) LM1.5 and LM1.7.

As it results from an inspection of Figure 4.10, the conversion of toluene monotonously increased with an increase in the reaction temperature, and a complete conversion of toluene

could be successfully achieved below 350°C over all samples. When the conversion reached 100%, only CO<sub>2</sub> and H<sub>2</sub>O were observed as oxidation products of toluene. Based on the conversion temperatures (see Table 4.4) and as it can be seen from Figure 4.11 where the toluene conversion achieved during the second run was compared and catalysts was compared with that of typical industrial catalysts such as a commercial Pd/Al<sub>2</sub>O<sub>3</sub> catalyst containing 1 % Pd, the prepared catalysts ranked as follows: LM1.5 ~LM1.2 ~LM1.3 > LM1~LM1.7 >> LM0.8.

The three best performing catalysts exhibited the highest specific surface area, around 21-26 m<sup>2</sup>/g, the optimum reducibility at low temperature and surface Mn/La atomic ratio higher than the stoichiometric value, 1.0, suggesting some Mn enrichment on the surface.

**Table 4.4.** Catalytic performances of the catalysts in terms of temperatures for achieving 10, 50 and 90% of toluene conversion. Data were collected upon cooling.

Catalysts	1st Run			2nd Run			3rd Run		
	T <sub>10</sub> °C	T <sub>50</sub> °C	T <sub>90</sub> °C	T <sub>10</sub> °C	T <sub>50</sub> °C	T <sub>90</sub> °C	T <sub>10</sub> °C	T <sub>50</sub> °C	T <sub>90</sub> °C
<b>LM0.8</b>	294	325	345	294	324	346	296	325	351
<b>LM1</b>	245	272	305	251	277	313	255	281	317
<b>LM1.2</b>	233	255	272	237	260	279	243	266	284
<b>LM1.3</b>	238	258	275	243	263	281	247	267	284
<b>LM1.5</b>	233	257	279	237	259	283	239	263	288
<b>LM1.7</b>	251	275	294	255	279	301	260	283	305

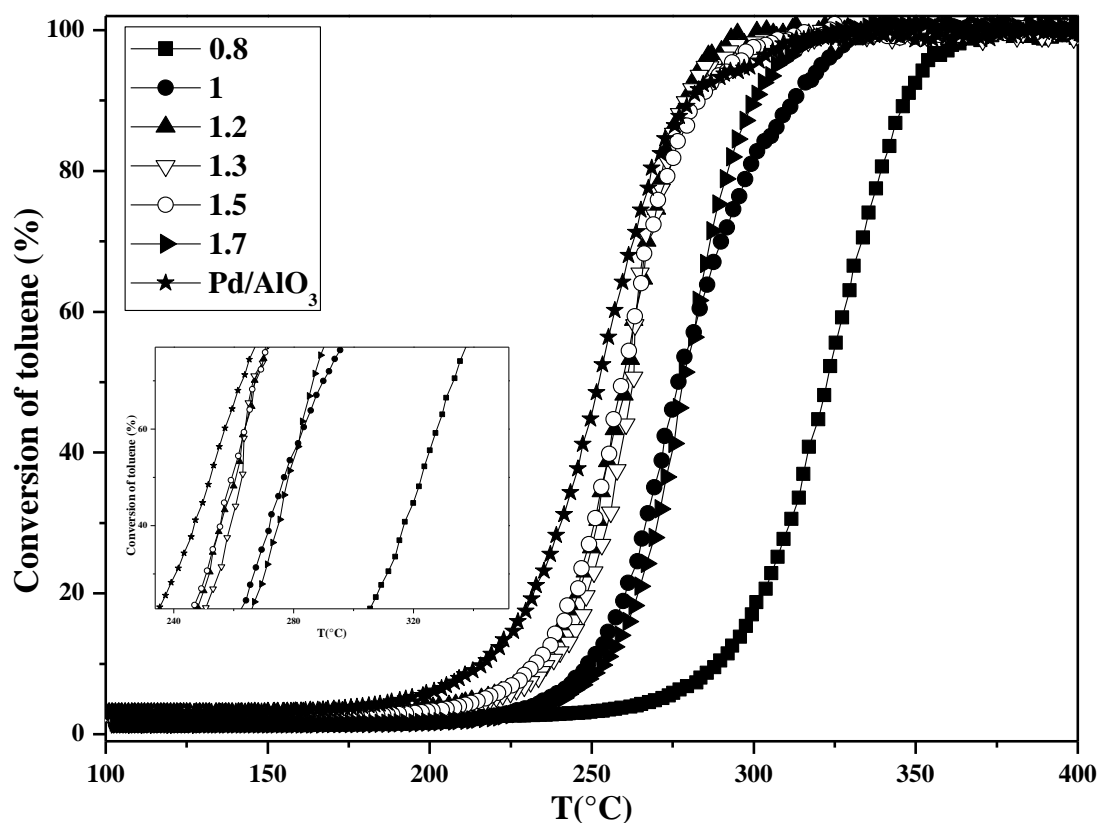


**Figure 4.11.** Toluene conversion versus temperature during the second consecutive run (cooling ramp). In the inset, the range of temperature at which conversion values between 40-80% were achieved is displayed.

The catalytic stability of the catalysts was further assessed under steady-state conditions at ~17% of toluene conversion for 24 h. Figure 4.12 shows the evolution of the conversion with the time on stream. Conversion values between 17 % and ~13 % were observed during the entire reaction time, confirming in the overall stable catalytic performance. In details, a slight deactivation was observed during the first 4 h of reaction for all catalysts, after that LM1.3 exhibited very good catalytic stability and durability in the following 20 h (around 16% of toluene conversion), LM 0.8 and LM 1.2 deactivated some more up to around 13% of conversion, conversion values over LM1.5, LM1 and LM1.7 showing an intermediate behavior.



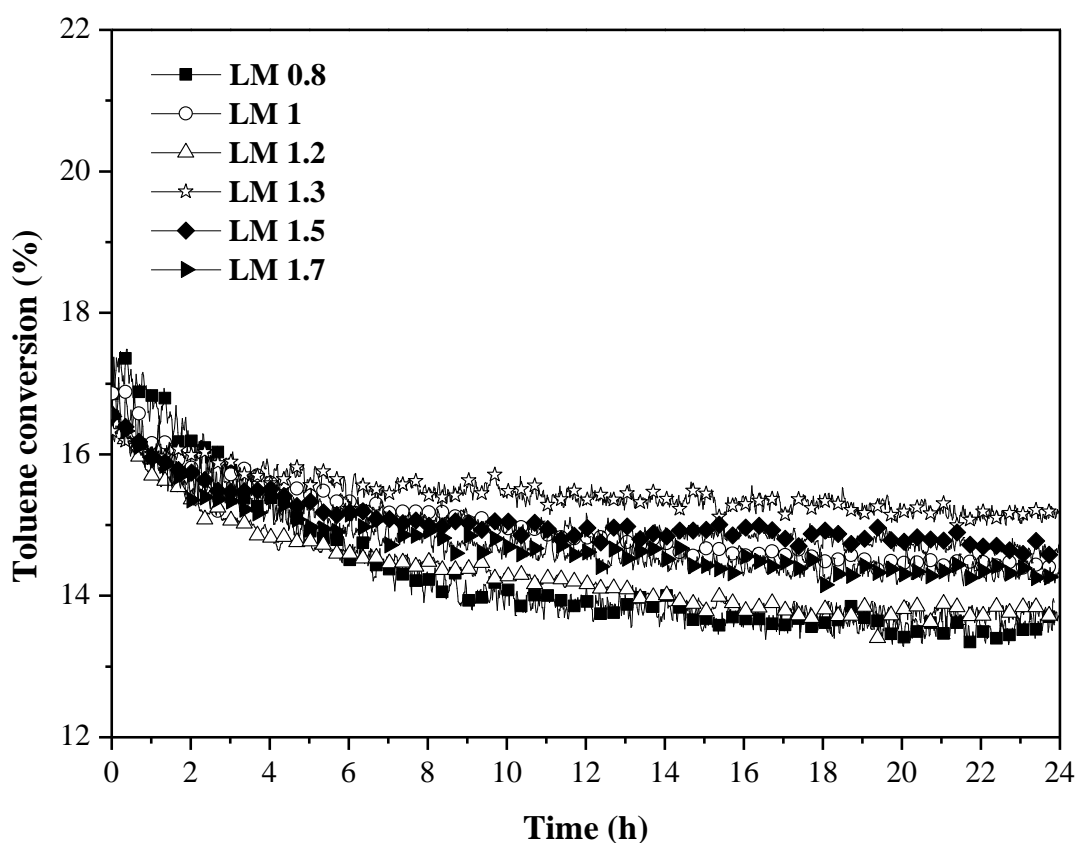


**Figure 4.12.** Lifetime toluene oxidation test performed at ~17 % of toluene conversion during 24 h.

#### 4.9. Conclusions.

The  $\text{LaMnO}_3$  perovskite prepared by citrate sol-gel method with different ratios of citric acid affected of the surface area and the catalytic activity of toluene oxidation. The catalytic stability was confirmed for all catalysts during three consecutive runs and long-term experiments. The results showed that the best catalytic performances were registered for the samples LM 1.2, LM 1.3 and LM 1.5 in agreement with the higher surface area, better reducibility at low temperature, below 500 °C, and higher surface concentration of Mn detected for such samples.

## Chapter 5

### General conclusions

This work aimed at the preparation of catalytically active manganese based oxides for VOCs abatement. Results reported in Chapter 3 showed that four different catalysts based on manganese oxide (LaMnO<sub>3</sub>, OMS and Mn<sub>2</sub>O<sub>3</sub>) were prepared using several preparation routes. For the synthesis of OMS two different preparation routes, solid state (OMSs) and hydrothermal method, were employed. The OMSs catalyst, prepared via solid-state method, exhibited the highest catalytic activity for the complete oxidation of toluene at low temperature, which could be related to its higher reducibility were more reducible at low temperatures compared to other catalysts but also to higher specific surface area 95 (m<sup>2</sup>g<sup>-1</sup>). The catalytic performances of the catalysts followed the order: OMSs > OMSh > Mn<sub>2</sub>O<sub>3</sub> > LaMnO<sub>3</sub>. In all cases the reaction started at around 200–250 °C with full conversion of toluene being achieved below 350°C. This trend was in agreement with the evolution of the specific surface area. Also, the loading (wt%) of the active element of the catalysts (Mn) followed a similar trend as the catalytic activities, except for Mn<sub>2</sub>O<sub>3</sub>, which is the one with the highest loading of Mn but its surface area is lower than half of the surface area of the catalyst with the highest catalytic activity (OMSs). All catalysts demonstrated to be stable upon three consecutive runs. A comparison between the present results with the performances of different Mn-containing catalysts, already reported in the literature, show comparable activity with our systems, OMSs being the most active one. Tests of toluene oxidation over a reference Pd/Al<sub>2</sub>O<sub>3</sub> catalyst were also performed for comparison purposes. Although for such Pd catalyst a T<sub>50</sub> value slightly lower than the one of OMSs was found, the OMSs was more active at low temperature. A kinetic study was carried out and a model was developed with an excellent good agreement between the experimental and predicted data even at high temperatures. For all catalysts, the reaction is the only rate-limiting step. At the end of Chapter 3, it was demonstrated that, although LaMnO<sub>3</sub> was the worse catalyst in the evolution of the toluene conversion as a function of temperature, in the range 100-400 °C, it exhibited relatively good catalytic stability and durability under steady-

state conditions at 25% of toluene conversion as a function of time on stream (24 h). For that reasons, it is worth investigating the effects of the preparation method and the experimental conditions on the physicochemical properties and the catalytic performances of LaMnO<sub>3</sub> perovskite. With the purpose to study the effect of the citric acid (CA) concentration on the catalytic properties of the LaMnO<sub>3</sub> perovskites, samples with a CA to (La<sup>3+</sup> + Mn<sup>2+</sup>) ions molar ratio ranging from 0.5 to 2 were prepared and investigated in the chapter 4 of the thesis.






It was demonstrated that the crystalline phase purity of the LaMnO<sub>3</sub> perovskite depends on the CA concentration, indeed, at high concentration of CA, namely for molar ratio in the range 1.6-2.0, a small peak, attributed to La<sub>2</sub>O<sub>3</sub> phase, appeared. The highest amount of La<sub>2</sub>O<sub>3</sub> impurity was detected at CA to total metal ions (La<sup>3+</sup> + Mn<sup>2+</sup>) molar ratio equal to 2.0. The presence of very small features, ascribed to the phase Mn<sub>3</sub>O<sub>4</sub> was also observed for samples of the series LM1.6-LM2, while, the phase purity of LaMnO<sub>3</sub> perovskite was higher for CA molar ratio values in the range 0.5-1.5. Concerning the catalytic performances in the oxidation of toluene, the catalysts LM1.2, LM1.3 and LM1.5 showed the best catalytic performances in the range of temperature, 150-400 °C, LM0.8 was poor performing, while LM1 and LM1.7 exhibited an intermediate behavior. Under steady-state conditions at ~17% of toluene conversion for 24 h, LM1.3 exhibited the best catalytic activity and durability (stable values of toluene conversion, around 16%, were registered).

In conclusions, the catalysts studied in the present work compare well with typical industrial systems, such as Pd over alumina, and are worthy of further investigation in more realistic conditions. Considering that industrial effluents are mixtures of several VOC gases, the study of the catalytic activities of these materials on the double or ternary-VOC systems would be important for future applications.

## Chapter 6

## Appendix

## 1. Chemical products used in this work


Chemical Product	Label elements	Pictogram
<b>Manganese acetate</b> (Mn (CH <sub>3</sub> COO) <sub>2</sub> .4H <sub>2</sub> O)	Causes skin irritation. Causes serious eye irritation.	
<b>Manganese(II) Sulfate Monohydrate</b> (MnSO <sub>4</sub> .H <sub>2</sub> O)	May cause damage to organs through prolonged or repeated exposure. Toxic to aquatic life with long lasting effects.	
<b>Manganese(II) nitrate tetrahydrate</b> (Mn(NO <sub>3</sub> ) <sub>2</sub> .4H <sub>2</sub> O)	May intensify fire; oxidizer. Harmful if swallowed Causes severe skin burns and eye damage. May cause damage to organs (Brain) through prolonged or repeated exposure if inhaled. Harmful to aquatic life with long lasting effects	
<b>Potassium Permanganate</b> (KMnO <sub>4</sub> )	May intensify fire; oxidiser. Harmful if swallowed. Very toxic to aquatic life with long lasting effects.	
<b>Lanthanum(III) nitrate hydrate</b> (La(NO <sub>3</sub> ) <sub>3</sub> .6H <sub>2</sub> O)	May intensify fire; oxidizer. Causes skin irritation. Causes serious eye irritation. May cause respiratory irritation.	

## 2. Publications

1. Sihaib, Z., Puleo, F., Garcia-Vargas, J. M., Retailleau, L., Descorme, C., Liotta, L. F., ... & Giroir-Fendler, A. (2017). Manganese oxide-based catalysts for toluene oxidation. *Applied Catalysis B: Environmental*, 209, 689-700

Applied Catalysis B: Environmental 209 (2017) 689–700


---



Contents lists available at [ScienceDirect](#)

### Applied Catalysis B: Environmental


journal homepage: [www.elsevier.com/locate/apcatb](http://www.elsevier.com/locate/apcatb)



---

## Manganese oxide-based catalysts for toluene oxidation

Z. Sihaib<sup>a,b</sup>, F. Puleo<sup>b</sup>, J.M. Garcia-Vargas<sup>a</sup>, L. Retailleau<sup>a</sup>, C. Descorme<sup>a</sup>, L.F. Liotta<sup>b</sup>, J.L. Valverde<sup>c</sup>, S. Gil<sup>a,\*</sup>, A. Giroir-Fendler<sup>a,\*</sup>



<sup>a</sup> Univ Lyon, Université Claude Bernard Lyon 1, CNRS, IRCELYON, 2 avenue Albert Einstein, Villeurbanne F-69622, France  
<sup>b</sup> Istituto per lo Studio dei Materiali Nanostrutturati (ISMN)-CNR, via Ugo La Malfa, 153, 90146 Palermo, Italy  
<sup>c</sup> Facultad de Ciencias y Tecnologías Químicas, Departamento de Ingeniería Química, Universidad de Castilla-La Mancha, 13071 Ciudad Real, Spain

---

#### ARTICLE INFO

**Article history:**  
Received 14 January 2017  
Received in revised form 11 March 2017  
Accepted 15 March 2017  
Available online 19 March 2017

**Keywords:**  
Perovskite  
OMS  
Manganese Oxide  
Oxidation  
Toluene

#### ABSTRACT

Four different catalysts based on manganese oxide were prepared: a perovskite (LaMnO<sub>3</sub>), via sol-gel method; Mn<sub>2</sub>O<sub>3</sub>, rapid method and an Octahedral Molecular Sieve (OMS-2) by two different preparation methods, via solid state (OMS<sub>s</sub>) and hydrothermal method (OMS<sub>h</sub>). The physicochemical properties of these catalysts were characterized by X-ray diffraction (XRD), N<sub>2</sub> adsorption–desorption at –196 °C, thermogravimetric and differential thermal analysis (TGA/DTA), inductively coupled plasma optical emission spectroscopy (ICP-OES) and temperature-programmed reduction with hydrogen (H<sub>2</sub>-TPR). Their catalytic performances were evaluated in the catalytic oxidation of toluene. Three consecutive catalytic cycles were performed for each catalyst in order to reach steady state performances. In order to assess the stability of the catalysts under reaction conditions, the catalytic performances were studied upon long term experiments running for 24 h at 25% of toluene conversion. For comparison purposes, the catalytic activity of the present manganese oxide catalysts was compared with that of typical industrial catalysts such as a commercial Pd/Al<sub>2</sub>O<sub>3</sub> catalyst containing 0.78% Pd. The crystalline features detected in the XRD patterns, are well-consistent with the formation of the desired structures. Based on their specific surface area and their low-temperature reducibility, the catalysts were ranked as follows: OMS<sub>s</sub> > Mn<sub>2</sub>O<sub>3</sub> > OMS<sub>h</sub> > LaMnO<sub>3</sub>. This trend was in good agreement with the performances observed in the catalytic removal of toluene. A kinetic model was proposed and a good agreement was obtained upon fitting with the experimental data.

© 2017 Elsevier B.V. All rights reserved.

2. Z. Sihaib, F. Puleo, C. Descorme, L.F. Liotta, J.L. Valverde, S. Gil, A. Giroir-Fendler. The effect of citric acid ratio on LaMnO<sub>3</sub> properties (2018) under preparation.

## References



## References

- Aguero, Fabiola N., Scian, Alberto, Barbero, Bibiana P., & Cadús, Luis E. (2008). Influence of the Support Treatment on the Behavior of MnOx/Al<sub>2</sub>O<sub>3</sub> Catalysts used in VOC Combustion. *Catalysis Letters*, 128(3), 268. doi: 10.1007/s10562-008-9695-y
- Andersen, Ib, Lundqvist, Gunnar R., Ihave, Lars, Pedersen, Ole Find, Proctor, Donald F., . . . Wyon, David P. (1983). Human response to controlled levels of toluene in six-hour exposures. *Scandinavian Journal of Work, Environment & Health*, 9(5), 405-418.
- Arai, H., Yamada, T., Eguchi, K., & Seiyama, T. (1986). Catalytic combustion of methane over various perovskite-type oxides. *Applied Catalysis*, 26(Supplement C), 265-276. doi: [https://doi.org/10.1016/S0166-9834\(00\)82556-7](https://doi.org/10.1016/S0166-9834(00)82556-7)
- Avgouropoulos, George, Oikonomopoulos, Evaggelos, Kanistras, Dimitrios, & Ioannides, Theophilos. (2006). Complete oxidation of ethanol over alkali-promoted Pt/Al<sub>2</sub>O<sub>3</sub> catalysts. *Applied Catalysis B: Environmental*, 65(1), 62-69. doi: <https://doi.org/10.1016/j.apcatb.2005.12.016>
- Bælum, Jesper, Lundqvist, Gunnar R., Mølhav, Lars, & Andersen, Niels Trolle. (1990). Human response to varying concentrations of toluene. *International Archives of Occupational and Environmental Health*, 62(1), 65. doi: 10.1007/bf00397850
- Baldi, Marco, Escribano, Vicente Sanchez, Amores, José Manuel Gallardo, Milella, Fabio, & Busca, Guido. (1998). Characterization of manganese and iron oxides as combustion catalysts for propane and propene. *Applied Catalysis B: Environmental*, 17(3), L175-L182. doi: [https://doi.org/10.1016/S0926-3373\(98\)00013-7](https://doi.org/10.1016/S0926-3373(98)00013-7)
- Baldi, Marco, Finocchio, Elisabetta, Milella, Fabio, & Busca, Guido. (1998). Catalytic combustion of C<sub>3</sub> hydrocarbons and oxygenates over Mn<sub>3</sub>O<sub>4</sub>. *Applied Catalysis B: Environmental*, 16(1), 43-51. doi: [https://doi.org/10.1016/S0926-3373\(97\)00061-1](https://doi.org/10.1016/S0926-3373(97)00061-1)
- Barakat, Tarek, Rooke, Joanna C., Franco, Manuel, Cousin, Renaud, Lamonier, Jean-François, Giraudon, Jean-Marc, . . . Siffert, Stéphane. (2012). Pd- and/or Au-Loaded Nb- and V-Doped Macro-Mesoporous TiO<sub>2</sub> Supports as Catalysts for the Total Oxidation of VOCs. *European Journal of Inorganic Chemistry*, 2012(16), 2812-2818. doi: 10.1002/ejic.201101233
- Barbour, A.K., Burdett, N.A., Cairns, J., Derwent, R., Chave, P.A., Crutzen, P., . . . Hopke, P.K. (2007). *Volatile Organic Compounds in the Atmosphere*: Royal Society of Chemistry.
- Bastos, S. S. T., Carabineiro, S. A. C., Órfão, J. J. M., Pereira, M. F. R., Delgado, J. J., & Figueiredo, J. L. (2012). Total oxidation of ethyl acetate, ethanol and toluene catalyzed by exotemplated manganese and cerium oxides loaded with gold. *Catalysis Today*, 180(1), 148-154. doi: <https://doi.org/10.1016/j.cattod.2011.01.049>
- Bastos, S. S. T., Órfão, J. J. M., Freitas, M. M. A., Pereira, M. F. R., & Figueiredo, J. L. (2009). Manganese oxide catalysts synthesized by exotemplating for the total oxidation of ethanol. *Applied Catalysis B: Environmental*, 93(1), 30-37. doi: <https://doi.org/10.1016/j.apcatb.2009.09.009>
- Bedia, J., Rosas, J. M., Rodríguez-Mirasol, J., & Cordero, T. (2010). Pd supported on mesoporous activated carbons with high oxidation resistance as catalysts for toluene oxidation. *Applied Catalysis B: Environmental*, 94(1), 8-18. doi: <https://doi.org/10.1016/j.apcatb.2009.10.015>
- Behar, Siham, Gómez-Mendoza, Noel-Andrés, Gómez-García, Miguel-Ángel, Świerczyński, Dariusz, Quignard, Françoise, & Tanchoux, Nathalie. (2015). Study and modelling of kinetics of the oxidation of VOC catalyzed by nanosized Cu–Mn spinels prepared via an alginate route. *Applied Catalysis A: General*, 504(Supplement C), 203-210. doi: <https://doi.org/10.1016/j.apcata.2014.12.021>

- Berger, D., Matei, C., Papa, F., Macovei, D., Fruth, V., & Deloume, J. P. (2007). Pure and doped lanthanum manganites obtained by combustion method. *Journal of the European Ceramic Society*, 27(13), 4395-4398. doi: <https://doi.org/10.1016/j.jeurceramsoc.2007.02.164>
- Brock, Stephanie L., Duan, Niangao, Tian, Zheng Rong, Giraldo, Oscar, Zhou, Hua, & Suib, Steven L. (1998). A Review of Porous Manganese Oxide Materials. *Chemistry of Materials*, 10(10), 2619-2628. doi: 10.1021/cm980227h
- Brunauer, Stephen, Emmett, P. H., & Teller, Edward. (1938). Adsorption of Gases in Multimolecular Layers. *Journal of the American Chemical Society*, 60(2), 309-319. doi: 10.1021/ja01269a023
- Cai, Jun, Liu, Jia, Willis, William S., & Suib, Steven L. (2001). Framework Doping of Iron in Tunnel Structure Cryptomelane. *Chemistry of Materials*, 13(7), 2413-2422. doi: 10.1021/cm0014233
- Cant, Noel W., Angove, Dennys E., & J. Patterson, Michael. (1998). The effects of residual chlorine on the behaviour of platinum group metals for oxidation of different hydrocarbons. *Catalysis Today*, 44(1), 93-99. doi: [https://doi.org/10.1016/S0920-5861\(98\)00177-1](https://doi.org/10.1016/S0920-5861(98)00177-1)
- Cant, Noel W., & Hall, W. Keith. (1970). Catalytic oxidation: II. Silica supported noble metals for the oxidation of ethylene and propylene. *Journal of Catalysis*, 16(2), 220-231. doi: [https://doi.org/10.1016/0021-9517\(70\)90216-2](https://doi.org/10.1016/0021-9517(70)90216-2)
- Carabineiro, S. A. C., Chen, X., Konsolakis, M., Psarras, A. C., Tavares, P. B., Órfão, J. J. M., . . . Figueiredo, J. L. (2015). Catalytic oxidation of toluene on Ce-Co and La-Co mixed oxides synthesized by exotemplating and evaporation methods. *Catalysis Today*, 244, 161-171. doi: <https://doi.org/10.1016/j.cattod.2014.06.018>
- Carabineiro, S. A. C., Chen, X., Martynyuk, O., Bogdanchikova, N., Avalos-Borja, M., Pestryakov, A., . . . Figueiredo, J. L. (2015). Gold supported on metal oxides for volatile organic compounds total oxidation. *Catalysis Today*, 244(Supplement C), 103-114. doi: <https://doi.org/10.1016/j.cattod.2014.06.034>
- Carballo, Luis M., & Wolf, Eduardo E. (1978). Crystallite size effects during the catalytic oxidation of propylene on  $\gamma$ -Al<sub>2</sub>O<sub>3</sub>. *Journal of Catalysis*, 53(3), 366-373. doi: [https://doi.org/10.1016/0021-9517\(78\)90108-2](https://doi.org/10.1016/0021-9517(78)90108-2)
- Castaño, María Haidy, Molina, Rafael, & Moreno, Sonia. (2015). Catalytic oxidation of VOCs on MnMgAlO<sub>x</sub> mixed oxides obtained by auto-combustion. *Journal of Molecular Catalysis A: Chemical*, 398(Supplement C), 358-367. doi: <https://doi.org/10.1016/j.molcata.2015.01.001>
- Chen, Min, Qi, Lingyan, Fan, Liping, Zhou, Renxian, & Zheng, Xiaoming. (2008). Zirconium-pillared montmorillonite and their application in supported palladium catalysts for volatile organic compounds purification. *Materials Letters*, 62(21), 3646-3648. doi: <https://doi.org/10.1016/j.matlet.2008.04.017>
- Chen, X., Carabineiro, S. A. C., Bastos, S. S. T., Tavares, P. B., Órfão, J. J. M., Pereira, M. F. R., & Figueiredo, J. L. (2014). Catalytic oxidation of ethyl acetate on cerium-containing mixed oxides. *Applied Catalysis A: General*, 472(Supplement C), 101-112. doi: <https://doi.org/10.1016/j.apcata.2013.11.043>
- Chen, X., Carabineiro, S. A. C., Tavares, P. B., Órfão, J. J. M., Pereira, M. F. R., & Figueiredo, J. L. (2014). Catalytic oxidation of ethyl acetate over La-Co and La-Cu oxides. *Journal of Environmental Chemical Engineering*, 2(1), 344-355. doi: <https://doi.org/10.1016/j.jece.2014.01.003>
- Chen, Xiao, Shen, Yan-Fei, Suib, Steven L., & O'Young, C. L. (2001). Catalytic Decomposition of 2-Propanol over Different Metal-Cation-Doped OMS-2 Materials. *Journal of Catalysis*, 197(2), 292-302. doi: <https://doi.org/10.1006/jcat.2000.3063>

- Chen, Xiao, Shen, Yan-Fei, Suib, Steven L., & O'Young, C. L. (2002). Characterization of Manganese Oxide Octahedral Molecular Sieve (M-OMS-2) Materials with Different Metal Cation Dopants. *Chemistry of Materials*, 14(2), 940-948. doi: 10.1021/cm000868o
- Chlala, D., Giraudon, J. M., Nuns, N., Lancelot, C., Vannier, Rose-Noëlle, Labaki, M., & Lamonier, J. F. (2016). Active Mn species well dispersed on Ca<sup>2+</sup> enriched apatite for total oxidation of toluene. *Applied Catalysis B: Environmental*, 184(Supplement C), 87-95. doi: <https://doi.org/10.1016/j.apcatb.2015.11.020>
- Ciuparu, Dragos, Lyubovsky, Maxim R., Altman, Eric, Pfefferle, Lisa D., & Datye, Abhaya. (2002). CATALYTIC COMBUSTION OF METHANE OVER PALLADIUM-BASED CATALYSTS. *Catalysis Reviews*, 44(4), 593-649. doi: 10.1081/CR-120015482
- CUI, XIAO-LING, LI, YONG-LI, LI, SHI-YOU, SUN, GUO-CUN, MA, JIN-XIA, ZHANG, LU, . . . MA, RONG-BO. (2014). Mn<sub>3</sub>O<sub>4</sub> nano-sized crystals: Rapid synthesis and extension to preparation of nanosized LiMn<sub>2</sub>O<sub>4</sub> materials. *Journal of Chemical Sciences*, 126(3), 561-567. doi: 10.1007/s12039-014-0592-1
- Day, A. K. Cheetham and P. (1992). Solid State Chemistry: Compounds (pp. 234). Oxford science publications.
- de la Osa, A. R., De Lucas, A., Romero, A., Valverde, J. L., & Sánchez, P. (2011). Kinetic models discrimination for the high pressure WGS reaction over a commercial CoMo catalyst. *International Journal of Hydrogen Energy*, 36(16), 9673-9684. doi: <https://doi.org/10.1016/j.ijhydene.2011.05.043>
- de Rivas, Beatriz, López-Fonseca, Rubén, Jiménez-González, Cristina, & Gutiérrez-Ortiz, José I. (2011). Synthesis, characterisation and catalytic performance of nanocrystalline Co<sub>3</sub>O<sub>4</sub> for gas-phase chlorinated VOC abatement. *Journal of Catalysis*, 281(1), 88-97. doi: <https://doi.org/10.1016/j.jcat.2011.04.005>
- DeGuzman, Roberto N., Shen, Yan-Fei, Neth, Edward J., Suib, Steven L., O'Young, Chi-Lin, Levine, Steven, & Newsam, John M. (1994). Synthesis and Characterization of Octahedral Molecular Sieves (OMS-2) Having the Hollandite Structure. *Chemistry of Materials*, 6(6), 815-821. doi: 10.1021/cm00042a019
- Delimaris, Dimitrios, & Ioannides, Theophilos. (2008). VOC oxidation over MnO<sub>x</sub>-CeO<sub>2</sub> catalysts prepared by a combustion method. *Applied Catalysis B: Environmental*, 84(1), 303-312. doi: <https://doi.org/10.1016/j.apcatb.2008.04.006>
- Ding, Yun-shuang, Shen, Xiong-fei, Sithambaram, Shanthakumar, Gomez, Sinue, Kumar, Ranjit, Crisostomo, Vincent Mark B., . . . Aindow, Mark. (2005). Synthesis and Catalytic Activity of Cryptomelane-Type Manganese Dioxide Nanomaterials Produced by a Novel Solvent-Free Method. *Chemistry of Materials*, 17(21), 5382-5389. doi: 10.1021/cm051294w
- Domínguez, M. I., Navarro, P., Romero-Sarria, F., Frías, D., Cruz, S. A., Delgado, J. J., . . . Odriozola, J. A. (2009). Fibrous MnO<sub>2</sub> Nanoparticles with (2 × 2) Tunnel Structures. Catalytic Activity in the Total Oxidation of Volatile Organic Compounds. *Journal of Nanoscience and Nanotechnology*, 9(6), 3837-3842. doi: 10.1166/jnn.2009.NS76
- Doornkamp, C., & Ponec, V. (2000). The universal character of the Mars and Van Krevelen mechanism. *Journal of Molecular Catalysis A: Chemical*, 162(1), 19-32. doi: [https://doi.org/10.1016/S1381-1169\(00\)00319-8](https://doi.org/10.1016/S1381-1169(00)00319-8)
- Duplančić, Marina, Tomašić, Vesna, & Gomzi, Zoran. (2017). Catalytic oxidation of toluene: comparative study over powder and monolithic manganese-nickel mixed oxide catalysts. *Environmental Technology*, 1-13. doi: 10.1080/09593330.2017.1346713
- Duprat, Françoise. (2002). Light-off curve of catalytic reaction and kinetics. *Chemical Engineering Science*, 57(6), 901-911. doi: [https://doi.org/10.1016/S0009-2509\(01\)00409-2](https://doi.org/10.1016/S0009-2509(01)00409-2)

- Einaga, Hisahiro, Yamamoto, Shintaro, Maeda, Nanako, & Teraoka, Yasutake. (2015). Structural analysis of manganese oxides supported on SiO<sub>2</sub> for benzene oxidation with ozone. *Catalysis Today*, 242(Part B), 287-293. doi: <https://doi.org/10.1016/j.cattod.2014.05.018>
- . European Union emission inventory report 1990–2014 under the UNESCO Convention on Long-range Transponder Air Pollution (LYRA). (2016) *European Environment Agency*.
- Everaert, K., & Baeyens, J. (2004). Catalytic combustion of volatile organic compounds. *Journal of Hazardous Materials*, 109(1), 113-139. doi: <https://doi.org/10.1016/j.jhazmat.2004.03.019>
- Feng, Qi, Kanoh, Hirofumi, & Ooi, Kenta. (1999). Manganese oxide porous crystals. *Journal of Materials Chemistry*, 9(2), 319-333. doi: 10.1039/A805369C
- Finocchio, Elisabetta, & Busca, Guido. (2001). Characterization and hydrocarbon oxidation activity of coprecipitated mixed oxides Mn<sub>3</sub>O<sub>4</sub>/Al<sub>2</sub>O<sub>3</sub>. *Catalysis Today*, 70(1), 213-225. doi: [https://doi.org/10.1016/S0920-5861\(01\)00419-9](https://doi.org/10.1016/S0920-5861(01)00419-9)
- Galvita, Vladimir V., Filez, Matthias, Poelman, Hilde, Bliznuk, Vitaliy, & Marin, Guy B. (2014). The Role of Different Types of CuO in CuO–CeO<sub>2</sub>/Al<sub>2</sub>O<sub>3</sub> for Total Oxidation. *Catalysis Letters*, 144(1), 32-43. doi: 10.1007/s10562-013-1144-x
- Gandhe, Aditi R., Rebello, Jeanette S., Figueiredo, J. L., & Fernandes, J. B. (2007). Manganese oxide OMS-2 as an effective catalyst for total oxidation of ethyl acetate. *Applied Catalysis B: Environmental*, 72(1), 129-135. doi: <https://doi.org/10.1016/j.apcatb.2006.10.017>
- Garcia, Tomas, Agouram, Said, Sánchez-Royo, Juan F., Murillo, Ramón, Mastral, Ana María, Aranda, Asunción, . . . Solsona, Benjamin. (2010). Deep oxidation of volatile organic compounds using ordered cobalt oxides prepared by a nanocasting route. *Applied Catalysis A: General*, 386(1), 16-27. doi: <https://doi.org/10.1016/j.apcata.2010.07.018>
- Garcia, Tomas, Solsona, Benjamin, & Taylor, Stuart H. (2004). The Oxidative Destruction of Hydrocarbon Volatile Organic Compounds Using Palladium–Vanadia–Titania Catalysts. *Catalysis Letters*, 97(1), 99-103. doi: 10.1023/B:CATL.0000034294.35776.db
- Gélin, Patrick, & Primet, Michel. (2002). Complete oxidation of methane at low temperature over noble metal based catalysts: a review. *Applied Catalysis B: Environmental*, 39(1), 1-37. doi: [https://doi.org/10.1016/S0926-3373\(02\)00076-0](https://doi.org/10.1016/S0926-3373(02)00076-0)
- Genuino, Homer C., Dharmarathna, Saminda, Njagi, Eric C., Mei, Michael C., & Suib, Steven L. (2012). Gas-Phase Total Oxidation of Benzene, Toluene, Ethylbenzene, and Xylenes Using Shape-Selective Manganese Oxide and Copper Manganese Oxide Catalysts. *The Journal of Physical Chemistry C*, 116(22), 12066-12078. doi: 10.1021/jp301342f
- Ghiasi, Elham, Malekzadeh, Azim, & Ghiasi, Mahnaz. (2013). Moderate concentration of citric acid for the formation of LaMnO<sub>3</sub> and LaCoO<sub>3</sub> nano-perovskites. *Journal of Rare Earths*, 31(10), 997-1002. doi: [https://doi.org/10.1016/S1002-0721\(13\)60020-4](https://doi.org/10.1016/S1002-0721(13)60020-4)
- Gil, A., Gandía, L. M., & Korili, S. A. (2004). Effect of the temperature of calcination on the catalytic performance of manganese- and samarium-manganese-based oxides in the complete oxidation of acetone. *Applied Catalysis A: General*, 274(1), 229-235. doi: <https://doi.org/10.1016/j.apcata.2004.07.004>
- Gil, Sonia, Marchena, Miriam, Sánchez-Silva, Luz, Romero, Amaya, Sánchez, Paula, & Valverde, José Luís. (2011). Effect of the operation conditions on the selective oxidation of glycerol with catalysts based on Au supported on carbonaceous materials. *Chemical Engineering Journal*, 178(Supplement C), 423-435. doi: <https://doi.org/10.1016/j.cej.2011.10.048>

- Giroir-Fendler, Anne, Alves-Fortunato, Maira, Richard, Melissandre, Wang, Chao, Díaz, Jose Antonio, Gil, Sonia, . . . Guo, Yanglong. (2016). Synthesis of oxide supported LaMnO<sub>3</sub> perovskites to enhance yields in toluene combustion. *Applied Catalysis B: Environmental*, 180(Supplement C), 29-37. doi: <https://doi.org/10.1016/j.apcatb.2015.06.005>
- Hammami, Ramzi, Aïssa, Salwa Ben, & Batis, Habib. (2009). Effects of thermal treatment on physico-chemical and catalytic properties of lanthanum manganite LaMnO<sub>3+y</sub>. *Applied Catalysis A: General*, 353(2), 145-153. doi: <https://doi.org/10.1016/j.apcata.2008.10.048>
- Han, Wen, Deng, Jiguang, Xie, Shaohua, Yang, Huanggen, Dai, Hongxing, & Au, Chak Tong. (2014). Gold Supported on Iron Oxide Nanodisk as Efficient Catalyst for The Removal of Toluene. *Industrial & Engineering Chemistry Research*, 53(9), 3486-3494. doi: 10.1021/ie5000505
- Heinsohn, R.J., & Kabel, R.L. (1998). *Sources and control of air pollution: Engineering principles*: American Academy of Environmental Engineers, Annapolis, MD (United States).
- Hermia, J., & Vigneron, S. (1993). Catalytic incineration for odour abatement and VOC destruction. *Catalysis Today*, 17(1), 349-358. doi: [https://doi.org/10.1016/0920-5861\(93\)80038-3](https://doi.org/10.1016/0920-5861(93)80038-3)
- Hosseini, Mahsa, Siffert, Stephane, Cousin, Renaud, Aboukaïs, Antoine, Hadj-Sadok, Zoulika, & Su, Bao-Lian. (2009). Total oxidation of VOCs on Pd and/or Au supported on TiO<sub>2</sub>/ZrO<sub>2</sub> followed by “operando” DRIFT. *Comptes Rendus Chimie*, 12(6), 654-659. doi: <https://doi.org/10.1016/j.crci.2008.09.032>
- Hu, Chaoquan. (2011). Catalytic combustion kinetics of acetone and toluene over Cu<sub>0.13</sub>Ce<sub>0.87</sub>O<sub>y</sub> catalyst. *Chemical Engineering Journal*, 168(3), 1185-1192. doi: <https://doi.org/10.1016/j.cej.2011.02.006>
- Hu, Rongrong, Cheng, Yi, Xie, Lanying, & Wang, Dezheng. (2007). Effect of Doped Ag on Performance of Manganese Oxide Octahedral Molecular Sieve for CO Oxidation. *Chinese Journal of Catalysis*, 28(5), 463-468. doi: [https://doi.org/10.1016/S1872-2067\(07\)60040-0](https://doi.org/10.1016/S1872-2067(07)60040-0)
- Huang, Hui, Meng, Yongtao, Labonte, Alec, Doble, Arthur, & Suib, Steven L. (2013). Large-Scale Synthesis of Silver Manganese Oxide Nanofibers and Their Oxygen Reduction Properties. *The Journal of Physical Chemistry C*, 117(48), 25352-25359. doi: 10.1021/jp409507h
- Huang, Yi-Chin, Luo, Chin-Hsiang, Yang, Shinhao, Lin, Yi-Chang, & Chuang, Chi-Yu. (2010). Improved Removal of Indoor Volatile Organic Compounds by Activated Carbon Fiber Filters Calcined with Copper Oxide Catalyst. *CLEAN – Soil, Air, Water*, 38(11), 993-997. doi: 10.1002/clen.200900302
- Iablokov, Viacheslav, Frey, Krisztina, Geszti, Olga, & Kruse, Norbert. (2010). High Catalytic Activity in CO Oxidation over MnO<sub>x</sub> Nanocrystals. *Catalysis Letters*, 134(3), 210-216. doi: 10.1007/s10562-009-0244-0
- Joung, Hea-Jung, Kim, Jae-Ha, Oh, Jun-Sik, You, Dong-Wook, Park, Han-Oh, & Jung, Kwang-Woo. (2014). Catalytic oxidation of VOCs over CNT-supported platinum nanoparticles. *Applied Surface Science*, 290(Supplement C), 267-273. doi: <https://doi.org/10.1016/j.apsusc.2013.11.066>
- Kang, Min, Park, Eun Duck, Kim, Ji Man, & Yie, Jae Eui. (2007). Manganese oxide catalysts for NO<sub>x</sub> reduction with NH<sub>3</sub> at low temperatures. *Applied Catalysis A: General*, 327(2), 261-269. doi: <https://doi.org/10.1016/j.apcata.2007.05.024>
- Karuppiah, J., Linga Reddy, E., Manoj Kumar Reddy, P., Ramaraju, B., Karvembu, R., & Subrahmanyam, Ch. (2012). Abatement of mixture of volatile organic compounds

- (VOCs) in a catalytic non-thermal plasma reactor. *Journal of Hazardous Materials*, 237(Supplement C), 283-289. doi: <https://doi.org/10.1016/j.jhazmat.2012.08.040>
- Khan, Faisal I., & Kr. Ghoshal, Alope. (2000). Removal of Volatile Organic Compounds from polluted air. *Journal of Loss Prevention in the Process Industries*, 13(6), 527-545. doi: [https://doi.org/10.1016/S0950-4230\(00\)00007-3](https://doi.org/10.1016/S0950-4230(00)00007-3)
- Kim, Sang Chai. (2002). The catalytic oxidation of aromatic hydrocarbons over supported metal oxide. *Journal of Hazardous Materials*, 91(1), 285-299. doi: [https://doi.org/10.1016/S0304-3894\(01\)00396-X](https://doi.org/10.1016/S0304-3894(01)00396-X)
- Kim, Sang Chai, & Shim, Wang Geun. (2010). Catalytic combustion of VOCs over a series of manganese oxide catalysts. *Applied Catalysis B: Environmental*, 98(3), 180-185. doi: <https://doi.org/10.1016/j.apcatb.2010.05.027>
- Kujawa, Joanna, Cerneaux, Sophie, & Kujawski, Wojciech. (2015). Removal of hazardous volatile organic compounds from water by vacuum pervaporation with hydrophobic ceramic membranes. *Journal of Membrane Science*, 474(Supplement C), 11-19. doi: <https://doi.org/10.1016/j.memsci.2014.08.054>
- Lahousse, C., Bernier, A., Grange, P., Delmon, B., Papaefthimiou, P., Ioannides, T., & Verykios, X. (1998). Evaluation of  $\gamma$ -MnO<sub>2</sub> as a VOC Removal Catalyst: Comparison with a Noble Metal Catalyst. *Journal of Catalysis*, 178(1), 214-225. doi: <https://doi.org/10.1006/jcat.1998.2148>
- Lakshmanan, Pandian, Delannoy, Laurent, Richard, Vincent, Méthivier, Christophe, Potvin, Claude, & Louis, Catherine. (2010). Total oxidation of propene over Au/xCeO<sub>2</sub>-Al<sub>2</sub>O<sub>3</sub> catalysts: Influence of the CeO<sub>2</sub> loading and the activation treatment. *Applied Catalysis B: Environmental*, 96(1), 117-125. doi: <https://doi.org/10.1016/j.apcatb.2010.02.009>
- Larcher, D., Sudant, G., Patrice, R., & Tarascon, J. M. (2003). Some Insights on the Use of Polyols-Based Metal Alkoxides Powders as Precursors for Tailored Metal-Oxides Particles. *Chemistry of Materials*, 15(18), 3543-3551. doi: 10.1021/cm030048m
- Larsson, Per-Olof, Andersson, Arne, Wallenberg, L. Reine, & Svensson, Bo. (1996). Combustion of CO and Toluene; Characterisation of Copper Oxide Supported on Titania and Activity Comparisons with Supported Cobalt, Iron, and Manganese Oxide. *Journal of Catalysis*, 163(2), 279-293. doi: <https://doi.org/10.1006/jcat.1996.0329>
- Leson, Gero, & Winer, Arthur M. (1991). Biofiltration: An Innovative Air Pollution Control Technology For VOC Emissions. *Journal of the Air & Waste Management Association*, 41(8), 1045-1054. doi: 10.1080/10473289.1991.10466898
- Li, W. B., Wang, J. X., & Gong, H. (2009). Catalytic combustion of VOCs on non-noble metal catalysts. *Catalysis Today*, 148(1-2), 81-87. doi: <http://dx.doi.org/10.1016/j.cattod.2009.03.007>
- Liotta, L. F. (2010). Catalytic oxidation of volatile organic compounds on supported noble metals. *Applied Catalysis B: Environmental*, 100(3), 403-412. doi: <https://doi.org/10.1016/j.apcatb.2010.08.023>
- Liu, Jia, Makwana, Vinit, Cai, Jun, Suib, Steven L., & Aindow, Mark. (2003). Effects of Alkali Metal and Ammonium Cation Templates on Nanofibrous Cryptomelane-type Manganese Oxide Octahedral Molecular Sieves (OMS-2). *The Journal of Physical Chemistry B*, 107(35), 9185-9194. doi: 10.1021/jp0300593
- Liu, Jia, Son, Young-Chan, Cai, Jun, Shen, Xiongfei, Suib, Steven L., & Aindow, Mark. (2004). Size Control, Metal Substitution, and Catalytic Application of Cryptomelane Nanomaterials Prepared Using Cross-linking Reagents. *Chemistry of Materials*, 16(2), 276-285. doi: 10.1021/cm0303989
- Liu, Peng, He, Hongping, Wei, Gaoling, Liu, Dong, Liang, Xiaoliang, Chen, Tianhu, . . . Zhu, Runliang. (2017). An efficient catalyst of manganese supported on diatomite for toluene oxidation: Manganese species, catalytic performance, and structure-activity

- relationship. *Microporous and Mesoporous Materials*, 239(Supplement C), 101-110. doi: <https://doi.org/10.1016/j.micromeso.2016.09.053>
- Liu, Yuxi, Dai, Hongxing, Deng, Jiguang, Xie, Shaohua, Yang, Huanggen, Tan, Wei, . . . Guo, Guangsheng. (2014). Mesoporous Co<sub>3</sub>O<sub>4</sub>-supported gold nanocatalysts: Highly active for the oxidation of carbon monoxide, benzene, toluene, and o-xylene. *Journal of Catalysis*, 309(Supplement C), 408-418. doi: <https://doi.org/10.1016/j.jcat.2013.10.019>
- Liu, Yuxi, Dai, Hongxing, Deng, Jiguang, Zhang, Lei, Zhao, Zhenxuan, Li, Xinwei, . . . Guo, Guangsheng. (2013). Controlled Generation of Uniform Spherical LaMnO<sub>3</sub>, LaCoO<sub>3</sub>, Mn<sub>2</sub>O<sub>3</sub>, and Co<sub>3</sub>O<sub>4</sub> Nanoparticles and Their High Catalytic Performance for Carbon Monoxide and Toluene Oxidation. *Inorganic Chemistry*, 52(15), 8665-8676. doi: 10.1021/ic400832h
- Liu, Yuxi, Dai, Hongxing, Du, Yucheng, Deng, Jiguang, Zhang, Lei, & Zhao, Zhenxuan. (2012). Lysine-aided PMMA-templating preparation and high performance of three-dimensionally ordered macroporous LaMnO<sub>3</sub> with mesoporous walls for the catalytic combustion of toluene. *Applied Catalysis B: Environmental*, 119(Supplement C), 20-31. doi: <https://doi.org/10.1016/j.apcatb.2012.02.010>
- Luo, Jian, Zhang, Qiuhua, Garcia-Martinez, Javier, & Suib, Steven L. (2008). Adsorptive and Acidic Properties, Reversible Lattice Oxygen Evolution, and Catalytic Mechanism of Cryptomelane-Type Manganese Oxides as Oxidation Catalysts. *Journal of the American Chemical Society*, 130(10), 3198-3207. doi: 10.1021/ja077706e
- Luo, Jian, Zhang, Qiuhua, Huang, Aimin, & Suib, Steven L. (2000). Total oxidation of volatile organic compounds with hydrophobic cryptomelane-type octahedral molecular sieves. *Microporous and Mesoporous Materials*, 35(Supplement C), 209-217. doi: [https://doi.org/10.1016/S1387-1811\(99\)00221-8](https://doi.org/10.1016/S1387-1811(99)00221-8)
- Mali, A., & Ataie, A. (2005). Structural characterization of nano-crystalline BaFe<sub>12</sub>O<sub>19</sub> powders synthesized by sol-gel combustion route. *Scripta Materialia*, 53(9), 1065-1070. doi: <https://doi.org/10.1016/j.scriptamat.2005.06.037>
- Marquardt, Donald W. (1963). An Algorithm for Least-Squares Estimation of Nonlinear Parameters. *Journal of the Society for Industrial and Applied Mathematics*, 11(2), 431-441. doi: 10.1137/0111030
- Masui, Toshiyuki, Imadzu, Hayato, Matsuyama, Naoto, & Imanaka, Nobuhito. (2010). Total oxidation of toluene on Pt/CeO<sub>2</sub>-ZrO<sub>2</sub>-Bi<sub>2</sub>O<sub>3</sub>/γ-Al<sub>2</sub>O<sub>3</sub> catalysts prepared in the presence of polyvinyl pyrrolidone. *Journal of Hazardous Materials*, 176(1), 1106-1109. doi: <https://doi.org/10.1016/j.jhazmat.2009.11.108>
- Mellan, Thomas A., Maenetja, Khomotso P., Ngoepe, Phuti E., Woodley, Scott M., Catlow, C. Richard A., & Grau-Crespo, Ricardo. (2013). Lithium and oxygen adsorption at the [small beta]-MnO<sub>2</sub> (110) surface. *Journal of Materials Chemistry A*, 1(47), 14879-14887. doi: 10.1039/C3TA13559D
- Monks, P. S., Granier, C., Fuzzi, S., Stohl, A., Williams, M. L., Akimoto, H., . . . von Glasow, R. (2009). Atmospheric composition change – global and regional air quality. *Atmospheric Environment*, 43(33), 5268-5350. doi: <https://doi.org/10.1016/j.atmosenv.2009.08.021>
- Morales, Maria Roxana, Agüero, Fabiola N., & Cadus, Luis E. (2013). Catalytic Combustion of n-Hexane Over Alumina Supported Mn-Cu-Ce Catalysts. *Catalysis Letters*, 143(10), 1003-1011. doi: 10.1007/s10562-013-1083-6
- Moretti, E. C. (2002). Reduce VOC and HAP emissions. *Chemical Engineering Progress*, 98(6), 30-40.
- Musialik-Piotrowska, Anna. (2007). Destruction of trichloroethylene (TCE) and trichloromethane (TCM) in the presence of selected VOCs over Pt-Pd-based catalyst. *Catalysis Today*, 119(1), 301-304. doi: <https://doi.org/10.1016/j.cattod.2006.08.059>

- Nagabhushana, B. M., Chakradhar, R. P. Sreekanth, Ramesh, K. P., Shivakumara, C., & Chandrappa, G. T. (2007). Combustion synthesis, characterization and metal–insulator transition studies of nanocrystalline  $\text{La}_{1-x}\text{Ca}_x\text{MnO}_3$  ( $0.0 \leq x \leq 0.5$ ). *Materials Chemistry and Physics*, *102*(1), 47-52. doi: <https://doi.org/10.1016/j.matchemphys.2006.11.002>
- Najjar, Hend, Lamonier, Jean-François, Mentré, Olivier, Giraudon, Jean-Marc, & Batis, Habib. (2011). Optimization of the combustion synthesis towards efficient  $\text{LaMnO}_3$ +y catalysts in methane oxidation. *Applied Catalysis B: Environmental*, *106*(1), 149-159. doi: <https://doi.org/10.1016/j.apcatb.2011.05.019>
- Nicolas-Tolentino, Elaine, Tian, Zheng-Rong, Zhou, Hua, Xia, Guanguang, & Suib, Steven L. (1999). Effects of  $\text{Cu}^{2+}$  Ions on the Structure and Reactivity of Todorokite- and Cryptomelane-Type Manganese Oxide Octahedral Molecular Sieves. *Chemistry of Materials*, *11*(7), 1733-1741. doi: 10.1021/cm9811040
- Ojala, Satu, Pitkäaho, Satu, Laitinen, Tiina, Niskala Koivikko, Niina, Brahmi, Rachid, Gaálová, Jana, . . . Keiski, Riitta L. (2011). Catalysis in VOC Abatement. *Topics in Catalysis*, *54*(16), 1224. doi: 10.1007/s11244-011-9747-1
- Ordóñez, Salvador, Bello, Lisardo, Sastre, Herminio, Rosal, Roberto, & Díez, Fernando V. (2002). Kinetics of the deep oxidation of benzene, toluene, n-hexane and their binary mixtures over a platinum on  $\gamma$ -alumina catalyst. *Applied Catalysis B: Environmental*, *38*(2), 139-149. doi: [https://doi.org/10.1016/S0926-3373\(02\)00036-X](https://doi.org/10.1016/S0926-3373(02)00036-X)
- Parida, K. M., & Samal, Amarendra. (1999). Catalytic combustion of volatile organic compounds on Indian Ocean manganese nodules. *Applied Catalysis A: General*, *182*(2), 249-256. doi: [https://doi.org/10.1016/S0926-860X\(99\)00015-0](https://doi.org/10.1016/S0926-860X(99)00015-0)
- Pasero, Marco. (2005). A Short Outline of the Tunnel Oxides. *Reviews in Mineralogy and Geochemistry*, *57*(1), 291-305. doi: 10.2138/rmg.2005.57.9
- Paulis, María, Peyrard, Héléne, & Montes, Mario. (2001). Influence of Chlorine on the Activity and Stability of Pt/ $\text{Al}_2\text{O}_3$  Catalysts in the Complete Oxidation of Toluene. *Journal of Catalysis*, *199*(1), 30-40. doi: <https://doi.org/10.1006/jcat.2000.3146>
- Pawelec, B., La Parola, V., Navarro, R. M., Murcia-Mascarós, S., & Fierro, J. L. G. (2006). On the origin of the high performance of MWNT-supported PtPd catalysts for the hydrogenation of aromatics. *Carbon*, *44*(1), 84-98. doi: <https://doi.org/10.1016/j.carbon.2005.07.004>
- Peluso, Miguel A., Pronsato, Estela, Sambeth, Jorge E., Thomas, Horacio J., & Busca, Guido. (2008). Catalytic combustion of ethanol on pure and alumina supported K-Mn oxides: An IR and flow reactor study. *Applied Catalysis B: Environmental*, *78*(1), 73-79. doi: <https://doi.org/10.1016/j.apcatb.2007.09.002>
- Peña, M. A., & Fierro, J. L. G. (2001). Chemical Structures and Performance of Perovskite Oxides. *Chemical Reviews*, *101*(7), 1981-2018. doi: 10.1021/cr980129f
- Peng, Jiayi, & Wang, Shudong. (2007). Performance and characterization of supported metal catalysts for complete oxidation of formaldehyde at low temperatures. *Applied Catalysis B: Environmental*, *73*(3), 282-291. doi: <https://doi.org/10.1016/j.apcatb.2006.12.012>
- Piumetti, Marco, Fino, Debora, & Russo, Nunzio. (2015). Mesoporous manganese oxides prepared by solution combustion synthesis as catalysts for the total oxidation of VOCs. *Applied Catalysis B: Environmental*, *163*(Supplement C), 277-287. doi: <https://doi.org/10.1016/j.apcatb.2014.08.012>
- Preoana, Luminita, Malic, Barbara, Kosec, Marija, Carata, Mariana, Caldaru, Monica, & Zaharescu, Maria. (2007). Characterization of  $\text{LaCoO}_3$  powders obtained by water-based sol–gel method with citric acid. *Journal of the European Ceramic Society*, *27*(13), 4407-4411. doi: <https://doi.org/10.1016/j.jeurceramsoc.2007.02.161>
- Puértolas, Begoña, Smith, Abigail, Vázquez, Isabel, Dejoz, Ana, Moragues, Alaina, Garcia, Tomas, & Solsona, Benjamin. (2013). The different catalytic behaviour in the propane



- total oxidation of cobalt and manganese oxides prepared by a wet combustion procedure. *Chemical Engineering Journal*, 229(Supplement C), 547-558. doi: <https://doi.org/10.1016/j.cej.2013.06.041>
- Radic, Nenad, Grbic, Bosko, & Terlecki-Baricevic, Ana. (2004). Kinetics of deep oxidation of n-hexane and toluene over Pt/Al<sub>2</sub>O<sub>3</sub> catalysts: Platinum crystallite size effect. *Applied Catalysis B: Environmental*, 50(3), 153-159. doi: <https://doi.org/10.1016/j.apcatb.2004.01.011>
- Ramesh, Kanaparthi, Chen, Luwei, Chen, Fengxi, Liu, Yan, Wang, Zhan, & Han, Yi-Fan. (2008). Re-investigating the CO oxidation mechanism over unsupported MnO, Mn<sub>2</sub>O<sub>3</sub> and MnO<sub>2</sub> catalysts. *Catalysis Today*, 131(1), 477-482. doi: <https://doi.org/10.1016/j.cattod.2007.10.061>
- Rooke, Joanna C., Barakat, Tarek, Brunet, Julien, Li, Yu, Finol, Manuel Franco, Lamonier, Jean-François, . . . Su, Bao Lian. (2015). Hierarchically nanostructured porous group Vb metal oxides from alkoxide precursors and their role in the catalytic remediation of VOCs. *Applied Catalysis B: Environmental*, 162(Supplement C), 300-309. doi: <https://doi.org/10.1016/j.apcatb.2014.06.056>
- Rotter, H., Landau, M. V., Carrera, M., Goldfarb, D., & Herskowitz, M. (2004). High surface area chromia aerogel efficient catalyst and catalyst support for ethylacetate combustion. *Applied Catalysis B: Environmental*, 47(2), 111-126. doi: <https://doi.org/10.1016/j.apcatb.2003.08.006>
- Rui, Zebao, Chen, Chunyan, Lu, Yubing, & Ji, Hongbing. (2014). Anodic Alumina Supported Pt Catalyst for Total Oxidation of Trace Toluene. *Chinese Journal of Chemical Engineering*, 22(8), 882-887. doi: <https://doi.org/10.1016/j.cjche.2014.06.011>
- Saqr, Saleh M., Kondarides, Dimitris I., & Verykios, Xenophon E. (2011). Catalytic oxidation of toluene over binary mixtures of copper, manganese and cerium oxides supported on  $\gamma$ -Al<sub>2</sub>O<sub>3</sub>. *Applied Catalysis B: Environmental*, 103(3), 275-286. doi: <https://doi.org/10.1016/j.apcatb.2011.01.001>
- Satterfield, C.N. (1991). *Heterogeneous catalysis in industrial practice. 2nd edition*: New York, NY (United States); McGraw Hill Book Co.; None.
- Schurz, Fanny, Bauchert, Jörg M., Merker, Thorsten, Schleid, Thomas, Hasse, Hans, & Gläser, Roger. (2009). Octahedral molecular sieves of the type K-OMS-2 with different particle sizes and morphologies: Impact on the catalytic properties in the aerobic partial oxidation of benzyl alcohol. *Applied Catalysis A: General*, 355(1), 42-49. doi: <https://doi.org/10.1016/j.apcata.2008.11.014>
- Scirè, Salvatore, Minicò, Simona, Crisafulli, Carmelo, Satriano, Cristina, & Pistone, Alessandro. (2003). Catalytic combustion of volatile organic compounds on gold/cerium oxide catalysts. *Applied Catalysis B: Environmental*, 40(1), 43-49. doi: [https://doi.org/10.1016/S0926-3373\(02\)00127-3](https://doi.org/10.1016/S0926-3373(02)00127-3)
- Scott, D. W., Guthrie, G. B., Messerly, J. F., Todd, S. S., Berg, W. T., Hossenlopp, I. A., & McCullough, J. P. (1962). TOLUENE: THERMODYNAMIC PROPERTIES, MOLECULAR VIBRATIONS, AND INTERNAL ROTATION. *The Journal of Physical Chemistry*, 66(5), 911-914. doi: 10.1021/j100811a038
- Shah, R. K., Thonon, B., & Benforado, D. M. (2000). Opportunities for heat exchanger applications in environmental systems. *Applied Thermal Engineering*, 20(7), 631-650. doi: [https://doi.org/10.1016/S1359-4311\(99\)00045-9](https://doi.org/10.1016/S1359-4311(99)00045-9)
- Shen, Yan-Fei, Suib, Steven L., & O'Young, Chi-Lin. (1994). Effects of Inorganic Cation Templates on Octahedral Molecular Sieves of Manganese Oxide. *Journal of the American Chemical Society*, 116(24), 11020-11029. doi: 10.1021/ja00103a018
- Sihaib, Z., Puleo, F., Garcia-Vargas, J. M., Retailleau, L., Descorme, C., Liotta, L. F., . . . Giroir-Fendler, A. (2017). Manganese oxide-based catalysts for toluene oxidation. *Applied*

- Catalysis B: Environmental*, 209(Supplement C), 689-700. doi: <https://doi.org/10.1016/j.apcatb.2017.03.042>
- Solsona, Benjamín, Garcia, Tomás, Aylón, Elvira, Dejoz, Ana M., Vázquez, Isabel, Agouram, Said, . . . Taylor, Stuart H. (2011). Promoting the activity and selectivity of high surface area Ni–Ce–O mixed oxides by gold deposition for VOC catalytic combustion. *Chemical Engineering Journal*, 175(Supplement C), 271-278. doi: <https://doi.org/10.1016/j.cej.2011.09.104>
- Spinicci, R., Delmastro, A., Ronchetti, S., & Tofanari, A. (2003). Catalytic behaviour of stoichiometric and non-stoichiometric LaMnO<sub>3</sub> perovskite towards methane combustion. *Materials Chemistry and Physics*, 78(2), 393-399. doi: [https://doi.org/10.1016/S0254-0584\(02\)00218-3](https://doi.org/10.1016/S0254-0584(02)00218-3)
- Spinicci, R., Faticanti, M., Marini, P., De Rossi, S., & Porta, P. (2003). Catalytic activity of LaMnO<sub>3</sub> and LaCoO<sub>3</sub> perovskites towards VOCs combustion. *Journal of Molecular Catalysis A: Chemical*, 197(1–2), 147-155. doi: [http://dx.doi.org/10.1016/S1381-1169\(02\)00621-0](http://dx.doi.org/10.1016/S1381-1169(02)00621-0)
- Sun, Hong, Chen, Shuo, Wang, Peng, & Quan, Xie. (2011). Catalytic oxidation of toluene over manganese oxide octahedral molecular sieves (OMS-2) synthesized by different methods. *Chemical Engineering Journal*, 178(Supplement C), 191-196. doi: <https://doi.org/10.1016/j.cej.2011.10.047>
- Sun, Hong, Liu, Zhigang, Chen, Shuo, & Quan, Xie. (2015). The role of lattice oxygen on the activity and selectivity of the OMS-2 catalyst for the total oxidation of toluene. *Chemical Engineering Journal*, 270(Supplement C), 58-65. doi: <https://doi.org/10.1016/j.cej.2015.02.017>
- Taguchi, Hideki, Matsu-ura, Shin-ichiro, Nagao, Mahiko, Choso, Testuo, & Tabata, Kenji. (1997). Synthesis of LaMnO<sub>3</sub>+ $\delta$  by Firing Gels Using Citric Acid. *Journal of Solid State Chemistry*, 129(1), 60-65. doi: <https://doi.org/10.1006/jssc.1996.7229>
- Taguchi, Hideki, Sugita, Akio, Nagao, Mahiko, & Tabata, Kenji. (1995). Surface characterization of LaMnO<sub>3</sub>+ $\delta$  powder annealed in air. *Journal of Solid State Chemistry*, 119(1), 164-168. doi: [https://doi.org/10.1016/0022-4596\(95\)80025-K](https://doi.org/10.1016/0022-4596(95)80025-K)
- Tichenor, Bruce A., & Palazzolo, Michael A. (1987). Destruction of volatile organic compounds via catalytic incineration. *Environmental Progress*, 6(3), 172-176. doi: 10.1002/ep.670060328
- Tidahy, H. L., Siffert, S., Wyrwalski, F., Lamonier, J. F., & Aboukais, A. (2007). Catalytic activity of copper and palladium based catalysts for toluene total oxidation. *Catalysis Today*, 119(1), 317-320. doi: <https://doi.org/10.1016/j.cattod.2006.08.023>
- Todorova, S., Kolev, H., Holgado, J. P., Kadinov, G., Bonev, Ch, Pereñíguez, R., & Caballero, A. (2010). Complete n-hexane oxidation over supported Mn–Co catalysts. *Applied Catalysis B: Environmental*, 94(1), 46-54. doi: <https://doi.org/10.1016/j.apcatb.2009.10.019>
- Wang, Ching-Huei. (2004). Al<sub>2</sub>O<sub>3</sub>-supported transition-metal oxide catalysts for catalytic incineration of toluene. *Chemosphere*, 55(1), 11-17. doi: <https://doi.org/10.1016/j.chemosphere.2003.10.036>
- Wang, Xiangang, Cheung, C. S., Di, Yage, & Huang, Zuohua. (2012). Diesel engine gaseous and particle emissions fueled with diesel–oxygenate blends. *Fuel*, 94(0), 317-323. doi: <http://dx.doi.org/10.1016/j.fuel.2011.09.016>
- Wang, Xiaobin, Zhang, Xiongf, Wang, Yao, Liu, Haiou, Qiu, Jieshan, Wang, Jinqu, . . . Yeung, King Lun. (2011). Investigating the Role of Zeolite Nanocrystal Seeds in the Synthesis of Mesoporous Catalysts with Zeolite Wall Structure. *Chemistry of Materials*, 23(20), 4469-4479. doi: 10.1021/cm201619y

- Xia, Yunsheng, Dai, Hongxing, Jiang, Haiyan, Deng, Jiguang, He, Hong, & Au, Chak Tong. (2009). Mesoporous Chromia with Ordered Three-Dimensional Structures for the Complete Oxidation of Toluene and Ethyl Acetate. *Environmental Science & Technology*, 43(21), 8355-8360. doi: 10.1021/es901908k
- Yu, Lin, Sun, Ming, Yu, Jian, Yu, Qian, Hao, Zhifeng, & Li, Chaosheng. (2008). Synthesis and Characterization of Manganese Oxide Octahedral Molecular Sieve and Its Catalytic Performance for DME Combustion. *Chinese Journal of Catalysis*, 29(11), 1127-1132. doi: [https://doi.org/10.1016/S1872-2067\(09\)60013-9](https://doi.org/10.1016/S1872-2067(09)60013-9)
- Zhang, Chuanhui, Guo, Yanglong, Guo, Yun, Lu, Guanzhong, Boreave, Antoinette, Retailleau, Laurence, . . . Giroir-Fendler, Anne. (2014a). LaMnO<sub>3</sub> perovskite oxides prepared by different methods for catalytic oxidation of toluene. *Applied Catalysis B: Environmental*, 148(Supplement C), 490-498. doi: <https://doi.org/10.1016/j.apcatb.2013.11.030>
- Zhang, Chuanhui, Guo, Yanglong, Guo, Yun, Lu, Guanzhong, Boreave, Antoinette, Retailleau, Laurence, . . . Giroir-Fendler, Anne. (2014b). LaMnO<sub>3</sub> perovskite oxides prepared by different methods for catalytic oxidation of toluene. *Applied Catalysis B: Environmental*, 148-149, 490-498. doi: <https://doi.org/10.1016/j.apcatb.2013.11.030>
- Zimowska, M., Michalik-Zym, A., Janik, R., Machej, T., Gurgul, J., Socha, R. P., . . . Serwicka, E. M. (2007). Catalytic combustion of toluene over mixed Cu–Mn oxides. *Catalysis Today*, 119(1), 321-326. doi: <https://doi.org/10.1016/j.cattod.2006.08.022>